Ministry of Higher Education and Scientific Research
University 08 Mai 1945, Guelma
Faculty of Sciences and Engineering

THEORETICAL STUDIES OF THE STRUCTURAL, ELECTRONIC AND OPTICAL PROPERTIES OF THE COMPOUNDS BASED ON THE ELEMENTS OF II, IV AND VI GROUPS

A thesis presented to the Exact Sciences Department at the Faculty of Sciences and Engineering at the University 08 Mai 1945 in partial fulfillment of the requirements for the degree of '' Doctorat en Sciences'' in Physics.

By

Fateh KALARASSE

Examining board:

President:	Ahmed BOUFELFEL	Prof.	University of Guelma
Supervisor:	Badis BENNECER	Prof.	University of Guelma
Examiners:	Hafid AOURAG	Prof.	University of Tlemcen
	Bachir BOUHAFS	Prof.	University of SBA
	Hafid BELKHIR	Prof.	University of Annaba
	Sacia DJEROUD	MC	University of Guelma

2008

Abstract

We report on theoretical study of the structural, electronic and optical properties of semiconductors using the full–potential linearized augmented plane wave method (FP–LAPW) in the framework of density functional theory (DFT).
This study includes the rocksalt–like compounds GeTe, SnTe and PbTe, the antifluorite compounds Be_2C, Mg_2C, Mg_2Si and Mg_2Ge and the Nowotny–Juza compounds LiZnN, LiZnP, LiZnAs and LiCdP. The obtained results are in good agreement with the available experimental data.
The bandgap of the rocksalt compounds and LiZnN, show an anomalous behavior; it decreases when the atomic number decreases. The small bandgap of LiZnN compared to LiZnP can be attributed to the anion p–cation d repulsion effects.
The study of the optical properties shows that the dielectric constant decreases with increasing the cation atomic number for the rocksalt-like and antifluorite compounds and increases with increasing the anion atomic number for the other studied compounds.
The elastic properties and the valence charge density distribution show that the filled tetrahedral compounds LiZnP, LiZnAs and LiCdP have a covalent bond (e.g., Zn–As) and ionic one (e.g., Li–As) so that they can be characterized as half–ionic and half–covalent semiconductors.
Finally, the study of the effect of hydrostatic pressure on the electronic and optical properties shows that the antifluorite compounds follow the same behaviour as the elemental diamond–like semiconductors, silicon and diamond. However, the small values of Be_2C pressure coefficients compared to those of diamond are attributed to the ionic nature of the Be–C bond in Be_2C.

ملخص

في هذه الرسالة قمنا بدراسة نظرية للخواص الالكترونية و الضوئية بالإضافة إلى الخواص البنيوية لأنصاف النواقل. هذه الدراسة تمت في إطار نظرية دالة الكثافة، حيث تم حل معادلة شرودنغر بطريقة التناسق الذاتي.

هذه الدراسة تشمل المركبات GeTe ، SnTe ، PbTe التي تتبلور على شكل كلوريد الصوديوم (NaCl) و المركبات Be2C، Mg2C، Mg2Si، Mg2Ge والتي تتبلور على شكل مضاد الفليوريد و المركبات المعروفة باسم نووتني جوزا LiZnN، LiZnP، LiZnAs، LiCdP ، حيث حصلنا على نتائج متوافقة إلى حد كبير مع النتائج التجريبية.

الفاصل الطاقي بين عصابات التكافؤ و عصابات النقل يتبع سلوك غير مألوف بالنسبة للمركبات GeTe ، PbTe،SnTe و كذلك بالنسبة للمركب LiZnN. حيث انه يتناقص مع تناقص العدد الذري.

حيث تم تفسير صغر قيمة الفاصل الطاقي لـ LiZnN مقارنة مع المركب LiZnP بتنافر مدارات d للذرة Zn مع مدارات p للذرة N.

دراسة الخواص الضوئية بينت أن الثابت الكهربائي للعوازل يتزايد مع تناقص العدد الذري في المركبات GeTe، SnTe، PbTe وهذا أيضا سلوك غير مألوف. أما بالنسبة للمركبات الأخرى هذا الثابت يتبع سلوك عادي حيث يتناقص مع تناقص العدد الذري.

دراسة خواص المرونة و توزيع الشحنات في المركبات LiZnN، LiZnP، LiZnAs، LiCdP تبين أن هذه المركبات ذات رابطة تكافئية، Zn-As مثلا، و رابطة أيونية، Li- As على سبيل المثال، و بالتالي يمكن اعتبارها كمركبات تكافئية و أيونية في نفس الوقت.

أخيرا دراسة تأثير الضغط الهيدروستاتيكي على الخواص الالكترونية و الضوئية للمركبات Be_2C، Mg_2C، Mg_2Si، Mg_2Ge تبين أن هذه المركبات تتبع سلوك مماثل لسلوك أنصاف النواقل الأولية مع تناقص ملحوظ لمعاملات الضغط لـ Be_2C مقارنة مع معاملات الماس حيث تم تفسيرها بطبيعة الرابطة الأيونية Be-C في المركب Be_2C مقارنة مع الرابطة التكافئية للماس.

Résumé

Dans cette thèse nous avons effectué une étude théorique des propriétés structurales, électroniques et optiques des semi-conducteurs, en utilisant la méthode linéaire des ondes planes augmentées (FP-LAPW), dans le cadre de la théorie de la fonctionnelle de la densité (DFT). Cette étude porte sur les semi-conducteurs GeTe, SnTe et PbTe qui se cristallisent dans une structure de chlorure de sodium, les composés Be2C, Mg2C, Mg2Si et Mg2Ge cristallisant dans la structure anti-fluorite et les composés de Nowotny et Juza LiZnN, LiZnP, LiZnAs et LiCdP. Les résultats obtenus sont en bon accord avec les données expérimentales disponibles.

Le gap d'énergie des composés GeTe, SnTe, PbTe et LiZnN présente une anomalie; il diminue avec la diminution du nombre atomique. En particulier, la petite valeur du gap de LiZnN par rapport à celui de LiZnP est due à la répulsion entre l'orbital d de l'atome du zinc et l'orbital p de l'atome d'azote.

L'étude des propriétés optiques montre que la constante diélectrique statique augmente quand le nombre atomique diminue pour les composés GeTe, SnTe et PbTe, par contre elle diminue pour les autres composés étudiés.

Les propriétés élastiques et la distribution des charges de valence, montrent l'existence des deux caractères ionique et covalent des liaisons dans les composés à liaisons tétraédriques remplies.

L'étude de l'effet de pression hydrostatique sur les propriétés électroniques et optiques des composés Be_2C, Mg_2C, Mg_2Si et Mg_2Ge montre que ces composés se comportent comme les semi-conducteurs élémentaires ; le silicium et le diamant. Les petites valeurs des coefficients de pression de Be_2C par rapport à celles du diamant ont été attribuées au caractère ionique de la liaison Be-C.

Acknowledgements

During my scientific career many people contributed to my education, so that it is impossible to give an explicit acknowledgement to all of them here. Thus I will just mention those directly involved in this work.

First of all I would like to express my sincere appreciation and thanks to my supervisor Prof. Badis Bennecer at the Exact Sciences Department, Guelma University, for his scientific guidance, support and encouragement throughout this research work. I have also appreciated the discussions about research ethics. But, most of all, I am grateful to him for providing me the freedom to pursue my own ideas with unconditional support.

I thank the members of examining board, Prof. Ahmed Boufelfel (Guelma University), Prof. Hafid Aourag (Tlemcen University), Prof. Bachir Bouhafs (Sidi Bel Abbes University), Prof. Hafid Belkhir (Annaba University) and Dr. S. Djeroud (Guelma University), for accepting to evaluate my work.

I would like to express my deepest gratitude to Prof. A. Boufelfel (head of the Guelma Physics Laboratory) and Prof. Bennecer who gave me the opportunities to enjoy the Guelma Physics Laboratory GPL, I am very fortunate to be a part of a highly motivated research group. The numerous conversations with Makhlouf Kharoubi, Mostafa Ben Yakhlef, Kamel Zanat and Abdallah Mellouki had a great impact on my work.

I thank my colleagues at the Exact Sciences Department, Guelma University.

The Computational Quantum Theory Group, Technical University, Vienna is acknowledged for providing us the software code WIEN2K used in the calculations and Dr. Sangeeta Sharma is thanked for providing me the linear and nonlinear optic package. Also the EXCITING code developer team (Institut

für Physik, Karl–Franzens–Universität,A–8010 Graz, Austria) is thanked for making this promising code freely available. Especially, the contacts with S. Sharma and Kay Dewhurst had encouraged and helped me a lot during some dark period. This work is also supported by the Algerian Ministry of High Education and Scientific Search.

Many other people contributed to this work. I thank Dr. Abderazak Bezazi, D. Hiceri and Ali Hamidani for their help in getting the documentation used in this work. Prof. Bachir Bouhafs is acknowledged for his help, advice and suggestions. Prof. K. Kuriyama (from Hosei University, Japan) merits his place in these acknowledgements for providing us with some unpublished data, so I thank him again for his confidence.

But if there are other persons who I have to thank the most, they are my parents. Without their help and support, I could never finish this work. They gave me the strength to face difficult times. They taught me the meaning of life. They always give and never ask. Really, I do not have words to thank them. I will be always indebted to them.

Finally, I would like to thank all my friends, especially, Belgassem, Abderazak, Akrem, Abdessalem, Mounir, Ryad, Said and Ahmed, for their help, support and encouragements during the realization of this work.

CONTENTS

LIST OF TABLES

LIST OF FIGURES

CHAPTER 1

Introduction

The use and understanding of materials have gone hand in hand with the advances of civilization and technology since the first use of primitive tools. Historian uses the dominant materials of an ancient era to classify it. Historical ages - the Stone Age, the Bronze Age, the Iron Age - have often been named according to the material dominating the technology of that time [1,2].

The properties of a given material depend on the chemical nature of its constituent atoms, and their arrangement and distribution in its microstructure. Thus, the objective of modern materials science is to tailor a material in order to obtain a desired set of properties suitable for a given application [1].

Since the discovery of the bipolar junction transistor by Shockly, Bardeen and Brattain in 1948, semiconductors have been and still are the basic materials for the technological revolutions of electronics [3]. Silicon is the most used and developed semiconductors up to now, however, owing to its indirect bandgap it is not suitable optical source which requires direct gap to achieve a high probability of transitions which ensure a high efficiency [4]. Therefore, other compounds, such as II–VI and III–V zinc–blend–like semiconductors, have been used [5].

IV–VI and II–IV semiconductors, which crystallize in the rock salt and anti-fluorite structures, respectively, are compounds usually used in light emitters and detectors operating in the Infrared region of the light spectrum. The first infrared detectors was based on lead sulfide (PbS), however the need of detector operating in specific wavelength leads to the use of other materials, such as lead salts alloys and super lattices [6, 7].

However, following Rompa et al. [8] the insertion of closed shell atom or ion in one of the empty interstitial sites of zinc–blende semiconductor can change the nature of the bandgap (from indirect to direct). On the other hand Zunger and his collaborators [9–11] aimed at the Nowotny–Juza filled tetrahedral compounds (FTC) such as LiZnP and LiZnN [12, 13]. Their works show that the Nowotny–Juza compounds $A^{I}B^{II}C^{V}$ can be viewed as zinc–blend $(B^{II}C^{V})^{-}$ filled by A^{I+} ions (e.g., LiZnP). Furthermore, they showed that $A^{I}B^{II}C^{V}$ can be obtained from the III–V zinc–blend compounds by transmuting the III atom to its isovalent pair I+II (e.g., Ga to Li+Zn), in this context the ternary FTC are analogous to the binary zinc–blend III-V compounds. Moreover the interstitial insertion rule have been proposed to describe the induced change in band structure of FTC compared to their binary analogous.

Computer modelling in the framework of quantum mechanical description of the interactions between electrons and atomic nuclei has an important impact on materials science both in fundamental understanding and design of new materials for future applications, and in many cases, it is possible to predict material properties before it has even been manufactured which greatly reduces time and cost required for this process [14].

First principles methods, which require only the atomic number and the crystal structure as input, provide a powerful tools in this field. In particular the density functional theory (DFT) is the widely accepted theory by both physicists and chemists [15, 16]. Its impact on modern physics, chemistry, and

material sciences has been deemed so important that Walter Kohn shared the Noble prize in chemistry with John Pople in 1998 [17].

In this thesis we report on first principles studies of the structural, electronic and optical properties of a series of semiconductors, including the rocksalt–like GeTe, SnTe and PbTe, and the antifluorite Mg_2–Y (Y=C, Si, Ge) and the filled tetrahedral compounds LiZnN, LiZnP, LiZnAs and LiCdP. This choice of materials enables us to study the evolution of the electronic structure of rock-salt, antifluorite and Nowotny–Juza FTC semiconductors, when the Z atomic number changes (i.e., Ge–Sn–Pb in IV–VI or Y=C, Si, Ge, Sn in antifluorite compounds) on one hand. On the other one, it enables us to view the induced behavior changes, when the crystal structure changes (space group, the change of coordination, valence electron number).

This thesis is organized as follows: in the two following chapters the theoretical background and the calculation method are briefly described. In the next five chapters we give the obtained results and discuss them. Finally a summary and concluding remarks are given.

BIBLIOGRAPHY

[1] *Europian white book on fundamental research in materials science*, Max–Planck–Institute Für Metallforschung, Stutgart (2000).

[2] P.M. Chaikin, T.C. Lubensky, *Principles of condensed matter physics*, Cambridge University Press (1995).

[3] Hartmut Haug and Stephan W. Koch, *Quntum theory of the optical and electronic properties of semiconductors*, World Scientific Publishing Co. Pte. Ltd. (2004).

[4] B. Bouhafs, F. Benkabou, M. Ferhat, B. Khelifa, J.P. Dufour and H. Aourag, Infrared Physics and Technology **36** (1995) 967.

[5] O. Maksimov, Rev. Adv. Mater. Sci. **9** (2005) 178.

[6] R. Dornhaus, G. Nimtz and B. Schlicht, *Narrow–Gap Semiconductors*, Springer–Verlag (1983).

[7] A. Rogalski, K. Adamiec and J. Rutkowski, *Narrow-Gap Semiconductor Photodiodes*, SPIE Press (2000).

[8] H.W.M. Rompa, M.F.H. Schuurmans, and F. Williams, Phys. Rev. Lett. **52** (1984) 675.

[9] D.M. Wood, A. Zunger, and R. de Groot, Phys. Rev. B **31** (1985) 2570.

[10] A.E. Carlsson, A. Zunger, and D.M. Wood, Phys. Rev. B **32** (1985) 1386.

[11] S.–H. Wei and A. Zunger, Phys. Rev. Lett. **56** (1986) 528.

[12] H. Nowotny, K. Bachmayer, Mh. Chem. **80** (1949) 734.

[13] R. Juza, F. Hund, Z. Anorg. Chem. **257** (1948) 1.

[14] J. Hafner, C. Wolverton and G. Ceder, MRS Bulletin **31** (2006) 659.

[15] P. Hohenberg and W. Kohn, Phys. Rev. B **136** (1964) 864.

[16] W. Kohn and L. J. Sham, Phys. Rev. A **140** (1965) 1113.

[17] W. Kohn, *Nobel lecture*, Rev. Mod. Phys. **71** (1999) 1253.

CHAPTER 2

The many body problem

2.1 Introduction

Matter is formed by atoms held together by chemical bonds [1–3]. Atoms are composed of a heavy positif charged nucleus and a nearly massless electrons. Thus condensed matter physics is concerned with understanding and exploiting the properties of systems of interacting electrons and atomic nuclei. In quantum mechanics the properties of such systems can be, in principle, obtained by solving the Schrödinger equation. Unfortunately, the strongly interacting many–body system, formed by electrons and nuclei, makes the solution of this equation impossible and many approaches have been proposed to solve this problem. The major and most popular ones are the Hartree–Fock approximation (HF) [4], which is usually used in quantum chemistry, and the density functional theory (DFT) used in the calculations of solids [5–7]. In this chapter, we briefly discuss the fundamental concepts of the DFT.

2.2 The electronic Schrödinger equation

The starting point for calculations of solid properties is the Schrödinger equation

$$H\psi = E\psi, \tag{2.1}$$

where H and ψ are the Hamiltonian and wavefunction of all the electrons and nuclei. ψ is a function of all electron and nuclear coordinates.
If we neglect the relativistic effects, H can be written

$$H = \sum_i \frac{\mathbf{p}_i^2}{2m_e} + \sum_\alpha \frac{\mathbf{P}_\alpha^2}{2M_\alpha} + \frac{1}{2}\sum_{i,j}{}' \frac{e^2}{|\mathbf{r}_i - \mathbf{r}_j|} + \frac{1}{2}\sum_{\alpha,\beta}{}' \frac{Z_\alpha Z_\beta e^2}{\mathbf{R}_\alpha - \mathbf{R}_\beta} - \sum_{i,\alpha} \frac{Z_\alpha e^2}{\mathbf{r}_i - \mathbf{R}_\alpha}, \tag{2.2}$$

where :

$\mathbf{P}_\alpha$ and $\mathbf{p}_i$ are the momenta of nuclei and electrons, respectively, m_e is the electron mass, M_α is the mass of the nucleus α, $\mathbf{r}_i$ and $\mathbf{R}_\alpha$ are the electronic and nuclear coordinates, respectively, and Z_α is the charge of that nucleus. The sums over i and j run over all electrons and the sums over α and β run over all the nuclei. The primes on the summations exclude $i = j$ and $\alpha = \beta$.

In the right hand side of this equation, the two first terms are the kinetic energies of the electrons and nuclei, respectively, the following two terms are the Coulomb (repulsive) potential energy between the electrons and the corresponding one for the nuclei, the last term is the Coulomb (attractive) energy between the electrons and nuclei.
Because of the presence of the last term, this Hamiltonian is not separable into the sum of a purely nuclear Hamiltonian and a purely electronic one. However, the great difference between the electron and nuclei masses makes the motion of electron faster than the one of nuclei leading to the Born–Oppenheimer approximation, within the nuclei are considered point charges at fixed positions, which enables the separation of variables [4]. This can be done by taking the wavefunction as a product of the electronic wavefunction φ and the nuclear one ϕ (i.e., $\psi = \varphi \times \phi$). Substituting this expression in (2.1) and (2.2) yields Schrödinger equations for φ and ϕ. The equation for φ is

$$\left\{ \sum_i \frac{\mathbf{p}_i^2}{2m_e} + \frac{1}{2}\sum_{i,j}{}' \frac{e^2}{|\mathbf{r}_i - \mathbf{r}_j|} - \sum_{i,\alpha} \frac{Z_\alpha e^2}{\mathbf{r}_i - \mathbf{R}_\alpha} \right\} \varphi = E\varphi, \tag{2.3}$$

this is the so called electronic Schrödinger equation.

The eigenvalue problem of equation (2.3) is a problem of a large number of variables and is very difficult to solve. Therefore, further approximations have to be made in practical calculations for realistic materials.

2.3 Hartree and Hartree–Fock approximations

In the Hartree approximation the electronic wavefunction φ of the system of n electrons is taken as the product of the single particle wavefunctions χ (one for each electron)

$$\varphi = \chi_1(\mathbf{r}_1)\chi_2(\mathbf{r}_2)\cdots\chi_n(\mathbf{r}_n), \tag{2.4}$$

substituting (2.4) into (2.3) and minimizing the energy with respect to the variations in χ_i yields a Schrödinger equation for each of the χ_i, and we write

$$\left[-\frac{\hbar^2}{2m_e}\nabla_i^2 + e^2\sum_{j\neq i}\int\frac{|\chi_j(\mathbf{r})|^2}{|\mathbf{r}_i-\mathbf{r}|}d\mathbf{r} - e^2\sum_\alpha\frac{Z_\alpha}{\mathbf{r}_i-\mathbf{R}_\alpha}\right]\chi_i(\mathbf{r}_i) = \varepsilon\chi_i(\mathbf{r}_i). \tag{2.5}$$

In this approximation, the wavefunction (2.4) does not respect the antisymmetric statistics of electrons, and the tendency for cohesion is underestimated. To overcome this problem, in the Hartree–Fock approximation the wavefunction is given in the form of a Slater determinant

$$\varphi = \frac{1}{\sqrt{n!}}\begin{vmatrix}\chi_1(\mathbf{r}_1) & \chi_1(\mathbf{r}_2) & \cdots & \chi_1(\mathbf{r}_n)\\ \chi_2(\mathbf{r}_1) & \chi_2(\mathbf{r}_2) & \cdots & \vdots\\ \vdots & \vdots & \ddots & \vdots\\ \chi_n(\mathbf{r}_1) & \cdots & \cdots & \chi_n(\mathbf{r}_n)\end{vmatrix}. \tag{2.6}$$

This wavefunction is antisymmetric. Following the same procedure as in Hartree approximation, leads to a different single particle equations

$$\left[-\frac{\hbar^2}{2m_e}\nabla_i^2 + e^2\sum_{j\neq i}\int\frac{|\chi_j(\mathbf{r})|^2}{|\mathbf{r}_i-\mathbf{r}|}d\mathbf{r} - e^2\sum_\alpha\frac{Z_\alpha}{\mathbf{r}_i-\mathbf{R}_\alpha}\right]\chi_i(\mathbf{r}_i) - e^2\sum_j\int\frac{\chi_j^*(\mathbf{r})\chi_j(\mathbf{r_i})\chi_i(\mathbf{r})}{|\mathbf{r}_i-\mathbf{r}_j|} = \varepsilon\chi_i(\mathbf{r}_i). \tag{2.7}$$

The last term in this equation is called the exchange term which arises from the antisymmetrized function (2.6).

The Hartree–Fock approximation is a wave–function–based method. In fact, when high accuracy is required many Slater determinants are used, so that comprehension becomes difficult. It is worth adding that the cohesive energy of solids, even improved, is still underestimated in this approximation.

2.4 Density functional theory

Density functional theory is now the most popular approach for calculating the electronic properties of materials. It is a theory of electronic structure formulated in terms of the electron density as the basic unknown function instead of the electron wave function in the Hartree and Hartree–Fock approximations. Although the electronic density has been introduced early in the works of Fermi [8] and Gaspar [9]. However, the DFT has been given a firm foundation by Hohenberg and Kohn [5], and Kohn and Sham [6]. Since then an enormous amount of work has been done in this field and several monographs, textbooks, reviews have been devoted to this novel approach. Here we just point out the fundamental concepts of the theory. Namely, the Hohenberg–Kohn theorem, the Kohn–Sham equations and the exchange and correlation potential.

2.4.1 Hohenberg–Kohn theorem

For a system of N electrons moving under the influence of some local external potential $v(\mathbf{r})$. The first Hohenberg–Kohn theorem states that $v(\mathbf{r})$ is determined within an arbitrary additive constant by the knowledge of the electron density $n(\mathbf{r})$. The proof proceeds by reductio ad absurdum. That is to say that the total energy of the system is given exactly as a functional of the ground state density

$$E = E[n(\mathbf{r})]. \tag{2.8}$$

The second theorem states that for a given external potential $v(\mathbf{r})$, the correct charge density $n(\mathbf{r})$ minimizes the ground state energy $E[n(\mathbf{r})]$.

The Hohenberg–Kohn theorem does not provide any idea about the form of the functional $E[n(\mathbf{r})]$ and therefore the utility of the DFT depends on the discovery of sufficiently accurate approximations. The best scheme for the implementation of the DFT is the Kohn–Sham one.

2.4.2 The single particle Kohn–Sham equations

Kohn and Sham introduced the idea of an auxiliary non–interacting system, in which the electrons move independently in a common effective local potential, with the same electron density as the real system [6]. Therefore, the density can be taken as the sum of single particle densities

$$n(\mathbf{r}) = \sum_{i=1}^{N} |\psi(\mathbf{r})|^2, \tag{2.9}$$

and the Hohenberg–Kohn functional takes the form

$$\begin{aligned} E[n(\mathbf{r})] = &- \frac{\hbar^2}{2m} \sum_{i=1}^{N} \int \psi_i^*(\mathbf{r}) \nabla^2 \psi_i(\mathbf{r}) d\mathbf{r} + \int n(\mathbf{r}) V_{ion}(\mathbf{r}) d\mathbf{r} \\ &+ \frac{e^2}{8\pi\varepsilon_0} \int \int \frac{n(\mathbf{r}) n(\mathbf{r}')}{|\mathbf{r} - \mathbf{r}'|} d\mathbf{r} d\mathbf{r}' + E_{xc}[n(\mathbf{r})], \end{aligned} \tag{2.10}$$

where the right hand side terms are the kinetic energy of the non–interacting electrons, the energy of interaction with the ionic potential, the Hartree energy, and the exchange and correlation interaction energy. The last term is still unknown and has to be approximated, one of the most used approach, the local density approximation, is discussed in the next subsection.

The minimization of the total energy functional of equation (2.10) by using the method of Lagrange multiplies lead to the single particle Kohn–Sham equations

$$\left[-\frac{\hbar^2}{2m} \nabla^2 + V_{eff} \right] \psi_i(\mathbf{r}) = \varepsilon_i \psi_i(\mathbf{r}), \tag{2.11}$$

where the effective potential is the sum of Coulomb (V_C) and exchange correlation (V_{xc}) potentials

$$V_{eff}(\mathbf{r}) = V_C(\mathbf{r}) + V_{xc}[n(\mathbf{r})], \tag{2.12}$$

The equation (2.11) is probably the most important equation of the density functional theory. It tells us that the motion of the interacting electrons can be treated exactly as a system of independent particles.

2.4.3 Local density approximation

In order to use the Kohn–Sham formulation for the DFT, an approximate form for the exchange and correlation energy is required. The local density approximation (LDA) is the simplest and the widely used approximation in which the exchange and correlation energy is taken to be the same as in a uniform electron gas of the same density

$$E_{xc}^{LDA} = \int e_{xc}[n(\mathbf{r})]n(\mathbf{r})d\mathbf{r}. \tag{2.13}$$

Modern forms of the local density approximation are based on the total energy of the homogeneous electron gas derived from quantum Monte Carlo simulations [10].

2.4.4 Solving the single particle equations

Finding the solution of the Kohn–Sham equation is the major computational problem in determining the ground state charge density and hence the other properties. To do this, the Kohn–Sham orbital ψ_i is expanded in term of the basis functions ϕ_j

$$\psi_i(\mathbf{r}) = \sum_j a_{ij}\phi_j(\mathbf{r}), \tag{2.14}$$

where a_{ij} are the expansion coefficients.

By substituting equation (2.14) in (2.11), multiplying both sides by $\phi_j^*(\mathbf{r})$, and

integrating over all space, the a_{ij} and ε_i form the eigenvalue problem

$$\sum_j (H_{kj} - \varepsilon_i S_{kj}) a_{ij} = 0, \tag{2.15}$$

where

$$H_{kj} = \int \phi_k^*(\mathbf{r}) \left[-\frac{\hbar^2}{2m} \nabla^2 + V_{eff}(\mathbf{r}) \right] \phi_j(\mathbf{r}) d^3\mathbf{r}, \tag{2.16}$$

is the Hamiltonian matrix and

$$S_{kj} = \int \phi_k^*(\mathbf{r}) \phi_j(\mathbf{r}) d^3\mathbf{r}, \tag{2.17}$$

is the overlap matrix.

BIBLIOGRAPHY

[1] O. Madelung, *Introduction to solid state theory*, Springer–Verlag 1978.

[2] N.W. Ashcroft. N.D. Mermin. *Solid State Physics*, Hault-Saunders Internationnal Editions 1981.

[3] I.M. Tsidilskovski, *Banb structure of semiconductors*, translated from Russian by R.S. Wadhwa, Pergamon Press 1982.

[4] G.C. Fletcher, *The Electron Band Theory of Solids*. NORTH-HOLAND PUBLISHING COMPANY, AMSTERDAM. LONDON 1971.

[5] P. Hohenberg and W. Kohn, Phys. Rev. B **136** (1964) 864.

[6] W. Kohn and L. J. Sham, Phys. Rev. A **140** (1965) 1113.

[7] W. Kohn, *Nobel lecture*, Rev. Mod. Phys. **71** (1999) 1253.

[8] L.H. Thomas, *The calculation of atomic fields*, Proc. Cambridge Phil. Soc. 23, 542 (1927).

[9] Á. Nagy, *Density functional theory and application to atoms and molecules*. PHYSICS REPORTS, ELSEVIER 1998.

[10] J. Hafner, C. Wolverton and G. Ceder, MRS Bulletin **31** (2006) 659.

CHAPTER 3

Method of calculation

3.1 Introduction

In the previous chapter, it has been shown that the many electrons Schrödinger equation can be mapped to a system of single particle equations called the Kohn–Sham equations. In solving these equations a basis set and a form to describe the crystal potential are required. The computational methods are usually distinguished by these choices. Pseudo–potential and plane waves (PW–PP), full-potential linear muffin-tin orbital (FP–LMTO) or full–potential linearized augmented plane wave (FP–LAPW), are examples of such methods [1, 2]. In our calculations we have used the state of the art FP–LAPW method, which is among the most accurate known method. In this chapter we briefly discuss the main concepts of this method and its applications in the physical properties computation [1, 5].

3.2 APW method

The FP–LAPW method is a modification of the augmented plane wave method (APW) developed by Slater in 1937 [1]. The basic idea of the later method is that: (i) Near an atomic nucleus the potential and wave function are atomic–like; that is to say that they are strongly varying but have nearly spherical

symmetry. (ii) Between the atoms the potential and wave function are smooth. So that space can be divided into spherical regions centered at atomic nucleus sites, the so called muffin-tin spheres, and the remaining unit cell volume constitutes the interstitial region. In the spherical region the potential is assumed to be spherically symmetric, whereas, in the interstitial region is constant which can be taken as zero

$$V(\mathbf{r}) = \begin{cases} V(r) & \text{for } r < r_s, \\ 0 & \text{for } r > r_s. \end{cases} \tag{3.1}$$

The basis functions are combinations of spherical harmonics times a radial function inside the spheres and plane waves in the interstitial region

$$\varphi(\mathbf{r}) = \begin{cases} \sum_{\ell m} A_{\ell m} U_\ell(r) Y_{\ell m}(r) & \text{for } r < r_s, \\ \\ \frac{1}{\sqrt{\Omega}} \sum_G C_G \exp\left[i(\mathbf{G}+\mathbf{K})\cdot\mathbf{r}\right] & \text{for } r > r_s, \end{cases} \tag{3.2}$$

where φ is a wave function, Ω is the unit cell volume, U_l is the regular solution of

$$\left\{ -\frac{d^2}{dr^2} + \frac{\ell(\ell+1)}{r^2} + V(r) - E_\ell \right\} r U_\ell(r) = 0. \tag{3.3}$$

The true (real) wavefunction is continuous, so that the APW basis functions must also be continuous at the sphere surface (i.e., for $r = r_s$). Therefore, the coefficients A_{lm} are chosen so that the basis functions inside the sphere matches to plane wave (interstitial region) for $r = r_s$. This can be done by expanding the plane wave in spherical harmonics, and we obtain

$$A_{\ell m} = \frac{4\pi i^\ell}{\sqrt{\Omega} U_\ell(r)} \sum_G C_G J_\ell\left(|\mathbf{K}+\mathbf{G}|\,\mathbf{R}\right) Y^*_{\ell m}(\mathbf{K}+\mathbf{G}), \tag{3.4}$$

where J_ℓ is a spherical Bessel function.

The APW method gives good results for close packed *fcc* and ideal c/a *hcp* materials. However, it is less accurate for *bcc* and related materials and becomes less reliable as the site symmetry and coordination decrease. This method

suffers from many problems, in particular, the matching condition which leads to the so called asymptote problem, and the lack of variational freedom make it computationally demanding.

3.3 FP–LAPW method

In order to solve the problems encountered in the APW method Anderson proposed the linear methods LMTO and LAPW in 1975 [1, 2].

3.3.1 The basis functions

In the LAPW method the wave functions are expanded in a linear combination of spherical harmonics and radial functions and their energy derivatives inside the muffin–tin spheres, and plane waves in the interstitial region

$$\varphi(\mathbf{r}) = \begin{cases} \frac{1}{\sqrt{\Omega}} \sum_{G} C_G \exp\left[i\left(\mathbf{K}+\mathbf{G}\right)\cdot\mathbf{r}\right] & \text{for } r > r_s, \\ \sum_{\ell m} [A_{\ell m} U_\ell(r) + B_{\ell m} \dot{U}_\ell(r)] Y_{\ell m}(r) & \text{for } r < r_s, \end{cases} \tag{3.5}$$

the radial functions satisfy the following equation

$$\frac{1}{r^2}\frac{d}{dr}\left[r^2 \frac{dU_\ell}{dr}\right] + \left[\varepsilon - \frac{\ell(\ell+1)}{r^2} - V(r)\right] U_\ell(\varepsilon, r) = 0, \tag{3.6}$$

whereas their derivatives satisfy the equation

$$\left\{\frac{1}{r^2}\frac{d}{dr} + \frac{\ell(\ell+1)}{r^2} + V(r) - E_\ell\right\} r\dot{U}_\ell(r) = rU_\ell(r), \tag{3.7}$$

the coefficients $B_{\ell m}$ are determined in the same way as the $A_{\ell m}$ ones in the APW method.

If E_ℓ differs from the band energy, the best way to describe the radial function is by using the linear combination

$$U(r) = U_l(\varepsilon_l, r) + (\varepsilon - E_l) r\dot{U}_l(r) + O\left((\varepsilon - E_l)^2\right). \tag{3.8}$$

3.3.2 The full potential

In the full–potential version of the LAPW method (FP–LAPW), no shape approximations are made for the potential and charge densities. The potential takes the following form

$$V(\mathbf{r}) = \begin{cases} \sum_{\mathbf{G}} V_{\mathbf{G}} e^{i\mathbf{G}\cdot\mathbf{r}} & \text{for } r > r_s, \\ \sum_{lm} V_{lm}(r) Y_{lm}(\mathbf{r}) & \text{for } r < r_s. \end{cases} \tag{3.9}$$

3.4 Calculation of properties

3.4.1 Total energy

Using the equation 2.11, the total energy is given by

$$E = \sum_{\alpha c} \epsilon_{\alpha C} + \sum_{occ} W(k,j)\epsilon_{k,j} - \frac{1}{2}\sum_{\alpha} Z_\alpha R(\alpha) - \int \rho(\mathbf{r})[V_{xc}(\mathbf{r}) - \epsilon_{xc} + \frac{1}{2}V_c(\mathbf{r})]d^3\mathbf{r}, \tag{3.10}$$

where the integral is over the unit cell, the sum over c is over the core states, the $W(k,j)$ are the weights associated with the valence eigenvalues, ρ is the total charge density (valence and core), ϵ_{xc} is the exchange and correlation energy density per atom, Z_α is the nuclear charge on atom α, and $R(\alpha)$ is the Coulomb potential at the nucleus minus the $Z_\alpha/\mathbf{r}$ self contribution.

3.4.2 Lattice parameter and bulk modulus

The knowledge of the total energy of crystal allows the study of its structural properties. The equilibrium lattice parameter (a), bulk modulus (B) and its pressure derivative (B') are determined by fitting the total energy as a function of volume to the Murnaghan's equation of state (eos) [3]

$$E(V) = \frac{BV}{B'}\left[\frac{(V_0/V)^{B'}}{B'-1} - 1\right] + cst., \tag{3.11}$$

with

$$B = V\frac{\partial^2 E}{\partial V^2}, \tag{3.12}$$

and

$$V = V_0 \left(1 + \frac{B'P}{B_0}\right)^{-1/B'}, \tag{3.13}$$

where B is the bulk modulus, B' is the bulk modulus pressure derivative, $E(V)$ is the total energy at volume V and V_0 is the equilibrium volume (ground state).

3.4.3 Elastic constants

Consider a crystal defined by the lattice vectors $\mathbf{a}_1$, $\mathbf{a}_2$ and $\mathbf{a}_3$. To calculate the elastic constants, the unit cell is deformed using an appropriate strain tensor to yield an energy–strain relation. The coefficients obtained from a polynomial fit to this data then yield the specific elastic constants, depending on the symmetry of the strain tensor used.

The strained lattice is defined by the distorted primitive vectors

$$\begin{pmatrix} \mathbf{a}_1' \\ \mathbf{a}_2' \\ \mathbf{a}_3' \end{pmatrix} = \begin{pmatrix} \mathbf{a}_1 \\ \mathbf{a}_2 \\ \mathbf{a}_3 \end{pmatrix} \cdot (\overleftrightarrow{I} + \overleftrightarrow{\varepsilon}), \tag{3.14}$$

where $\overleftrightarrow{I}$ is the 3×3 identity matrix and $\overleftrightarrow{\varepsilon}$ is the strain tensor given by

$$\overleftrightarrow{\varepsilon} = \begin{pmatrix} e_1 & e_6/2 & e_5/2 \\ e_6/2 & e_2 & e_4/2 \\ e_5/2 & e_4/2 & e_3 \end{pmatrix}. \tag{3.15}$$

The total energy changes by an amount

$$E(e_i) = E_0 + P(V)\Delta V + V \sum_{i=1}^{6} \sum_{j=1}^{6} C_{ij} e_i e_j / 2 + O[e_i^3]. \tag{3.16}$$

For the particular case of crystals with cubic symmetry there are only three distinct non vanishing elastic constants namely c_{11}, c_{12}, and c_{44}. To calculate their values the appropriate strain tensors and the corresponding energy strain relations are described in Refs. [5, 6].

The shear modulus G, Young modulus E and Poison's ratio ν of polycrystalline aggregate of single phase monocrystals having random orientations, can be calculated from the c_{ij}. For cubic lattices the bulk modulus is given by $B = (c_{11}+2c_{12})/3$ and the shear modulus is bounded by the Reuss and Voigt moduli, G_R and G_V, which represents its lower and upper limits, respectively [4]

$$G_R = 5(c_{11} - c_{12})c_{44}/[4c_{44} + 3(c_{11} - c_{12})], \tag{3.17}$$

$$G_V = (c_{11} - c_{12} + 3c_{44})/5, \tag{3.18}$$

and according to Hill the arithmetic mean value is taken as an estimate for G

$$G = \frac{1}{2}(G_R + G_V). \tag{3.19}$$

The bulk and shear moduli are used to calculate the Young modulus E and the Poisson's ratio ν

$$E = \frac{9BG}{3B + G}, \tag{3.20}$$

$$\nu = \frac{3B - E}{6B}. \tag{3.21}$$

3.4.4 Band characters and density of states

The density of states is a fundamental quantity in band theory. It is defined as the number of electron states in an interval of energy. If the number of states between E and $E + dE$ is $D(E)$, then the number of electrons will be $\int_0^{E_F} D(E)dE$. The density of states can be calculated from the band character (or orbital population) $Q_l^{(\alpha)}(\epsilon, \mathbf{k})$ which is the lth angular momentum component of the charge due to the wavefunction $\psi(\epsilon, \mathbf{k})$ enclosed in the sphere Ω_{MT} of radius $R_{MT}^{(\alpha)}$ about the atom α [7]

$$Q_l^{(\alpha)}(\epsilon, \mathbf{k}) = \int_{\Omega_{MT}} |\hat{P}\psi(\epsilon, \mathbf{k}, \mathbf{r})|^2 d\mathbf{r}, \tag{3.22}$$

where $\hat{P}$ is an angular momentum projection operator with origin at the site α.

The partial density of states (PDOS) are then determined by integrating the $Q_l^{(\alpha)}(\epsilon, \mathbf{k})$ over all $\mathbf{k}$ in the Brillouin zone (BZ)

$$N_l^{(\alpha)} = \int_{BZ} Q_l^{(\alpha)}(\epsilon, \mathbf{k}) d\mathbf{k}, \tag{3.23}$$

and the total density of states is taken as the the sum over all orbitals and atoms

$$D(E) = \sum_{\alpha} \sum_{l} N_l^{(\alpha)}.$$

3.4.5 Linear optical properties

The linear optical properties in solids can be described with the complex dielectric function $\varepsilon(\omega) = \varepsilon_1(\omega) + i\varepsilon_2(\omega)$, the interband contribution to the imaginary part of $\varepsilon(\omega)$ is calculated by summing transitions from occupied to unoccupied states over the Brillouin zone, weighted with the appropriate momentum matrix elements.

The imaginary, or absorptive part of the dielectric tensor, $\operatorname{Im}\varepsilon(\omega)$, is given by [8]

$$\operatorname{Im}\varepsilon(\omega) = \varepsilon_2(\omega) = \frac{4\pi^2 e^2}{m^2\omega^2} \sum_{i,j} \int \langle i|M|j\rangle^2 (f_i(1-f_j)) \delta(E_f - E_i - \hbar\omega) d^3k, \tag{3.24}$$

where e and m are the electron charge and mass, respectively, ω is the frequency of the photon, M is the momentum operator, $|i\rangle$ is the wave function, corresponding to the eigenvalue E_i, and f_i is the Fermi distribution for $|i\rangle$ state. The real, or the dispersive, part of the dielectric tensor, $\operatorname{Re}\varepsilon(\omega)$, is obtained from the imaginary part by using the Kramers–Kronig relation

$$\operatorname{Re}\varepsilon(\omega) = \varepsilon_1(\omega) = 1 + \frac{2}{\pi} P \int_0^k \frac{\omega' \varepsilon_2(\omega') d\omega'}{\omega'^2 - \omega^2}, \tag{3.25}$$

where P implies the principal value of the integral. The integral over the Brillouin zone (BZ) was performed using the tetrahedron method.

The absorption coefficient α and the complex refractive index N are given by

$$\alpha = \frac{2\pi\omega}{c} \sqrt{\frac{-\operatorname{Re}(\varepsilon) + |\varepsilon|}{2}}, \tag{3.26}$$

$$N(\omega) = n(\omega) + \mathrm{i}k(\omega), \tag{3.27}$$

where

$$n(\omega) = \sqrt{\frac{|\varepsilon(\omega)| + \mathrm{Re}\,\varepsilon(\omega)}{2}}, \tag{3.28}$$

$$k(\omega) = \sqrt{\frac{|\varepsilon(\omega)| - \mathrm{Re}\,\varepsilon(\omega)}{2}}. \tag{3.29}$$

The reflectivity for normal incidence is given by the following expression

$$R(\omega) = \frac{(n(\omega) - 1)^2 + k^2(\omega)}{(n(\omega) + 1)^2 + k^2(\omega)}. \tag{3.30}$$

BIBLIOGRAPHY

[1] D. Singh. *Planes waves, pseudo-potentiels and the LAPW method*. Kluwer Academic Publishers, Boston, Dortrecht, London, 1994.

[2] O.K. Anderson, Phys. Rev. B **12** (1975)

[3] F. D. Murnaghan. *Proc. Natl Acad. Sci, USA*, **30** (1944) 244.

[4] M. J. Mehl, B. M. Klein and D. A. Papaconstantopoulos, *Intermetallic Compounds*: *Principles and Practice*, Volume I: *Principles*, J. H. Westbrook and R. L. Fleisher, eds., John Wiley and Sons (London, 1995) Ch. 9 (pp. 195–210).

[5] P. Blaha, K. Schwarz, G. K. H. Madsen, D. Kvasnicka and J. Luitz. *WIEN2k, An Augmented Plane Wave + Local Orbitals Program for Calculating Crystal Properties*. Karlheinz Schwarz, Techn. Universität Wien, Austria, 2001. ISBN 3-9501031-1-2.

[6] M. B. Kanoun, A. E. Merad, G. Merad, J. Cibert and H. Aourag, Solid–State Electronics, **48** (2004) 1601.

[7] G.L.W. Hart and A. Zunger, Phys. Rev. B **62** (2000) 13522.

[8] C. Ambrosch-Draxl and J.O. Sofo. *Linear optical properties of solids within the full-potential linearized augmented plane wave method*. preprint, arXiv: cond–mat/0402523, Feb 2004.

CHAPTER 4

Electronic and optical properties of GeTe, SnTe and PbTe

4.1 Introduction

The IV–VI semiconductors AB (A=Ge, Sn, Pb; B=S, Se, Te) have been objects of investigation for a long time on account of their interesting properties like high dielectric constant and narrow fundamental gap whose pressure coefficient is negative for PbTe, i.e., it decreases as pressure is applied, and it is positive for SnTe. The narrow gap semiconductors are very suitable materials as infrared detectors and light emitting devices [1]. SnTe is a p-type semiconductor with a deficiency of tin atoms [2], it has been shown that SnTe is a good candidate for observing acoustic plasmons by using a model dielectric tensor based on the random phase approximation (R.P.A.) with an analytic continuation to the lower half of the complex frequency plane [3, 4].

The band structures of these compounds have been calculated using many different methods such as the empirical pseudo potential [5–10], the augmented plane wave method [11, 12], the full potential linear muffin tin orbital (FP–LMTO) [13], linear augmented plane wave method [14–16]. In the cubic phase, all of them gave results with general features in common, for exemple, the direct bandgap is at the L point in the brillouin zone for PbTe and near it for

SnTe. Experimental information relevant to the band structure has been obtained from the measurement of various quantities [17–22].

The optical properties have been investigated both theoretically [8, 10, 13, 14] and experimentally; near normal incidence of Cardona and Greenaway [23], the wavelength modulated reflectivity of Kohn et al. [8] and Korn and Braunstein on the $Pb_{1-x}Sn_xTe$ alloy system [24] and more recently the ellipsometry measurements [25–28].

Recently, Okoye [14] has used the the FP–LAPW method within the local density and the generalized gradient schemes to calculate some of the optical properties for SnTe and GeTe in the rocksalt structure. However, there is a crucial dependence of the results on the Brillouin zone sampling as was mentioned by Ambrosch–draxl et al. [29], thus using a dense mesh and taking into account of the spin orbit interaction might seem necessary in order to compare the calculated properties to the experimental data.

In this chapter we show the effect of the k sampling in the irreducible part of the Brillouin zone (IBZ) on the optical spectra on one hand, and on the other we give a comparative and a complementary study of the optical properties to both experimental and other works for GeTe, SnTe and PbTe. After a description of the calculations details in section 4.2, the results and discussions are presented in section 4.3. Finally, a conclusion is given.

4.2 Details of calculation

In this work, we use the full potential linearized augmented plane wave method, which has been described elsewhere [30]. The calculations have been carried out using the wien2k code [31]. As exchange and correlation potential the Perdew–Wang scheme [32] is used. The crystallographic structure is required as experimental input. The crystal structure of the compounds GeTe, SnTe and PbTe is rocksalt. The full space group is Fm3m which has 48 symmetry operations which includes inversion symmetry. In the calculation 453, 537, and

569 plane waves have been used for the expansion of the charge density and the potential in the interstitial region for GeTe, SnTe and PbTe, respectively, and lattice harmonics up to l=10 for the expansion in the muffin tin spheres. The muffin tin radii were chosen to be 2.4 Bohr, for the Ge, Sn and Te atoms, and 2.5 Bohr for Pb atom. A satisfactory degree of convergence was achieved by considering a number of LAPW basis up to $R_{MT} \times K_{max}$=8, where R_{MT} denotes the smallest atomic radius and K_{max} gives the magnitude of the largest k vector in the plane wave expansion. For the self consistent calculation, the Brillouin zone integration has been performed with 47 points in the IBZ.
To ensure convergence the variation of the total energy and the values of the energy of the highest valence and lowest conduction bands have been calculated in function of the number of k points and $R_{MT} \times K_{max}$. It is worth noting that the muffin tin radii are also varied to satisfy convergence.
For the calculation of optical spectra the integration over the Brillouin zone (BZ) was performed using the tetrahedron method. As pointed out by Ambrosch-Draxl [29] that the calculated optical spectra depend on the BZ sampling, therefore we varied the number of k point in the BZ in order to see the convergence with respect to the BZ sampling.
It is worth noting that all calculations have been performed with spin orbit, this effect is very important since the splitting of the bands contributes to the optical transitions.

4.3 Results and discussions

4.3.1 Structural properties

The equilibrium parameters are obtained by calculating the total energy for several values of the volume around the experimental one, then the calculated values are fitted to the Murnaghan's equation of state [34]. The results for the three compounds are illustrated in figure 4.1 and summarized in table 4.1 together with other theoretical and available experimental data. We included

the results obtained by the GGA [35]. The LDA equilibrium lattice constants are used in calculating the density of states band structure and the optical properties.

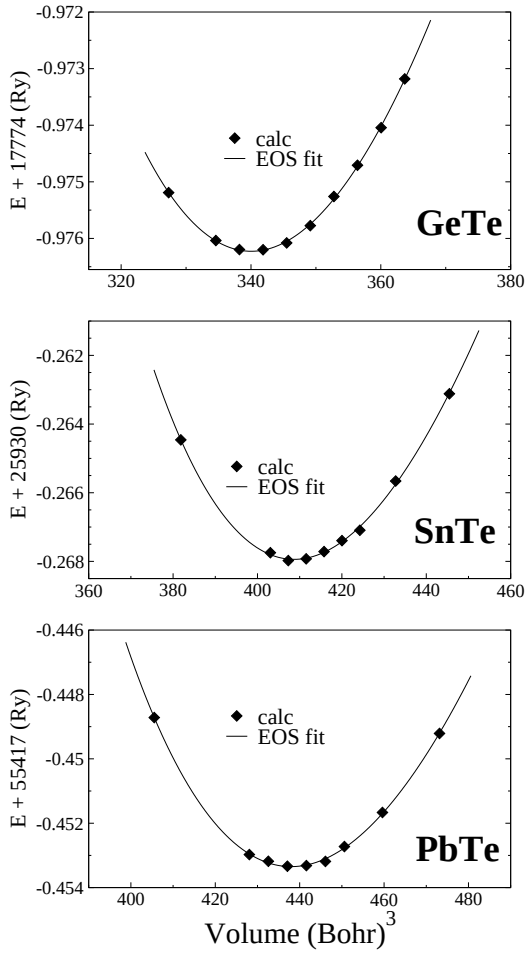

Figure 4.1: Energy versus volume, the filled diamond represents the calculated total energy while the lines are the fit to the Murnaghan's equation of state.

Table 4.1: Structural parameter, lattice parameter a_{eq} in (Å) , Bulk modulus B in (GPa) and its pressure derivative B'

	Calc. (Present results)		Other calculations		Expt.
	LDA	GGA	LDA	GGA	
GeTe					
a_{eq}	5.86	6.01	5.85[a]	6.01[a]	5.99[e]
B	60.43	48.28	60.01[a]	48.93[a]	
B'	3.77	4.16	60.01[a]	48.93[a]	
SnTe					
a_{eq}	6.23	6.40	6.23[a]	6.40[a]	6.313[e]
			6.23[b]		
B	50.74	40.91	50.75[a]	40.06[a]	
			51[b]		
B'	4.88	5.37	4.47[a]	4.25[a]	
PbTe					
a_{eq}	6.38	6.56	6.37[b]	6.56[c]	6.462[f]
			6.44[d]		
B	49.40	37.56	51.4[c]	41.4[c]	39.8[f]
			51.7[d]		
B'	4.26	4.93	4.08[c]	3.35[c]	

[a] Ref [14],
[b] Ref [7],
[c] Ref [16],
[d] Ref [15],
[e] Ref [9],
[f] see Ref [16].

4.3.2 Electronic properties

The optical properties are closely related to the electronic structure, thus the knowledge of it and the possible electronic transitions (band structure) as well as their origins (energy level) are very useful and fruitful in analyzing the optical spectra. In figure 4.3 we present the total density of states (TDOS) of GeTe, SnTe and PbTe along with the experimental data. As it is easily seen that the main features are preserved in the structures. The agreement with the experiment is good.

The calculated band structures are displayed in figure 4.3 together with the effect of spin orbit interaction of the three compounds studied. The partial

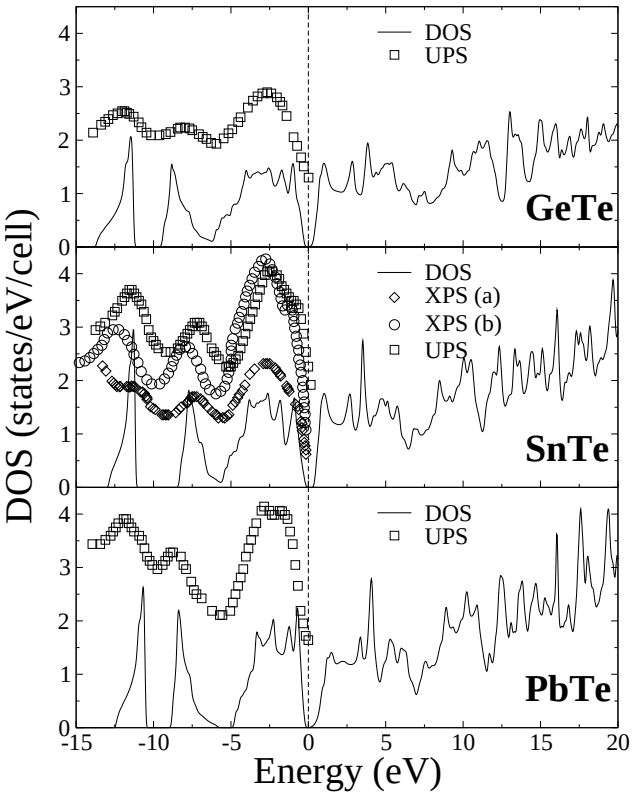

Figure 4.2: Total density of states of GeTe, SnTe and PbTe compared to the available XPS, (a) Shalvoy et al., (b) Kemeny and Cardona, and UPS Fukui [36] data. The data (a) and (b) are taken from Ref. [37].

density of states (PDOS) is plotted in the right panels. The calculated band structure and DOS show similarities for the studied compounds. The first peak reflects the s Te electrons, which corresponds to the lowest lying bands in figure 4.3, and its width originates mainly from region around Γ point in the BZ, since only there the dispersion of this band is appreciable. The second one the s X (X=Ge, Sn, Pb) electrons and the rest of the valence band is mainly due to the p electrons of both elements in the compounds. The conduction bands are mainly formed by the telluride and the X(X=Ge, Sn, Pb) p states, furthermore, above 6 eV there is a contribution from the d states. We note that the positions of the peaks shift down in energy as the column IV is traversed upwards, the same trend is observed in the calculated band structures of figure 4.3. The spin orbit interaction has a reverse effect on

the fundamental gap of Ge(Pb) and SnTe, since it decreases the gap at L for GeTe and increases it for SnTe as it is shown in table 4.2. The decrease of the gap is due to the lowering of the energy level of the first conduction band at the L point.

Table 4.2: LDA and GGA energy gap both with and without spin orbit, and results from experiment and other calculations, note that the data taken from Ref [14] and [16] are calculated at the experimental lattice parameter

	Calc. (without SO)		Calc. (with SO)		Other calc.		Expt.
	LDA	GGA	LDA	GGA	LDA	GGA	
GeTe	0.16	0.37	0.03	0.22	0.24[a],	0.20[a]	0.10 (300° K)[d]
							0.20 (4.2° K)[d]
SnTe	0.03	0.05	0.26	0.10	0.22[a]	0.21[a]	0.20 (300° K)[d]
							0.30 (4.2° K)[d]
PbTe	0.58	0.82	0.08	0.18	0.64[b]	0.18[b]	0.19[e]
					0.19[c]		0.32 (300° K)[f]

[a] Ref [14],
[b] Ref [16],
[c] Ref [15],
[d] Ref [20],
[e] see Ref [16],
[f] Ref [17].

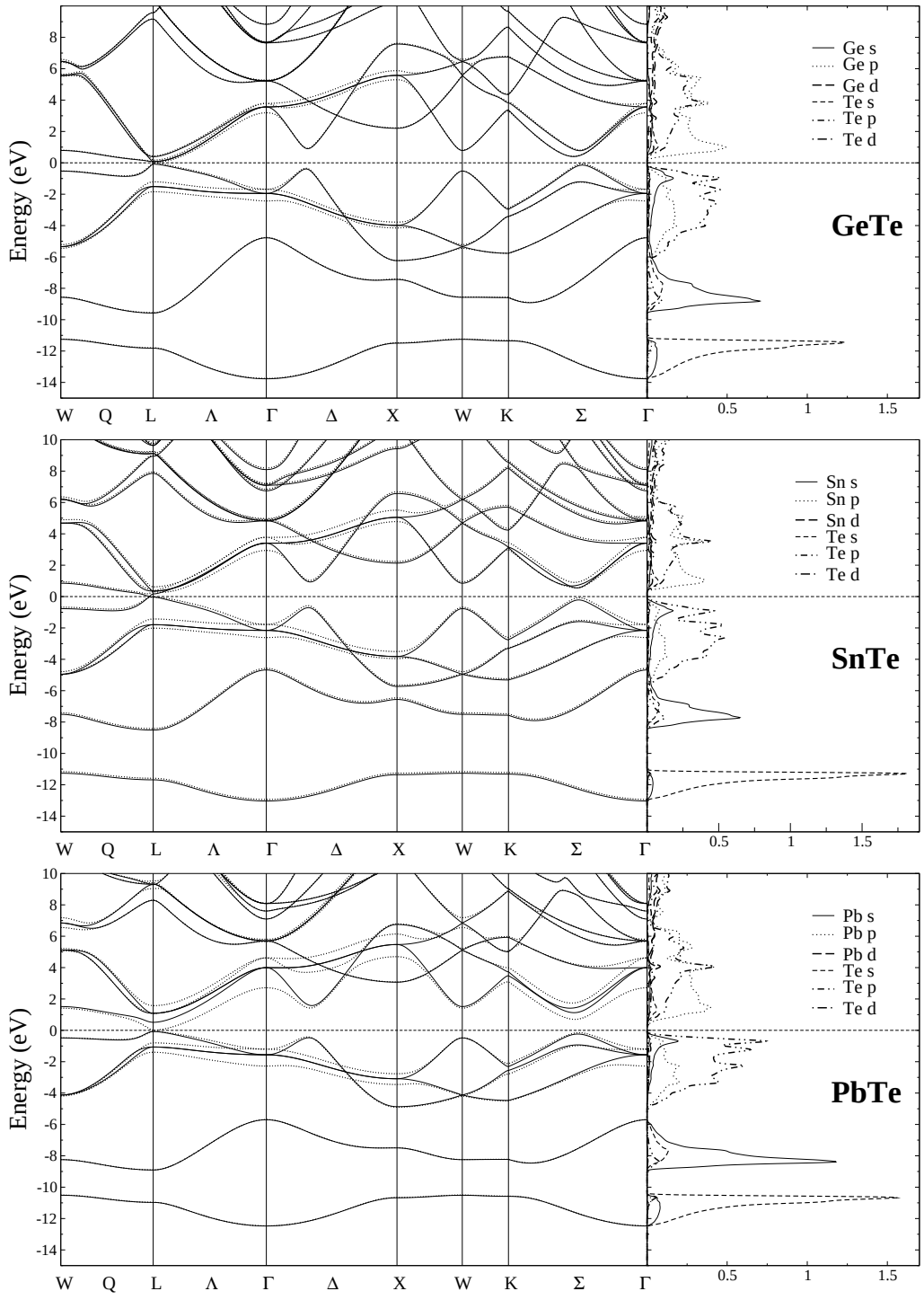

Figure 4.3: Band structure of GeTe, SnTe, and PbTe along high symmetry directions in the Brillouin zone with (dotted) and without (solid lines) spin orbit interaction. In the right panels the partial density of states are displayed. The Fermi energy is at zero.

4.3.3 Optical properties

We start the discussion of the optical properties by studying the effect of the BZ sampling on the imaginary and the real parts of the dielectric function for the three compounds. Figure 4.4 shows the variation of ε_2 and ε_1 of SnTe with respect to the k point meshes. The graph in the inset shows our calculated ε_2 using 2456 points in the IBZ compared to the one obtained by Okoye [14] and the experimental one of Suzuki and Adachi [27]. It is clear that with increasing the number of k points the structures and the peaks in the ε_2 spectra exhibit a pronounced energy shift to the lower values, as it does the onset of the absorption. The value of energy for which the real part of the dielectric function changes sign is also shifted to lower energies. The same results are found for the other two compounds. Only with the most dense mesh convergence is obtained and quantitative agreement with experimental data is achieved [29]. For the rest of the paper, the results are presented for the case of 2456 points in IBZ for SnTe and 4735 for GeTe and PbTe.

Our theoretical calculated absorptive and dispersive parts of the dielectric function for PbTe and SnTe are shown and compared to the experimental spectra [24, 25, 27, 28] in figure 4.5. For GeTe, no experimental spectra are available for us; we just show the calculated ones. The calculated absorptive spectra are not broadened. For PbTe a constant energy shift of 0.24 eV has been applied. Our calculated spectrum is in good agreement with that obtained by Delin et al. [13] using the FP–LMTO and Kohn et al. [8] obtained by the empirical pseudo potential. It is generally seen that the main features observed in the experimental data are well reproduced in our calculations.

Now, we turn to the examination of the origin of the different features in our calculated absorptive part of the spectra in terms of band to band transitions [38]. First, we decompose the calculated ε_2 in contributions from each pair of valence v_i, and conduction v_j bands (v_i,v_j). This is shown for the three materials studied in figure 4.6 (a). It is clear that the most features of

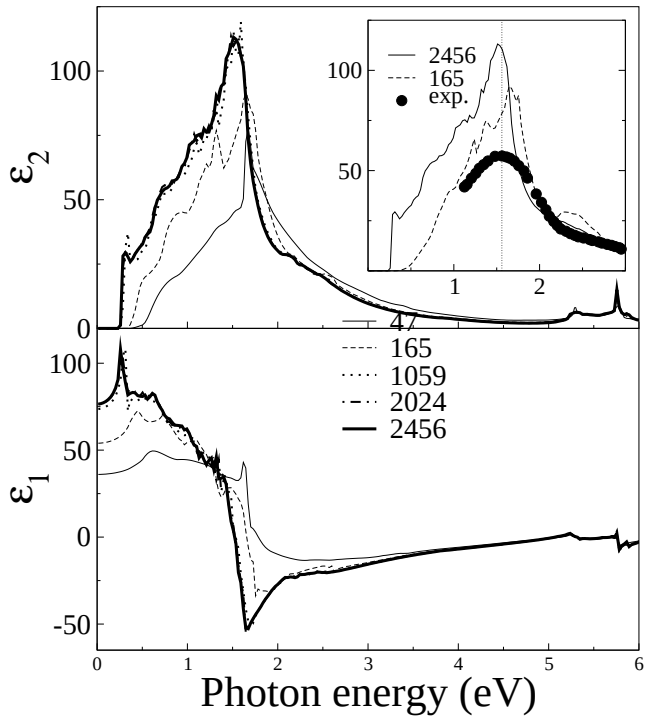

Figure 4.4: The frequency dependant dielectric function of SnTe for a series of k meshes in the BZ. In the inset our calculated imaginary part of the dielectric function with 2456 k points is compared to that obtained by Okoye [14] (with 165 points and without spin orbit) and the ellipsometry data of Suzuki and Adachi [27].

the spectra are due to the transitions between the top valence and the low lying conduction bands, i.e. (v_1,c_1). Secondly, since the most contributions to the joint density of states (JDOS), assuming that the matrix element of the momentum operator [24] do not vary much with k, are from those region in k-space where the bands are parallel. It is very meaningful to plot the band pair (valence-conduction) energy differences in the BZ, as illustrated in figure 4.6 (b), in which the counting for v(c) is down (up) from the top (bottom) of the valence (conduction) bands. The regions where the energy difference is constant correspond to regions of high density of states, and extremes correspond to Van Hove singularities [23, 24, 39]. On this basis, the ε_2 spectra can be interpreted as follow:

(i) An onset at the fundamental absorption edge comes from transition be-

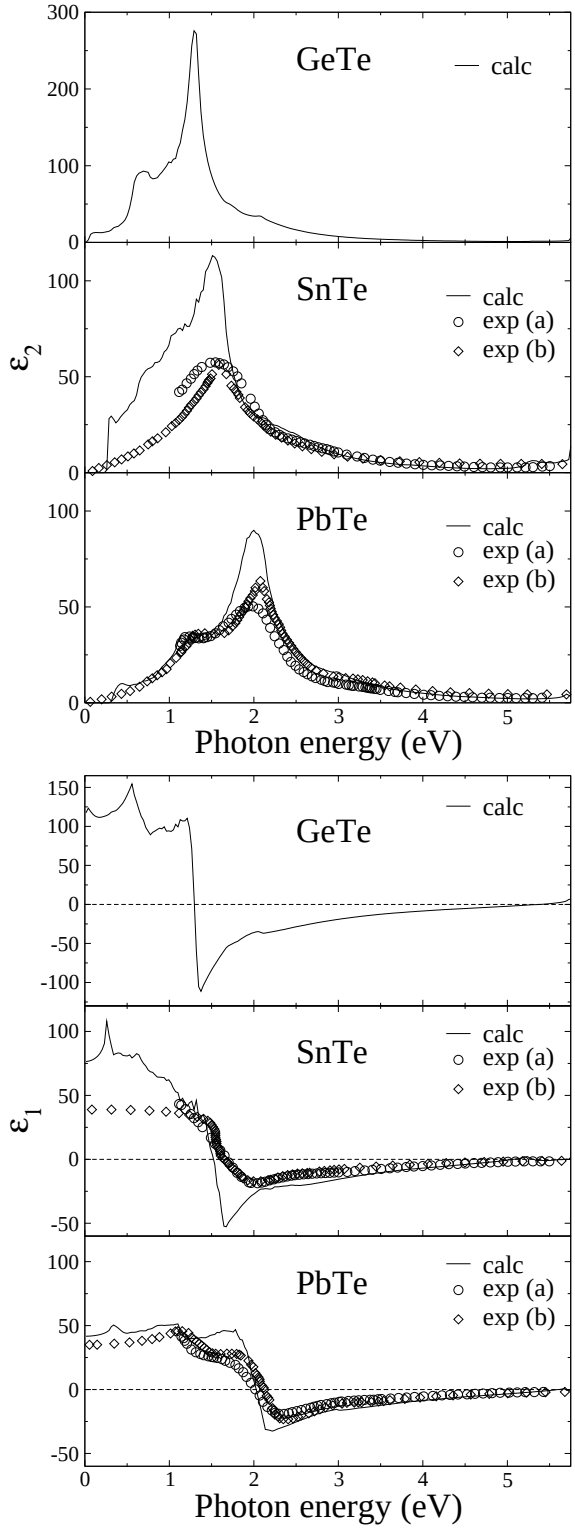

Figure 4.5: Calculated (solid line) and experimental absorptive and dispersive parts of the dielectric function. The experimental data are taken from (a) Refs. [25, 27, 28], and (b) Ref. [24].

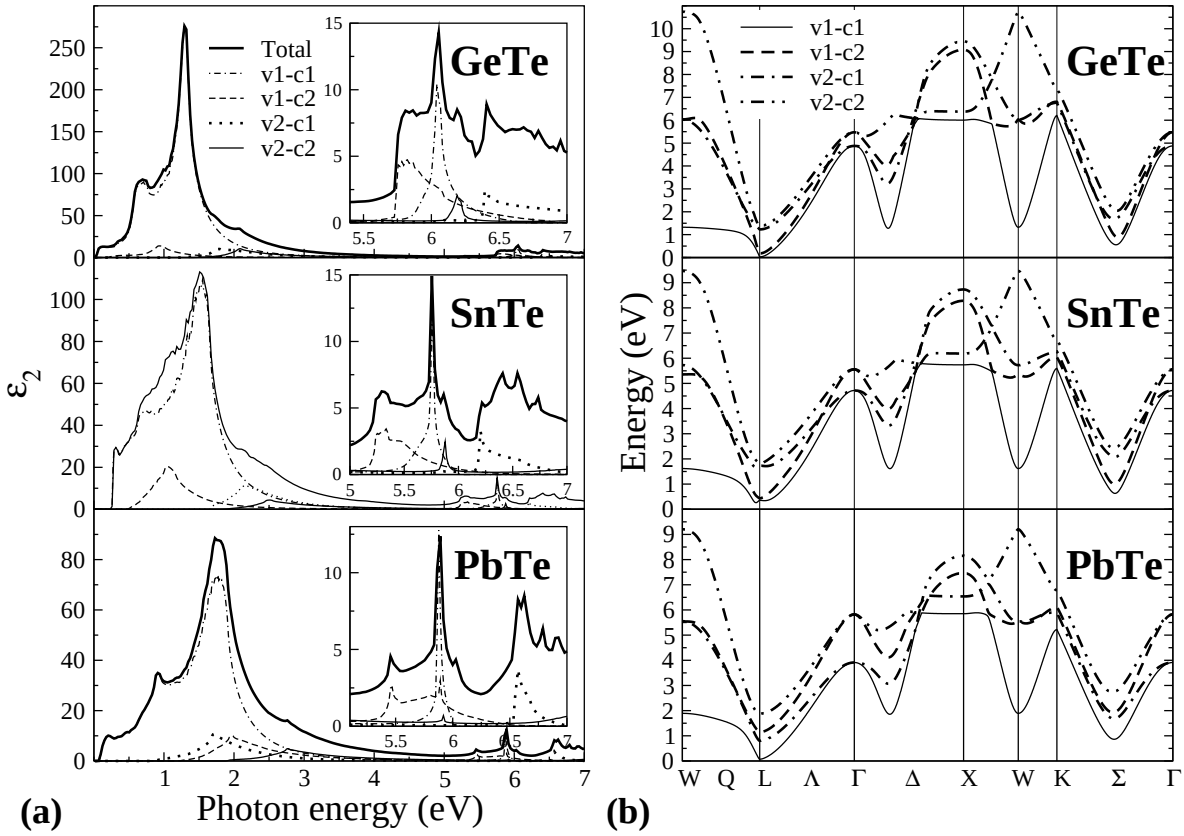

Figure 4.6: (a) decomposition of ε_2 in individual band-to-band contributions, and (b) transition band structures. The counting of the bands is down (up) from the top (bottom) of the valence (conduction) bands.

tween the extrema of the topmost valence band and the first conduction band at L for GeTe and PbTe and near it along the Q direction for SnTe. We note that this peak is sharper in SnTe than in the other two compounds.

(ii) A smal peak (structure) in the region around 0.7 eV for SnTe and GeTe, and 0.9 eV for PbTe, also comes from v_1–c_1 but along Σ and Δ lines in BZ.

(iii) Another structure around 1 eV for SnTe and GeTe, comes from the transitions between the topmost valence band and the second (lowest) conduction band (v_1–c_2) along the Σ lines in BZ.

(iv) The main broad peak, around 1.3 eV for GeTe, 1.6 eV for SnTe and 1.9 eV for PbTe, due to transitions between the two top valence bands (v_1,v_2) to the first (low) conduction band (c_1) along Σ line in BZ and the flat structure along Q line, where the topmost valence band and the first conduction band are pseudo parallel figure 4.3, and also at W. We must note that the contribution from (v_1–c_2) transitions to the main peak decreases in this order PbTe–SnTe–GeTe. This peak is the E_2 peak in Cardona and Greenaway work on the reflectivity measurements [23].

(v) The structures in energy range 1.6–2.47 eV for GeTe and 2–2.5 eV for SnTe and around 2.7 eV in PbTe, come from transitions between the second valence band to the two low conduction bands for GeTe and SnTe (v_2–c_1,c_2), and to the second conduction band for PbTe (v_2–c_2).

(vi) At higher energy the main features are; a relatively broad asymmetric peak around 5.80 eV for GeTe, 5.30 eV for SnTe and 5.4 eV for PbTe, due to transition v_1–c_2 along the X–W line, and a sharp peak around 6.0 eV for GeTe, 5.75 eV for SnTe and 5.88 eV for PbTe, due to transition from v1–c1 along Δ line (Γ–X) (as shown in the inset of figure 4.6 (b)).

The most striking feature which can be deduced from the discussion above is the shift in the energy positions of the peaks and structures when lead is substituted by an atom of the same column and smaller atomic number (Sn,Ge). This is in excellent agreement with the results of Ref. [23]. The same trend is observed in the calculated band structure and DOS.

The dispersive part of the dielectric function, ε_1, is shown in figure 4.6 (b) and with the available experimental spectra for PbTe and SnTe, but for GeTe we just show the calculated spectra. The general features observed in the energy range of the experimental data; that is a shoulder, followed by a step decrease, then ε_1 becomes negative and then it slowly increases towards zero, are well reproduced in our calculated spectra. Furthermore, the positions of the zeros of the calculated spectra are shifted down in energy when the column IV is crossed upwards.

Finally, the reflectivity, R, the absorption coefficient, α, and the real, n, and the imaginary, k, parts of the refractive index are calculated from the complex dielectric function by using the expressions 3.26–3.30. The results are displayed in figures 4.7 and 4.8 and compared with those obtained experimentally and by other calculations.

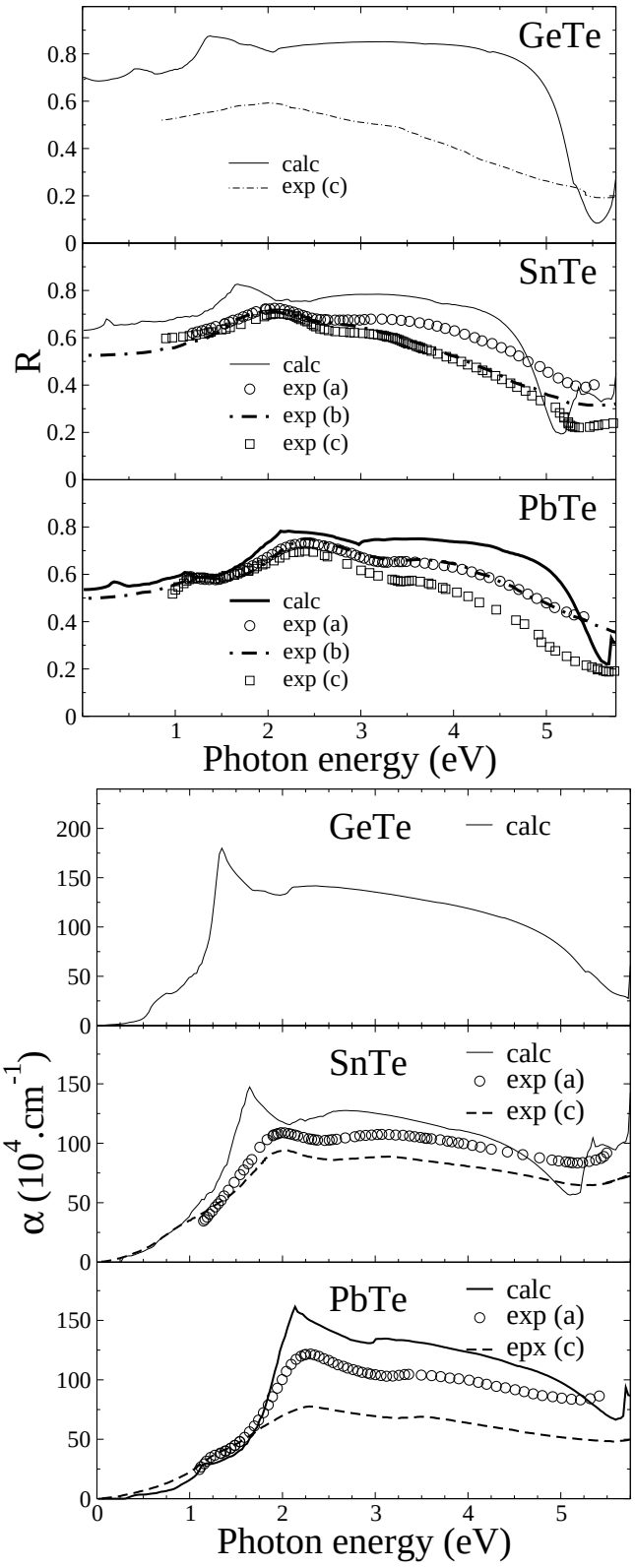

Figure 4.7: Calculated and experimental reflectivity (R) and absorption coefficient (α). The experimental data are taken from: (a) Refs. [25, 27], (b) Ref. [24], and (c) Ref. [23].

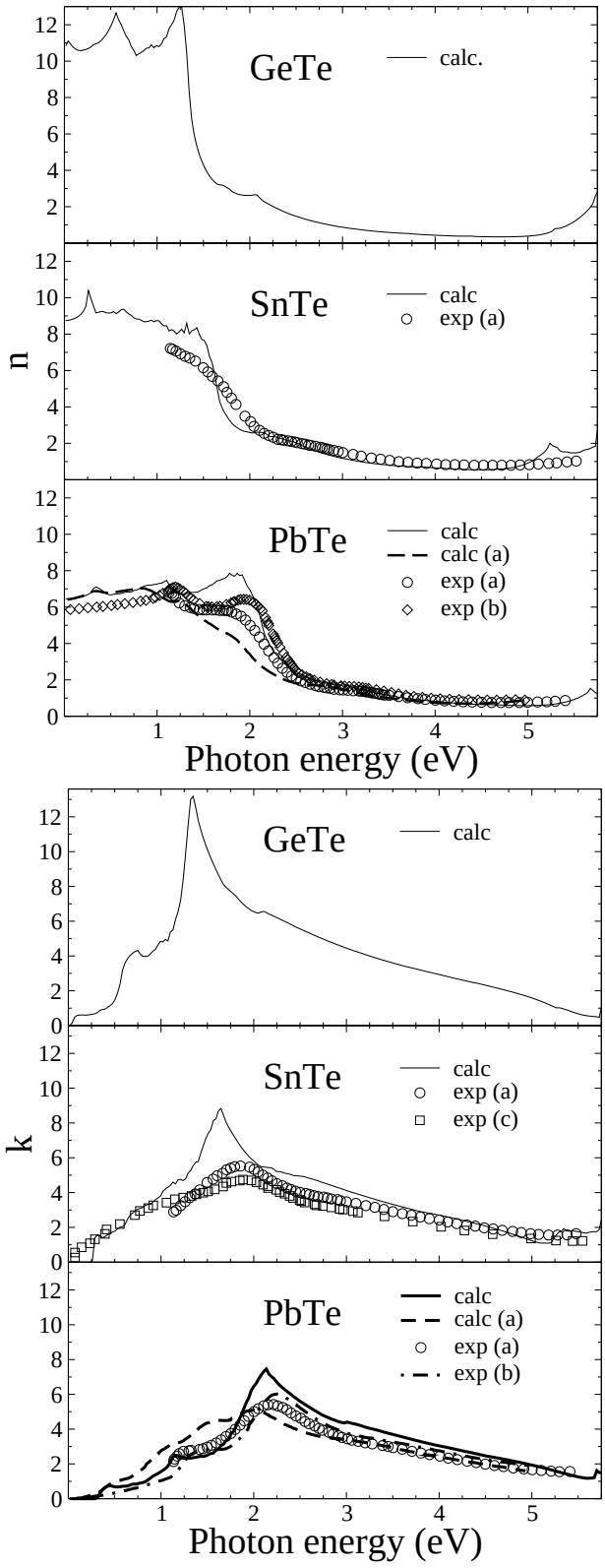

Figure 4.8: Calculated and experimental real, n, and imaginary, k, parts of the refractive index. The experimental data are taken from: (a) Refs. [25, 27], (b) Ref. [24]. For PbTe we compare our results to the theoretical ones (dashed) obtained by Buss et al. and which are taken from Ref. [24].

4.4 Conclusion

The optical spectra of GeTe, SnTe, and PbTe are successfully calculated using the FP–LAPW method. Increasing the density of the k–mesh in the BZ is shown to shift the structures and peaks positions to lower energies. The microscopic origin of the main features in the optical spectra is analyzed, and found that it is due to transitions between the highest valence and lowest conduction bands, which are both of p character. Furthermore, the contributions of the different regions in k–space are discussed in terms of the transition band structures. The positions of the main peak in the imaginary part of the dielectric function decrease through this sequence PbTe–SnTe–GeTe in the cubic phase. For SnTe and PbTe, our spectra are in good agreement with the experimental ones.

BIBLIOGRAPHY

[1] Y. Yang, W. Li, L. Yu, X. Sun, L. Xu and L. Hou. *Infrared physics and Technology*, 38 (1997) 9.

[2] R. S. Allgaier and B. Houston. *Phys. Rev.* ***B***, 5 (1972) 2186.

[3] B. Bennacer and A. A. Cottey. *Semicond. Sci. Technol*, 7 (1992) 822.

[4] B. Bennacer, A. A. Cottey and J. Senkiw. *J. Phys. Condens. Matter*, 1 (1989) 8877.

[5] M. L. Cohen and Y. W. Tsang. *The Physics of Semimetals and Narrow gap Semiconductors*. ed. D. L. Carter and R. T. Bate. Pergamon, New York, 1971. 303.

[6] Y. W. Tung and M. L. Cohen. *Physics Letters* ***A***, 29 (1969) 263.

[7] K. M. Rabe and J. D. Joannopoulos. *Phys. Rev.* ***B***, 32 (1985) 2302.

[8] S. E. Kohn, P. Y. Yu, Y. Petroff, Y. R. Shen, Y. Tsang and M. L. Cohen. *Phys. Rev.* ***B***, 8 (1975) 1477.

[9] M. L. Cohen, Y. W. Tung and P. B. Allan. *Journal de physique*, C4, 29 (1968) 163.

[10] H. M. Polatoglou, G. Theodorou and N. A. Economou. In Gornik et al, editor, *Physics of narrow gap semiconductors*, volume 152 of *Lecture notes in Physics*, pages 221–225. Springer, 1981.

[11] S. Rabii. *Phys. Rev*, 182 (1969) 821.

[12] J. S. Melvin and D. C. Hendry. *J. Phys.C: Solid State Phys*, 12 (1979) 3003.

[13] A. Delin, P. Ravindran, Olle Eriksson and J. M. Wills. *Int. J. Quntum Chem*, 69 (1998) 349.

[14] C. M. Okoye. *J. Phys.: Condens. Matter*, 14 (2000) 8625.

[15] Su–Huai and A. Zunger. *Phys. Rev.* ***B***, 55 (1997) 13605.

[16] M. Lach-hab, D. A. Papaconstantopolos and M. J. Mehl. *J. Phys. Chem. Solids*, 63 (2002) 833.

[17] M. Baleva and E. Mateeva. *Phys. Rev.* ***B***, 50 (1994) 8893.

[18] J. R. Burke, Jr, R. S. Houston, Jr, J. Babiskin and P. G. Siebenmann. *Phys. Rev. Lett*, 14 (1965) 360.

[19] L. Esaki and P. J. Stiles. *Phys. Rev. Lett*, 16 (1966) 1108.

[20] L. Esaki. *J. Phys. Soc. Japen*, 21 (1966) 589.

[21] A. G. Mikolaichuk and D. M. Freik. *Sov. phys. solide state*, 11 (1970) 2033.

[22] Y. Miamoto, H. Enomoto and H. Ozaki. *J. Phys. Soc. Japen*, 58 (1989) 2092.

[23] M. Cardonna and D. L. Greenaway. *Phys. Rev.* ***A***, 6 (1964) 1685.

[24] D. M. Korn and R. Braunstein. *Phys. Rev.* ***B***, 5 (1972) 4837.

[25] N. Suzuki and S. Adachi. *Jpn. J. Appl. Phys*, 33 (1994) 193.

[26] N. Suzuki, K. Swai and S. Adachi. *J. Appl. Physics*, 77 (1995) 1249.

[27] N. Suzuki and S. Adachi. *Jpn. J. Appl. Phys*, 34 (1995) 5977.

[28] N. Suzuki and S. Adachi. *J. Appl. Physics*, 79 (1996) 2065.

[29] C. Ambrosch-Draxl and J.O. Sofo. *Linear optical properties of solids within the full-potential linearized augmented plane wave method*. preprint, arXiv: cond–mat/0402523, Feb 2004.

[30] D. Singh. *Planes waves, pseudo-potentiels and the LAPW method*. Kluwer Academic Publishers, Boston, Dortrecht, London, 1994.

[31] P. Blaha, K. Schwarz, G. K. H. Madsen, D. Kvasnicka and J. Luitz. *WIEN2k, An Augmented Plane Wave + Local Orbitals Program for Calculating Crystal Properties*. Karlheinz Schwarz, Techn. Universität Wien, Austria, 2001. ISBN 3-9501031-1-2.

[32] J. P. Perdew. and Y. Wang. *Phys. Rev.* ***B***, 45 (1992) 13244.

[33] C. Ambrosch-Draxl and R. Abt. *The calculation of the optical properties within wien97*. (ICTP Lecture notes) 1998.

[34] F. D. Murnaghan. *Proc. Natl Acad. Sci, USA*, 30 (1944) 244.

[35] J. P. Perdew, S. Burke and M. Ernzerhof. *Phys. Rev. Lett*, 77 (1996) 3865.

[36] K. Fukui. *J. Phys. Soc. Japen*, 61 (1992) 1084.

[37] I. Lefebvre, M. A. Szymanski, J. Olivier–Fourcad and J. C. Jumas. *Phys. Rev.* ***B***, 58 (1998) 1896.

[38] W. L. Lambrecht and S. N. Rasheev. *Phys. Stat. Sol. (**b**)*, 217 (2000) 599.

[39] Peter Y. Yu and Manual Cardona. *Fundamentals of Semiconductors*. Third edition, Springer, 2001.

CHAPTER 5

Electronic and optical properties of Be_2C and Mg_2X (X=C,Si,Ge) under hydrostatic pressure

5.1 Introduction

Be_2C and Mg_2X (X=C, Si, Ge) are semiconductors having antifluorite structure which can be viewed as zinc–blende $M^{II}X^{IV}$ (M=Be, Mg; X=C, Si, Ge, Sn) filled by M^{II} atom [1]. This affects the crystal structure by changing the coordination of the X^{IV} atom from four fold coordinated in the diamond structure (e.g., Si, Ge) to eight fold coordinated in the antifluorite structure (e.g., Mg_2Si). But this structural change does not affect the electronic configuration of the molecule, since the number of valence electrons remains the same in both structures (i.e., diamond and antifluorite), moreover the Bravais lattice is also the same, thus the two structures possesse the same Brillouin zone (BZ), which results in a similar electronic structure [1, 2].

The antifluorite semiconductors are very interesting materials, they form the simplest metal–semiconductor hybrid materials [3]. The narrow gaps of Mg_2Si, Mg_2Ge and Mg_2Sn (0.3–0.6 eV) make them very suitable materials for technological application as infrared detector in the wave length range 1.2–1.8 μm relevant for optical fibers [4]. On the other hand due to the small size of Be and C atoms Be_2C and Mg_2C are expected to exhibit large elastic moduli, which

are related to hardness. Hence Be_2C and Mg_2C are very promissing materials for high temperature and pressure applications [5].
Although there have been numerous studies on the electronic and optical properties of these materials [1, 2, 5–12], but to the best of our knowledge there are no published works on the effect of pressure on these properties.
This chapter is devoted to the study of the evolution of these properties with pressure. The paper is organized as follows, in the following section we give the details of calculations. After that, we give the obtained results and discuss them in section 6.4, and finally a conclusion is given in section 6.5.

5.2 Details of calculation

The present calculations are performed using the full potential linearized augmented plane wave method [13] within the local density approximation (LDA) [14, 15], as implemented in the Wien2k code [16]. In this work we treat the core electrons fully relativistically, and the valence electrons scalar relativistically (all the relativistic effect are taken into account except the spin–orbit coupling).
In the calculations, the Be ($2s^2$), C ($2s^22p^2$), Mg ($3s^2$), Si ($3s^23p^2$) and Ge ($4s^24p^2$) states are treated as valence electrons, and the muffin–tin radii (in Bohr) are chosen to be 2.0 for Mg, Si and Ge atoms, and 1.45 for Be and C atoms. The basis functions are expanded up to $R_{mt} \times K_{max}$=8 (where K_{max} is the plane wave cut–off and R_{mt} is the smallest of all MT sphere radii), and up to l_{max}=10 in the expansion of the non–spherical charge and potential. We use the Perdew and Wang functional [17] for the exchange and correlation interaction. For the integration we used $10 \times 10 \times 10$ k–points mesh in the whole first Brillouin zone and the self–consistent calculations are considered to be converged when the total energy is stable within 0.1 mRy.

The linear optical properties in solids can be described with the complex

dielectric function $\varepsilon(\omega) = \varepsilon_1(\omega) + i\varepsilon_2(\omega)$, the interband contribution to the imaginary part of $\varepsilon(\omega)$ is calculated as described in chapter 3. The integral over the Brillouin zone (BZ) was performed using the tetrahedron method. The calculated optical spectra depend strongly on the BZ sampling, therefore a sufficiently dense k–mesh is used in the calculations of the optical spectra, which consists of $24 \times 24 \times 24$ k–mesh.

5.3 Results

5.3.1 Structural properties

Table 5.1: Structural parameters, lattice parameter a_0 in (Å), Bulk modulus B in (GPa), the Bulk modulus pressure derivative B' and cohesive energy E_c in eV/atom

	Parameters	Present work	Other calculations	Expt.
Be_2C	a_0	4.27	4.23[1], 4.27[2], 4.29[3]	4.34[4]
	B	219.6	215.9[1], 216[2], 213[3]	
	B'	3.09	3.5[2], 4.18[3]	
	E_c	6.10	5.86[2], 6.03[3]	5.08[4]
Mg_2C	a_0	5.36	5.00[1]	
	B	104.7	134[1]	
	B'	3.54		
	E_c	3.95		
Mg_2Si	a_0	6.26	6.09[1], 6.26[5], 6.295[6]	6.338[7], 6.35[8]
	B	58.84	59.2[1], 58.31[5], 56.2[6]	46.3–55.0[9]
	B'	3.97	4.023[5]	
	E_c	3.10		
Mg_2Ge	a_0	6.29	6.12[1], 6.286[5], 6.318[6]	6.393[7]
	B	56.12	57.6[1], 55.91[5], 55.10[6]	44.0–54.7[9]
	B'	4.31	4.051[5]	
	E_c	2.96		

[1]PWPP Ref. [11], [2]FP–LMTO Ref. [5], [3]LMTO–ASA Ref. [5], [4]Ref. [5] and references therein, [5]FP–LAPW Ref. [12], [6]PWPP Ref. [20], [7]Ref. [21], [8]Ref. [22], [9]Ref. [11] and references therein.

Antifluorite semiconductors Be_2C and Mg_2X (X=C,Si,Ge) can be considered as zinc–blende–like materials, with the atom which would be at $(\frac{1}{4}, \frac{1}{4}, \frac{1}{4})a_0$

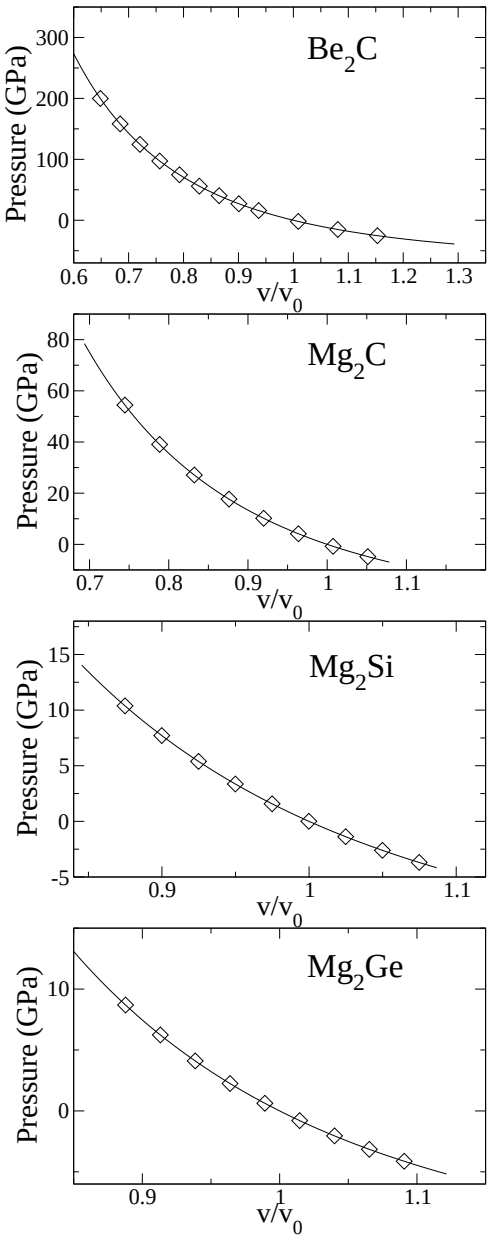

Figure 5.1: p(v) equation of state, v_0 is the equilibrium volume.

replaced by two Mg or Be atoms at $(\frac{1}{4}, \frac{1}{4}, \frac{1}{4})a_0$ and $(\frac{3}{4}, \frac{3}{4}, \frac{3}{4})a_0$, where a_0 denotes the lattice parameter. The ground state value of this parameter as well as the bulk modulus (B) and its pressure derivative (B') are obtained by calculating the total energy for several values of the unit cell volume and fitting them to the Murnaghan's equation of state (eos) [19]. The obtained results are listed in table 5.1, in which the available experimental data and results of other calculations are also shown. The calculated lattice parameters are about 1% lower than the experimental values for Mg_2Si, Mg_2Ge and Be_2C, while, the lattice parameter of the hypothetical compounds Mg_2C is larger than the previously reported value of Corkill and Cohen [11] calculated using the plane wave pseudo–potential (PW–PP) method. The bulk modulus of Mg_2Si and Mg_2Ge are higher than all the reported experimental values, this can be attributed to the LDA underestimation of lattice parameters. The lattice parameters and the bulk moduli agree well with the other calculations.

The energy–volume curves are very similar to the obtained ones by Benhelal et al. [12] using the same method. Since we are interested to the pressure effect, we have calculated the equation of state (the pressure versus volume) by taking the volume derivative of the fitted curves. The obtained results are depicted in figure 5.1. However, to the best of our knowledge, no experimental data are available to date, our results can be considered as prediction for future investigations.

5.3.2 Electronic properties

The zero pressure electronic band structures and optical spectra are calculated at the theoretical lattice constants. The energy band structure along principal symmetry directions at normal pressure and under pressure are depicted in figures 5.2–5.5 for the studied compounds. In these figures the valence bands are arbitrarily aligned. The band structures are quite similar for all the four compounds, with smaller differences in the details, with several features in

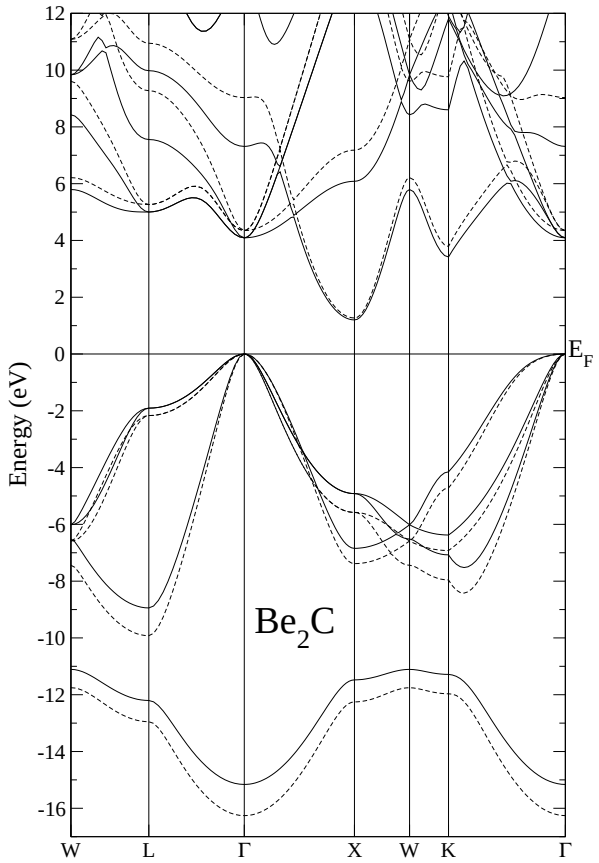

Figure 5.2: Energy band structure for Be_2C, along principal symmetry directions at normal pressure (full curves) and at 40.3 GPa (broken curves).

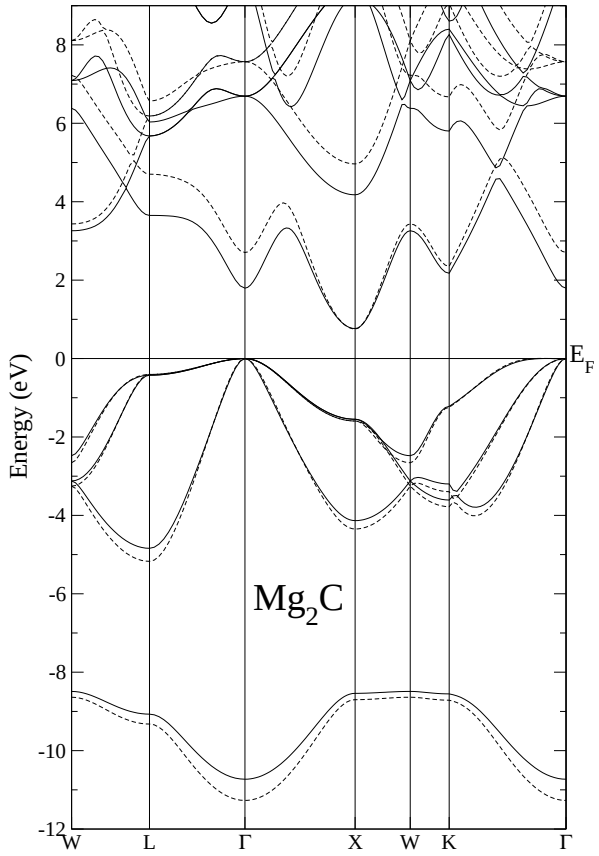

Figure 5.3: Energy band structure for Mg_2C, along principal symmetry directions at normal pressure (full curves) and at 17.7 GPa (broken curves).

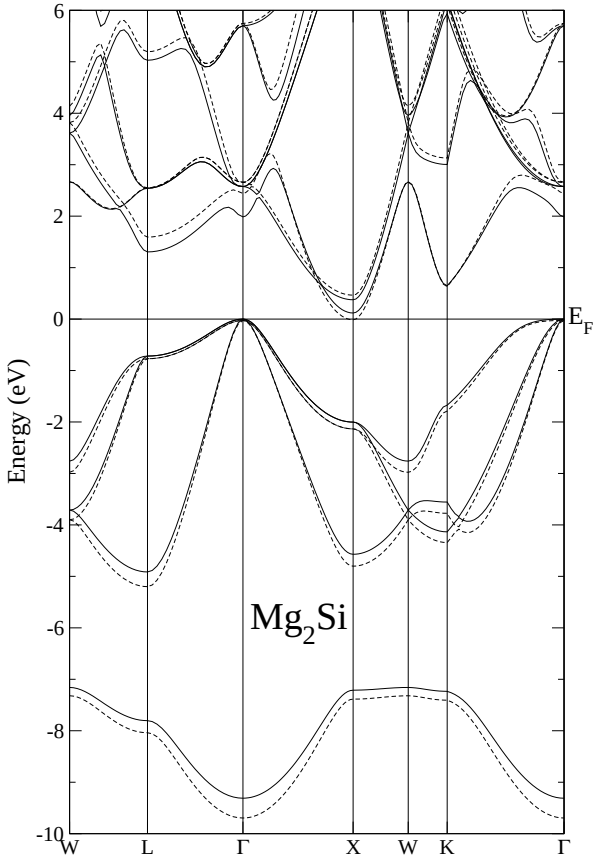

Figure 5.4: Energy band structure for Mg_2Si, along principal symmetry directions at normal pressure (full curves) and at 5.4 GPa (broken curves).

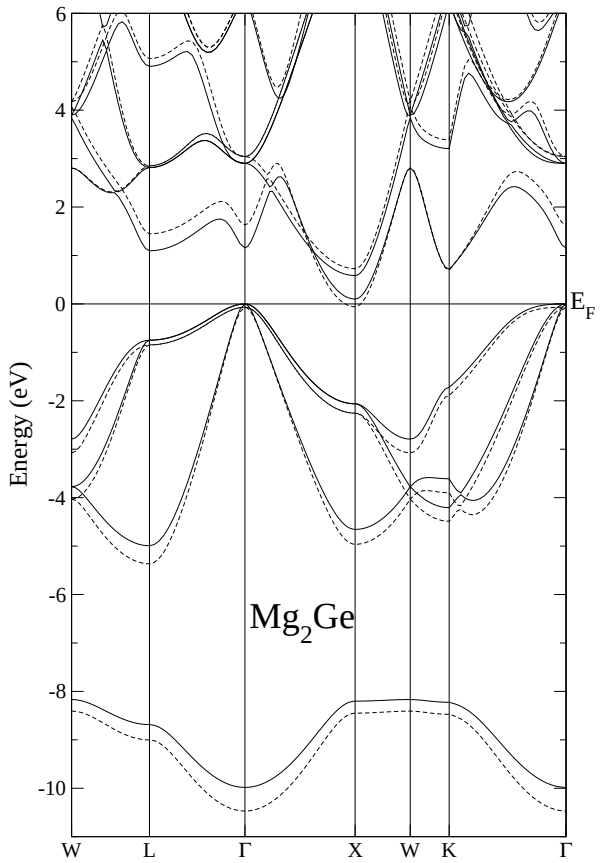

Figure 5.5: Energy band structure for Mg_2Ge, along principal symmetry directions at normal pressure (full curves) and at 6.7 GPa (broken curves).

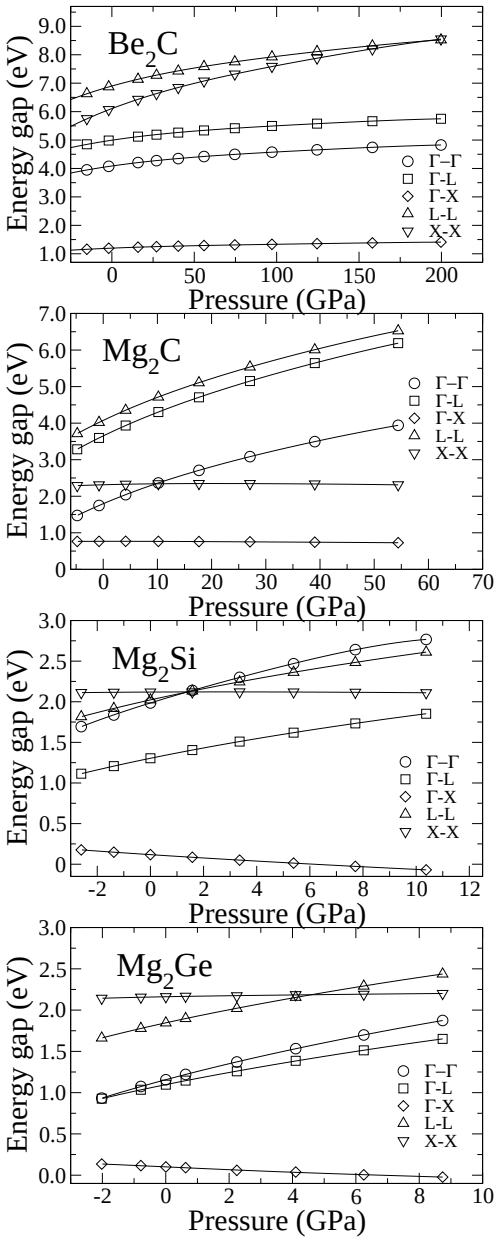

Figure 5.6: Variation of bandgaps as a function of pressure for Be_2C, Mg_2C, Mg_2Si and Mg_2Ge.

common with the IV, IIB–VI [23–25] and III–V [26–31] semiconductor compounds.

The valence bands can be divided into two groups. Starting from lower energy, the lowest bands consist mainly of the group IV atom s states. The second group of bands is mainly due to the group IV atom p–states hybridized with

Table 5.2: Bandgaps (in eV) and bandgap pressure coefficients a (meV/kbar) and b (meV/kbar^2)

Compound		$\Gamma-\Gamma$	$\Gamma-X$	$\Gamma-L$
C[1]	a	4.9	0.49	2.91
Si[1]	a	11.8	-1.9	3.73
Be_2C	$E(0)$	4.087305	1.198264	4.994781
	a	0.834453	0.237605	0.874447
	b	-0.000551	-0.000178	-0.000605
Mg_2C	$E(0)$	1.795377	0.766938	3.650250
	a	6.294564	0.019512	7.175434
	b	-0.007941	-0.000498	-0.008431
Mg_2Si	$E(0)$	1.983420	0.117929	1.303065
	a	10.388145	-2.140667	6.771665
	b	-0.026289	0.003787	-0.016904
Mg_2Ge	$E(0)$	1.155191	0.100224	1.095372
	a	10.331485	-1.718754	7.850679
	b	-0.026438	0.003169	-0.018896

[1]Ref. [36].

the Be and Mg p states. Continuing upward in energy, we see that all four compounds have a distinct energy gap, the maximum of the valence band is at the Γ point and the minimum of the conduction band is situated at the X point. The conduction bands are mixture of p and s states (see Ref. [12] for more details).

Under pressure the valence band energy levels decrease and consequently the valence band widths increase, whereas the conduction energy levels increase except at the X point of the lowest conduction band of Mg_2Si and Mg_2Ge where they decrease.

The LDA underestimates the bandgaps, but it reproduces the experimental trend quite well [32, 33]. The pressure derivatives and deformation potentials are given reasonably well within this approximation [34–36]. In this context and bearing in mind that the correction to this LDA effect is typically a rigid shift of the whole conduction bands, one might assume that the pressure coefficients of bandgaps within LDA, even underestimated [35,36], are more reliable

than the absolute gaps.

From the calculated equation of state and the gaps derived from band structure at various lattice parameters, we derived the first and second order pressure coefficients of the main transitions using polynomial fits. The variation of the direct and indirect gaps with pressure are shown in figure 5.6. The obtained values of the zero pressure gaps, the first and the second order pressure coefficients a and b, respectively, are listed in table 5.2.
As in the other diamond and zinc–blende semiconductors the linear coefficients are positive for the direct gap Γ–Γ and the indirect one Γ–L, while the coefficient of the Γ–X transition is negative except for the compounds containing the first row elements. Thus, the positive sign of $a^{\Gamma-X}$ coefficient for Be_2C and Mg_2C is in good agreement with the results found by Wei and Zunger [36] for C, GaN and AlN compounds which contain first row elements.
Be_2C and Mg_2Si are closely related to the C and Si [1, 5], respectively, our results show that under pressure the bandgaps of Be_2C and Mg_2Si follow the same behaviour as the homopolar column IV diamond–like semiconductors.
This trend was also encountered in the other FTC LiZnX (X=N,P,As) and their binary analogous GaX [37]. Comparing our results for Be_2C and Mg_2Si with the results of Wei and Zunger [36] for C and Si, respectively. We found that the coefficients of Mg_2Si are of the same order of magnitude as the Si ones. Whereas the Be_2C coefficients are substantially reduced relatively to the diamond ones, in contrast to what was found for LiZnN compared to GaN, where they are enhanced and this has been attributed to the significant reduction of LiZnN bulk modulus relatively to the one of GaN [37]. However, the bulk modulus value of Be_2C (219 GPa) is nearly half of that of diamond (442 GPa [38]), thus the pressure coefficients of Be_2C are expected to be larger than those of diamond.

As reported by Wei and Zunger [36] the bandgap pressure coefficients are altered by many effects, the volume effect (bulk modulus), the ionicity and the p–d coupling. Obviously, the smaller coefficients of Be_2C compared to diamond is not caused by p–d coupling effects, since both compounds lack an active d orbital. However, it has been shown in previous works [5, 9, 11], that Be_2C is an ionic semiconductor, and it is well known that diamond is the most covalent compound, therefore, the smaller coefficients of Be_2C might be attributed to the ionic character of this compound.
Another point worth noting is that Mg_2Si and Mg_2Ge become metallic as pressure increases (see Fig. 5.6) and the metallization pressures are 6.1 GPa and 6.7 GPa, for Mg_2Si and Mg_2Ge, respectively. While the two carbide compounds remain semiconductors in the range of the considered pressure.

5.3.3 Optical properties

The calculated imaginary part of the dielectric function under normal and under hydrostatic pressure for the studied compounds is shown in figure 5.7. The spectra of Mg_2Si, Mg_2Ge and Be_2C are quite similar. However the spectrum of Mg_2C is different from the others. This difference can be attributed to the position of the conduction bands which is quite different, for example, whereas the maximum of the valence band is at Γ, the conduction band valleys follow the X–L–Γ ordering of increasing energy for Mg_2Si and Mg_2Ge and X–Γ–L for Be_2C and Mg_2C. Furthermore, the Mg_2Si, Mg_2Ge spectra at zero pressure are similar to the ones obtained by Benhelal et al. [12]. The calculated onsets, which correspond to the threshold of absorption originate from the direct transition at the Brillouin zone centre are 4.09 eV, 1.80 eV, 1.98 eV and 1.16 eV for Be_2C, Mg_2C,Mg_2Si and Mg_2Ge, respectively. The last two values are very close to the ones reported in Ref. [12]. Furthermore, the assignment of the peaks and structures in the optical spectra and band structure transitions for Mg_2Si and Mg_2Ge are given in Refs. [8, 12]. Under pressure, we observe that

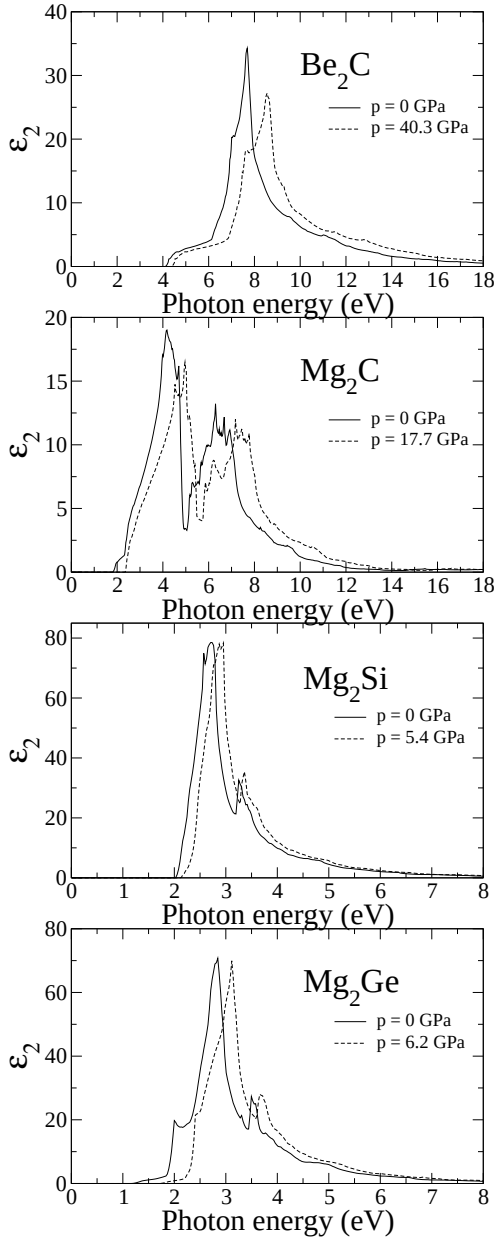

Figure 5.7: The imaginary parts of the dielectric function for Be_2C, Mg_2C, Mg_2Si and Mg_2Ge under normal and under hydrostatic pressure.

all the peaks shift to higher energies due to the increase of the bandgaps (as illustrated in figure 5.6).

The variation of the static dielectric constant ε_1 with pressure is also calculated for the studied compounds and the results are shown in figure 5.8. The LDA overestimates the values of ε_1. The static dielectric constant decreases

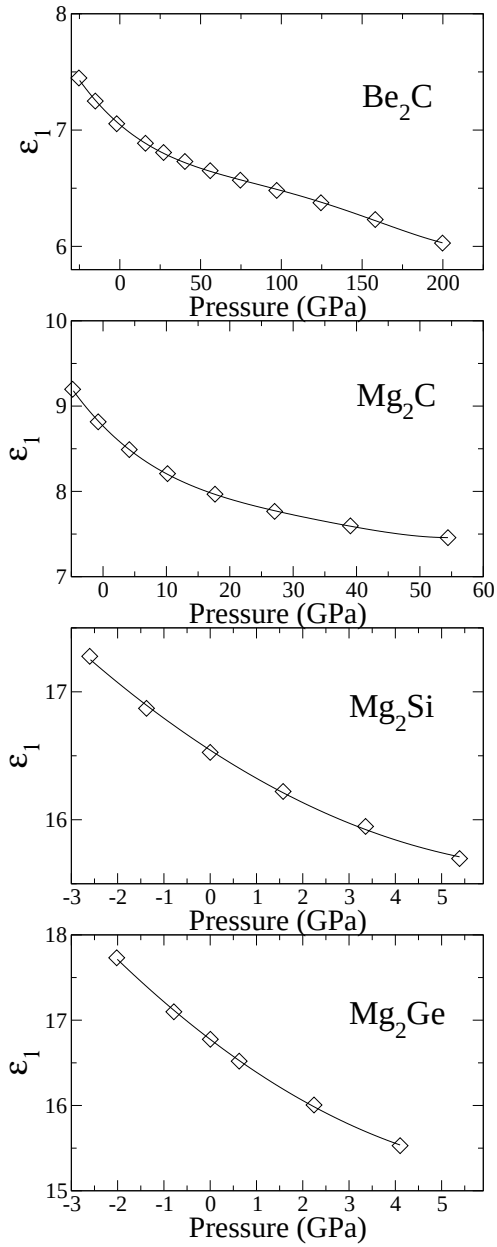

Figure 5.8: The variation of ε_1 as a function of pressure for Be_2C, Mg_2C, Mg_2Si and Mg_2Ge.

as the pressure increases for the semiconducting phase, its calculated values are adjusted using a polynomial fit and the first and second order pressure coefficients are displayed in table 5.3.

Table 5.3: The coefficients a and b of the static dielectric function ε_1, $\varepsilon_1(p) = \varepsilon_1(0) + ap + bp^2$, a (GPa^{-1}) and b (GPa^{-2}))

		$\varepsilon_1(0)$	a	b
Be_2C	This work	7.04716	-0.011844	0.000119
Mg_2C	This work	8.76655	-0.075923	0.002408
Mg_2Si	This work	16.54	-0.234658	0.014835
	Other	16.1827 [12]		
	Expt.	12.9 [7]		
Mg_2Ge	This work	16.78	-0.413175	0.027131
	Other	16.3626 [12]		
	Expt.	13.3 [7]		

5.4 Conclusion

We have used the FP–LAPW within the LDA in order to investigate the effect of pressure on the electronic and optical properties of the antifluorite Be_2C and Mg_2X (X=C,Si,Ge) compounds. The calculated pressure coefficients indicate that the $E_g^{\Gamma-\Gamma}$ and $E_g^{\Gamma-L}$ increase with pressure for all the studied compounds whereas $E_g^{\Gamma-X}$ increases with pressure for the carbide compounds and decreases for the other two and it is negative beyond 6.1 GPa for Mg_2Si and 6.7 GPa for Mg_2Ge. Furthermore, the smaller value of the first order pressure coefficient of Be_2C compared to diamond is attributed to the ionic character of the Be–C bond in this compound. The structures in the optical spectra shift towards higher energies when the pressure increases. The static dielectric function decreases with pressure.

BIBLIOGRAPHY

[1] D.M. Wood and A. Zunger, Phys. Rev. B **34** 4105 (1986).

[2] J. Tejeda and M. Cardona, Phys. Rev. B **14** (1976) 2559.

[3] B. Arnaud and M. Alouani, Phys. Rev. B **64** 033202 (2001).

[4] A. Vantomme, J.E. Mahan, G. Langouche, J.P. Becker, M. Van Bael, K. Temst and C. Van Haesendonck, Appl. Phys. Lett. **70** 1086 (1997).

[5] C.H. Lee, W.R.L. Lambrecht and B. Segall, Phys. Rev. B **51** (1995) 10392.

[6] F. Vasquez, R.A. Forman and M. Cardona, Phys. Rev. **176** (1968) 905.

[7] W.J. Scouler, Phys. Rev. **178** (1969) 1353.

[8] M.Y. Au–Yang and M.L. Cohen, Phys. Rev. **178** (1969) 1358.

[9] P. Herzig and J. Redinger, J. Chem. Phys. **82** (1985) 372.

[10] M.M. Disko, J.C.H. Spence, O.F. Sankey and D. Saldin, Phys. Rev. B **33** (1986) 5642.

[11] J.L. Corkill and M.L. Cohen, Phys. Rev. B **48** (1993) 17138.

[12] O. Benhelal, A. Chahed, S. Laksari, B. Abbar, B. Bouhafs and H. Aourag, phys. stat. sol. (b) **242** (2005) 2022.

[13] D. Singh. *Planes waves, pseudo-potentiels and the LAPW method*. Kluwer Academic Publishers, Boston, Dortrecht, London, 1994.

[14] P. Hohenberg and W. Kohn, Phys. Rev. B **136** (1964) 864.

[15] W. Kohn and L.J. Sham, Phys. Rev. A **140** (1965) 1113.

[16] P. Blaha, K. Schwarz, G.K.H. Madsen, D. Kvasnicka and J. Luitz. *WIEN2k, An Augmented Plane Wave + Local Orbitals Program for Calculating Crystal Properties*. Karlheinz Schwarz, Techn. Universität Wien, Austria, 2001. ISBN 3-9501031-1-2.

[17] J.P. Perdew. and Y. Wang, Phys. Rev. B **45** (1992) 13244.

[18] C. Ambrosch-Draxl, J.O. Sofo. *Linear optical properties of solids within the full-potential linearized augmented plane wave method*. preprint, arXiv: cond–mat/0402523, Feb 2004.

[19] F.D. Murnaghan. *Proc. Natl Acad. Sci, USA*, 30 (1944) 244.

[20] J–I. Tani and H. Kido, Lattice dynamics of Mg_2Si and Mg_2Ge Compounds from first–principles calculations, Comp. Mater. Sci. in press.

[21] E. Anastassakis and J.P. Hawranek, Phys. Rev. B **5** (1972) 4003.

[22] J. Zhang, Z. Fan, Y.Q. Wang and B.L. Zhou, Materials Science and Engineering A **281** (2000) 104.

[23] J.P. Walter, M.L. Cohen, Phys. Rev. B **1** (1970) 2661.

[24] N.E. Christensen, O.B. Christensen, Phys. Rev. B **33** (1986) 4739.

[25] Su–Huai Wei, A. Zunger, Phys. Rev. B, **37** (1988) 8958.

[26] J.P. Walter, M.L. Cohen, Phys. Rev. **183** (1969) 763.

[27] M. Alouani, L. Brey, N.E. Christensen, Phys. Rev. B **37** (1988) 1167.

[28] C. Persson, A. Zunger, Phys. Rev. B **68** (2003) 073205.

[29] K. Miwa, A. Fukumoto, Phys. Rev. B **48** (1993) 7897.

[30] K. Kim, W.R.L. Lambrecht, B. Segall, Phys. Rev. B **50** (1994) 1502.

[31] N.E. Christensen, Phys. Rev. B **30** (1984) 5753.

[32] F. Kalarasse and B. Bennecer, J. Phys. Chem. Solids **67** (2006) 1850.

[33] F. Kalarasse, B. Bennecer and A. Mellouki, J. Phys. Condens. Matter **18** (2006) 7237.

[34] S. Fahy, K.J. Chang, S.G. Louis and M.L. Cohen, Phys. Rev. B **35** (1987) 5856.

[35] S.–H. Wei, A. Zunger, I.H. Choi and P.Y. Yu, Phys. Rev. B **58** (1998) 1710.

[36] S.–H. Wei, A. Zunger, Phys. Rev. B **60** (1999) 5404.

[37] L. Kalarasse, A. Mellouki, B. Bennecer and F. Kalarasse, *Pressure effect on the optical properties of the filled tetrahedral semiconductors LiZnX (X=N,P, and As)*, J. Phys. Chem. Solids, in press.

[38] Peter Y. Yu and Manual Cardona. *Fundamentals of Semiconductors.* Third edition, Springer, 2001.

CHAPTER 6

Structural and elastic properties of the filled tetrahedral semiconductors LiZnX (X=N,P, and As)

6.1 Introduction

Among the filled–tetrahedral compounds (FTC), the Nowotny–Juza $A^{I}B^{II}C^{V}$ with (A^{I}= Li, Cu, Ag ; B^{II}= Be, Mg, Zn, Cd ; C^{V}= N, P, As, Sb, Bi) form a special class of semiconductors recognized as promissing materials for technological applications [1–3]. The main feature of these compounds is the change of the band structure from indirect to direct in comparison with the binary III–V analogous compounds leading to a new family of direct–wide bandgap semiconductors [2, 4].

Despite their interesting properties, the Nowotny–Juza compounds are less–investigated than the conventional III–V semiconductors. First principle techniques have been used to study the filling–induced change in electronic and optical properties for these compounds [1, 5–8] and very recently the vibrational spectrum of cubic LiZnAs has been calculated [9]. On the experimental side Kuriyama and his group studied the optical bandgap and determined the force constants for few members of this family [10–18]. However, the elastic constants and moduli which have been not yet calculated or measured (to the authors knowledge), are of extreme interest in both condensed matter theory

and technological fields. Many interesting properties of materials are closely related to them. For example, the bulk modulus is related to the hardness of the materials which is the key in high–temperature and pressure applications, and the elastic constants might provide valuable information about the bonding between adjacent atomic planes, the anisotropy character of bonding, structural stability and sound speeds. Therefore, a knowledge of the elastic properties of the filled tetrahedral compounds will be of great interest in understanding their behavior under different constraints.

The experimental determinations of all elastic constants need a single–phase, homogeneous and defect–free single crystal, so far, these conditions are not fullfilled in general for most of ternary alloys [19, 20] and in particular for FTC [3, 10–12, 18]. Theoretically, such single–crystal is assumed to exist through the periodic boundary conditions, and the full set of elastic constants and moduli can be directly obtained. For polycrystalline samples, the shear and young's moduli and Poisson's ratio can in principle be estimated from the elastic constants [19, 21].

In this work we initialize first–principles study of elastic properties of the filled compounds α–LiZnX (X=N, P, As) using the state of the art full potential linearized augmented plane wave method (FP–LAPW) [22, 23], in the framework of the density functional theory (DFT) within the local density approximation (LDA) [24,25]. Due to the absence of experimental measurements on the elastic constants of the three compounds, we also calculate the elastic constants of GaN, GaP, and GaAs for comparison and checking the reliability of our predicted results. The remainder of this paper is organized as follows: in section 6.2 we summarize the crystal structure of the FTC. The method and details of calculations are described in section 6.3. In section 6.4 we present the obtained results and discuss them. Finally, a conclusion is given in section 6.5.

6.2 Crystal structure

The zinc–blend crystal structure can be characterized by four lattice sites in unit cell namely $\tau_1 = (0,0,0)a_0$, $\tau_2 = (\frac{1}{4},\frac{1}{4},\frac{1}{4})a_0$, $\tau_3 = (\frac{1}{2},\frac{1}{2},\frac{1}{2})a_0$ and $\tau_4 = (\frac{3}{4},\frac{3}{4},\frac{3}{4})a_0$, where a_0 denote the lattice parameter. For zinc–blend–like structure DC compounds the cation D and the anion C atoms, occupy the τ_1 and τ_2 sites, respectively, whereas τ_3, τ_4 sites are empty, leading to the most minimal packing fraction (0.34) which is small than the half of the close–packed structure (0.74) which proves the effectiveness of sp^3 tetrahedral bonding in forming stable compounds [1]. Based on the openness of the zinc–blend structure, the small packing fraction, and the presence of two empty interstitial sites, Rompa et al., have proposed a simple method to modify the band structure of zinc–blend–like structure compounds by inserting a closed shell atom like He in one of the empty sites, their calculations indicate indirect–direct modification of the SiHe bandgap [4]. Later Wood and coworkers have proposed the *insertion rule* to describe the filling–induced change in the band structure of filled tetrahedral compounds [1].

The Nowotny–Juza compounds $A^IB^{II}C^V$ can be obtained by the transmutation of the cation atom (D^{III}) of the zinc–blend $D^{III}C^V$ to its isovalent pair A^I+B^{II} atoms, in this context the resulting compound can be viewed as Hypothetical zinc–blend $(B^{II}C^V)^-$ partially filled with $(A^I)^+$ interstitial ions [2]. Their crystal structure can be described as follows: the τ_1, τ_2 are occupied by the B^{II} and C^V atoms, respectively, and the A^I atoms can occupy, either the τ_3 site and forms the α–phase, or the τ_4 site which represents the β–phase [5]. The filling–induced change in the crystalline structure can be summarized as follows: (i) the insertion of the interstitial ion induce a dilation of the crystal cell, (ii) the change of coordination for the anion atom occupying the τ_2 site, from four–fold coordinated in the original zinc–blend structure to eight–fold coordinated in the filled one, and (iii) the additional interstitial atoms increase the packing fraction and the crystal becomes much denser than the original

zinc–blend parent.

6.3 Details of calculations

The present calculations are performed using the full potential linear augmented plane wave (FP–LAPW) [22, 23] within the local density approximation (LDA) [26]. In this work we treat the core electrons fully relativistically, and the valence electron semirelativistically (all the relativistic effect are taken in account except the spin–orbit coupling).

In the calculations, the Li ($2s^1$), N ($2s^2 2p^3$), P ($3s^2 3p^3$), Zn ($3d^{10} 4s^2$), Ga ($3d^{10} 4s^2 4p^1$) and As ($3d^{10} 4s^2 4p^3$) states are treated as valence electrons, and the muffin–tin radii (in Bohr) are chosen to be 1.8 for Li, 1.7 for N, and 2.2 for Ga, P, Zn and As atoms, we pointout that the radii of Ga and N atoms in GaN are reduced to 1.9 and 1.6, respectively, to avoid the overlap between spheres, and for the same raison the radius of P atom is reduced to 2.0 in GaP. The basis functions are expanded up to $R_{mt} \times K_{max} = 8$ (where K_{max} is the plane wave cut–off and R_{mt} the smallest of all MT sphere radii), and up to $l_{max} = 10$ in the expansion of the non–spherical charge and potential. We use the Perdew and Wang functional [26] for the exchange and correlation interaction. The integrations over the Brillouin zone are performed with $7 \times 7 \times 7$ k–mesh and the self–consistent calculations are considered to be converged when the total energy is stable within 0.1 mRy.

The theoretical equilibrium total energy, lattice parameter a_0, bulk modulus B and its first order pressure derivative B' are determined by fitting the total energy as a function of volume for both phases α and β to the Murnaghan's equation of state (eos) [27].

As it is well known that the elastic tensor of cubic crystals has only three independent elastic constants, namely c_{11}, c_{12} and c_{44}. Their determination requires knowledge of the curvature of the energy as a function of strain for selected deformations the unit cell. In this work, we adopt the same scheme

for deformations as those used by Kanoun et al. [28]: the elastic constants c_{11} and c_{12} are related to the bulk modulus B and can be computed by the Birch–Murnaghan eos [23] ; The two remaining deformations are : (i) a volume conservative tetragonal strain to calculate $c_{11}-c_{12}$; and (ii) rhombohedral strain to deduce c_{44}. The associated strain tensors as well as the full set of equations reliying the elastic constants to the strain–induced change in the total energy can be found in Refs. [23, 28].

6.4 Results

6.4.1 Structural properties

The calculated energy curves in function of volume for the two phases α and β of the three compounds are displayed in figure 6.1. The obtained total energy differences $E_\alpha - E_\beta$ (in meV per formula) are: -1673, -463 and -204, for LiZnN, LiZnP and LiZnAs, respectively, indicating that the α phase is the energetically favourable one. As it is clear from figure 6.1, the absence of common tangents between energy curves indicates that a pressure–induced phase transition from α to β is not possible in the studied pressure range. The rest of this paper will be devoted to the α phase only.

The results of structural optimization of α–LiZnX and zinc–blend GaX are listed in table 6.1, together with the available experimental data and results of other calculations. The lattice parameters and the bulk moduli for the binaries agree very well with the measured ones, the calculated B are 7% and 4.8% higher for GaN and GaP and 1.6% lower in GaAs than the experimental values. From table 6.1, the lattice parameters for LiZnN, LiZnP and LiZnAs are 4.80 Å, 5.61 Å, and 5.80 Å respectively, which are slightly less than the experimental values, this is mainly due to the LDA, but still predict an increase in volume for the ternaries compared to the binaries analogous compounds. The values of the bulk modulus (in GPa) are 141, 76, and 66 for the materials listed above, respectively, suggesting that the filling tends to slightly soften

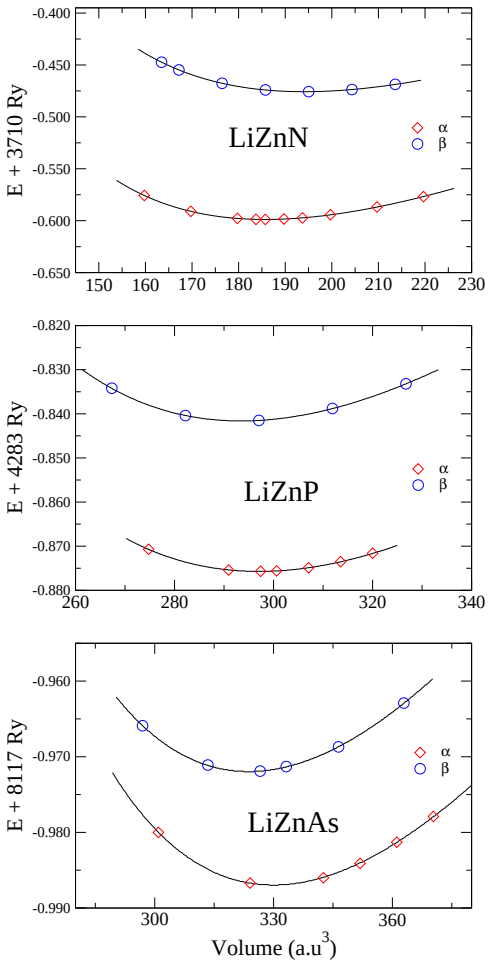

Figure 6.1: Energy versus volume for the α and β phases of the studied compounds. The circles and diamonds represent the calculated energies while the lines are the fits to the Murnaghan equation of state.

these materials, this can be associated to the volume increase in the filled compounds.

The bulk modulus pressure derivative falls within the range 4–5 as it the case for most solids.

6.4.2 Elastic properties

The calculated elastic constants are listed in table 6.2 together with the available experimental data and results of other calculation for GaN. The bulk modulus calculated from the theoretical values of the elastic constants $B =$

Table 6.1: Structural parameter, lattice parameter a_0 in (Å) , Bulk modulus B in (GPa), bulk modulus pressure derivative B' for the α–phase of filled LiZnX, and their parent zinc–blend GaX.

	Filled Compound			Binary Parents		
	This work	Other	Expt.	This work	Other	Expt.
	LiZnN			GaN		
a_0	4.80		4.87[1], 4.91[1]	4.46	4.446[2] 4.46[3]	4.5[4] , 4.49[5]
B	141			203	187–202[6]	190[5]
B'	4.2			4.5	3.9[7]	
	LiZnP			GaP		
a_0	5.61	5.64[8]	5.76[9], 5.75[10]	5.41		5.43[11], 5.45[12]
B	76			93.0		88.7[12]
B'	4.2			4.5		
	LiZnAs			GaAs		
a_0	5.8	5.768[8]	5.93[13]	5.61	5.55[14]	5.64[12]
B	66.9			73.8	73[14]	75.4[12]
B'	4.9			4.9		

[1] Ref [12], [2] Ref [30], [3] Ref [28,31,32,34], [4] Ref [31,32,34], [5] Ref [28], [6] Ref [28,30–32,34], [7] Ref [28,31,34], [8] Ref [9], [9] Ref [11], [10] Ref [3], [11] Ref [38], [12] Ref [37], [13] Ref [3,13], [14] Ref [29].

$(c_{11} + 2c_{12})/3$ is also listed in table 6.2, and it has nearly the same value as the one obtained from energy minimization (see table 6.1 for comparison) on one hand, and on the other it compares well with the one obtained from the experimental elastic constants. Furthermore, when analyzing carefully the results in table 6.2 and bearing in mind that the LDA underestimates the lattice parameter, consequently overestimates the elastic constants, and the neglect of the thermal motion the calculated c_{ij} for GaP and GaAs are in good agreement with experimentally measured values. This might be an estimate of the reliability of the calculational results for the ternaries.

All the calculated elastic constants in table 6.2 satisfy the mechanical stability criteria in cubic crystals [39]; $c_{11} - c_{12} > 0$; $c_{44} > 0$; $B > 0$. The overall trend in the elastic constants for the LiZnX series LiZnN–LiZnP–LiZnAs is similar to that for the GaX series GaN–GaP–GaAs, where all the c_{ij} are reduced, and also the bulk and shear wave moduli B and $c_s = (c_{11} - c_{12})/2$, respectively.

Table 6.2: Calculated elastic constants and moduli in (GPa) for the filled LiZnX, and their parent zinc–blend GaX.

	Reference	c_{11}	c_{12}	c_{44}	$B = (c_{11} + 2c_{12})/3$	c_s
LiZnN	This work	323.7	57.3	114.9	146.1	133.2
GaN	This work	290.0	167.0	210.0	208.0	61.5
	Other [31, 34]	296	154	206	201.3	71
	Other [35]	293	159	155	203.6	67
	Other [28]	274.2	166.1	199.0	202.1	54.0
	Expt.[1]	325	154	145	211	85.5
LiZnP	This work	149.2	47.7	76.0	81.5	50.7
GaP	This work	143.9	67.5	88.8	93.0	38.2
	Expt. [37]	141.2	62.3	70.5	88.6	39.4
LiZnAs	This work	120.6	40.2	70.7	67.0	40.2
GaAs	This work	136.1	45.9	75.6	75.9	45.1
	Other [29]	123	53	62	76.3	54.0
	Expt. [37]	118.1	53.2	59.4	74.8	32.4

[1] Obtained from hexagonal elastic constants of Ref [33] using Martin's method [36],

The velocities of the acoustic waves in solids are related to their elastic constants [40], for example for cubic crystals the velocity of the longitudinal wave in (110) direction is given by $\sqrt{(c_{11} + c_{12} + 2c_{44})/2\rho}$, where ρ is the density. From the theoretical elastic constants, we computed the ratio between the values of sound velocities in different directions (the density is calculated with the equilibrium volume) in the ternary and binary compounds, and found that it doesn't deviate much from unity for v_{LiZnAs}/v_{GaAs} and v_{LiZnP}/v_{GaP} (see table 6.3,and 6.4). This is in good agreement with the recent study of Wood and Strohmayer [9] on the vibrational spectrum of LiZnAs, in which they found that the sound velocities are quantitatively simmilar for LiZnAs and GaAs.

Table 6.3: Sound velocities in FTC for different propagation directions. The subscript L and T stand for longitudinal and transversal, respectively, and the superscript (hkl) indicates the propagation direction.

	v_L^{001}	v_T^{001}	v_L^{110}	v_T^{110}	v_L^{111}	v_T^{111}
LiZnN	7.90	4.71	7.67	5.07	7.60	4.95
LiZnP	6.20	4.42	6.70	3.61	6.86	3.90
LiZnAs	4.90	3.75	5.49	2.83	5.67	3.17

Table 6.4: Ratio between sound velocities in FTC and their zinc–blend binary analogous for different propagation directions, $r = v_{(FTC)}/v_{(Binary)}$. The subscript L and T stand for longitudinal and transversal, respectively, and the superscript (hkl) indicates the propagation direction.

	r_L^{001}	r_T^{001}	r_L^{110}	r_T^{110}	r_L^{111}	r_T^{111}
LiZnN vs. GaN	1.16	0.81	0.91	1.6	0.86	1.18
LiZnP vs. GaP	1.06	0.96	0.98	1.2	0.97	1.00
LiZnAs vs. GaAs	0.98	1.00	0.99	0.98	0.95	0.99

Having established the elastic constants c_{ij}, the elastic moduli for polycrystalline samples, shear modulus G, Young modulus E, and Poisson's ratio ν are calculated using the equations (3.20,3.19, 3.21), and the results are listed in table 6.5, which can be interpreted as follow:

(i) The large value of shear moduli are indications of the more pronounced directional bonding between atoms.

(ii) The small poisson's ratio for LiZnX ($\simeq 0.18$) than ($\simeq 0.24$) for GaX, indicate the relative stability against shear [21].

(iii) The quotient of bulk to shear modulus (B/G) is related to the ductility or brittleness of the crystal. The small values of this quotient ($\simeq 1.25 \ll 1.67$) show that the studied compounds are brittle rather than ductile materials (i.e., for cubic lattices the lower limit of ductility is $(B/G) = 1.67$ see Ref. [21] for more details.)

Finally, it is worthnoting that we are not aware of any experimental measurement or theoretical calculation of the elastic constants for the filled compounds, therefore our calculated values can be considered as prediction of these properties for the LiZnX materials, hoping that our study will stimulate some future works in this field.

Table 6.5: Elastic moduli in (GPa) and Poisson's ratio for polycrystalline samples of LiZnX and GaX, calculated using equations (3.19,3.20 and 3.21) from the data of table 6.2

	G_R	G_V	G	E	ν
LiZnN	121.6	122.2	121.9	286.2	0.17
GaN	96.00	141.0	118.5	297.6	0.25
LiZnP	63.4	65.9	64.6	153.4	0.18
GaP	53.6	58.0	55.8	138.4	0.24
LiZnAs	54.3	58.5	56.4	132.0	0.17
GaAs	44.6	48.6	46.6	115.9	0.24

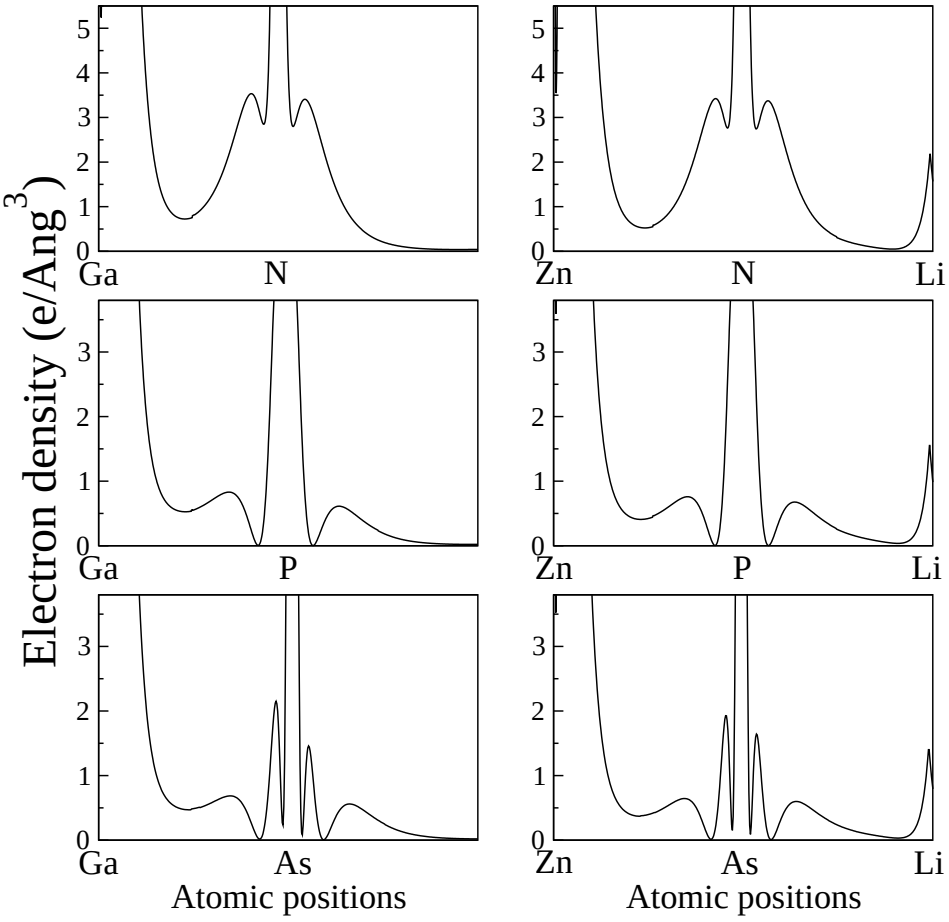

Figure 6.2: Electronic charge density profiles along the $< 111 >$ direction.

6.4.3 Valence charge density and bonding character

To obtain additional informations about the bonding properties, and to explain the large value of the elastic moduli, we have calculated the valence charge

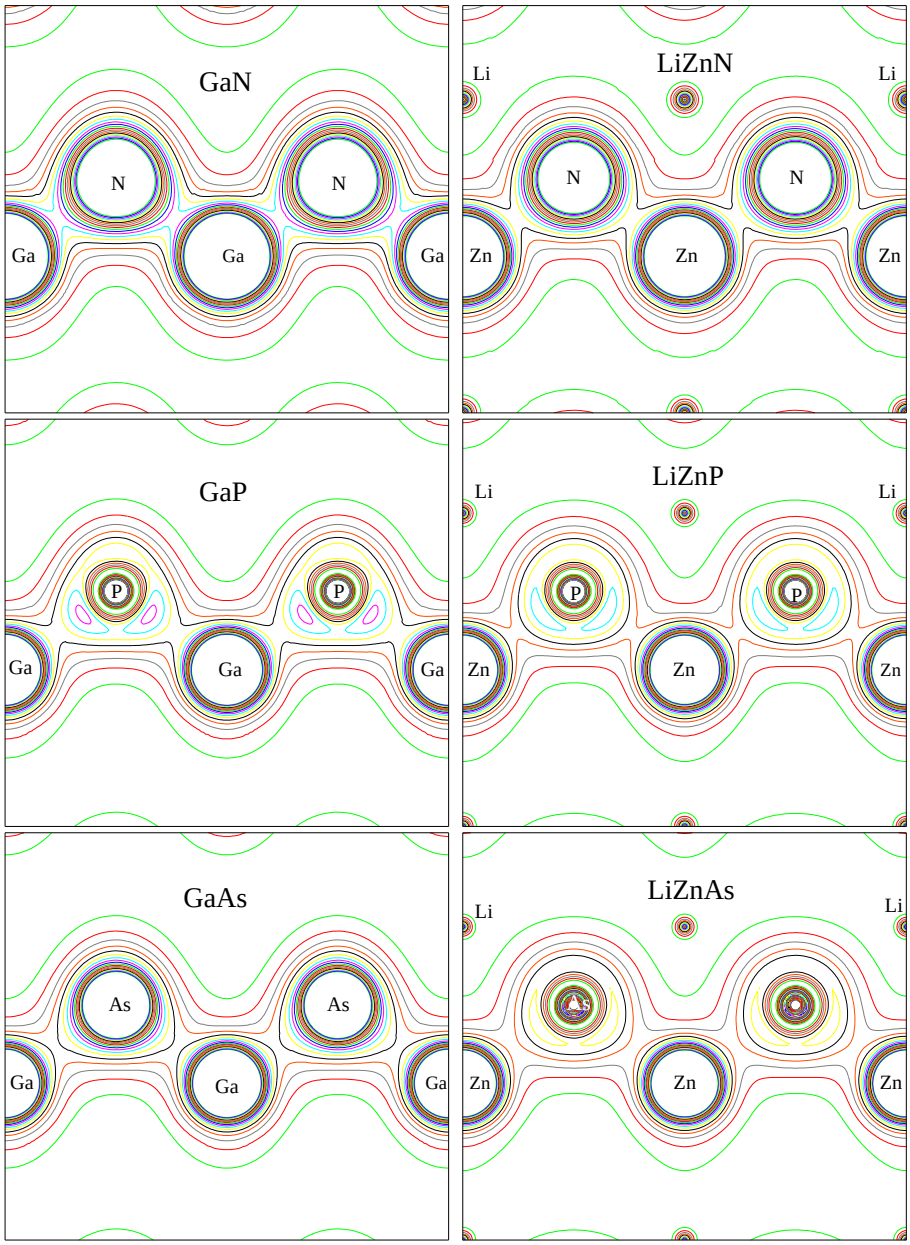

Figure 6.3: Valence charge density in plane (110)

density in the (110) plane and its profile along the bonding direction ⟨111⟩ for the studied compounds and also for the GaX compounds for comparison. The calculated densities show a great similarities between the ternary and binary compounds as it illustrated in figure 6.2 and 6.3 leading to similar character of the Zn–X and Ga–X bonds, and the main features of the bonding character are :

(i) The Li–N, Li–P and Li–As bonds, have a strongly ionic character with the presence of small amount of covalent charge.

(ii) The Zn–P, Zn–As are similar to Ga–P and Ga–As bonds, which are strongly covalent.

(iii) The Zn–N bond is similar to the Ga–N bond which have strong ionic character, with small covalent character indicated by the presence of small amount of valence charge along the bond.

(iv) The filling of the interstitial site $(\frac{1}{2}, \frac{1}{2}, \frac{1}{2})$ induce a small change in the shape of the electronic charge distribution of the anion atom and reduce its anisotropy, as it clear from the more spherical shape of the charge of N, P and As atom in the filled compounds in comparison with their shape in GaN, GaP and GaAs. This little difference of the sharge shape can be attributed to the volume change (dilation) and the charge transfer from the Li to the anion atoms.

In conclusion the valence charge densities confirm the previously deduced strong directional bonding between atoms (i.e., from the large elastic moduli) and the half–ionic half–covalent nature of the LiZnP and LiZnAs [5], and indicate that the LiZnN is ionic rather than covalent semiconductor.

6.5 Conclusion

We have performed first–principles calculations of structural and elastic properties of the Nowotny–Juza filled tetrahedral semiconductors LiZnX and the binary GaX (X=N, P, As) by using the FP–LAPW method, within the local density approximation. The energy minimization reveals that the most stable phase is the α one for all the studied compounds. The reliability of the predicted results for the FTC is checked by comparing the calculated results and the experimental data for the GaX compounds. The filling of the interstitial

sites leads to a reduction of the bulk modulus which is related to hardness. Our results show that the overall trend in the elastic constants of the LiZnX is similar to that in those of the binary compounds, where all the c_{ij} are reduced in moving downward in the periodic table of the elements, i.e., from N to As.

From the theoretically obtained elastic constants, the sound velocities are calculated and found to be in good agreement with the recent calculation of the vibrational spectrum of LiZnAs.

The calculated elastic constants are used to compute the elastic moduli of polycrystalline samples, which indicate a strong directional bonding between atoms. The charge density contours and profiles confirm the strong directional bonding, and show that the LiZnP and LiZnAs have a dual bonding character i.e., Half–covalent and Half–ionic semiconductors at the same time, whereas, LiZnN is ionic rather than covalent semiconductors like its parent GaN.

BIBLIOGRAPHY

[1] D. M. Wood, A. Zunger, and R. de Grood, Phys. Rev. B **31** (1985) 2570.

[2] A. E. Carlsson, A. Zunger, and D. M. Wood, Phys. Rev. B **32** (1985) 1386.

[3] R. Bacewicz and T. F. Ciszek, Appl. Phys. Lett. **52** (1988) 1150.

[4] H. W. M. Rompa, M. F. H. Schuurmans, and F. Williams, Phys. Rev. Lett. **52** (1984) 675.

[5] Su–Huai Wei and A. Zunger, Phys. Rev. Lett, **56** (1986) 528.

[6] Li Hui-Ping et al, Chinese. Phys. Lett. **20** (2003) 114.

[7] L.H. Yu, K.L. Yao, and Z.L. Liu , Physica B, **353** (2004) 278.

[8] L. H. Yu, K. L. Yao, and Z. L. Liu , Solid State Commun. **135** (2005) 124.

[9] D. M. Wood, W. H. Strohmayer, Phys. Rev. B **71** (2005) 193201.

[10] K. Kuriyama and F. Nakamura, Phys. Rev. B **36** (1987) 4439.

[11] K. Kuriyama and T. Katoh, Phys. Rev. B **37** (1988) 7140.

[12] K. Kuriyama, T. Katoh, and T. Tanaka, Phys. Rev. B, **49** (1994) 4511.

[13] K. Kuriyama, T. Kato, and K. Kawada, Phys. Rev. B, **49** (1994) 11452.

[14] K. Kuriyama, K. Kushida, and R. Taguchi, Solid State Commun. **108** (1998) 429.

[15] K. Kuriyama and K. Kushida, J. Appl. Phys, **87** (2000) 2303.

[16] K. Kuriyama and K. Kushida, J. Appl. Phys. **87** (2000) 3168.

[17] K. Kuriyama, K. Nagasawa, and K. Kushida, J. Cryst. Growth **237/239** (2002) 2019.

[18] K. Kushida, Y. Kaneko, and K. Kuriyama, Phys. Rev. B **70** (2004) 233303.

[19] M. J. Mehl, B. M. Klein and D. A. Papaconstantopoulos, Intermetallic Compounds: Principles and Practice, Volume I: Principles, J. H. Westbrook and R. L. Fleisher, eds., John Wiley and Sons (London, 1995) Ch. 9 (pp. 195–210).

[20] H. Neumann, Cryst. Res. Technol. **39** (2004) 939.

[21] P. Ravindran, L. Fast, P. A. Korzavyi and B. Johansson, J. Wills and O. Eriksson. J. Apll. Phys. **84**, 4891 (1998).

[22] D. Singh. *Planes waves, pseudo-potentiels and the LAPW method*. Kluwer Academic Publishers, Boston, Dortrecht, London, 1994.

[23] P. Blaha, K. Schwarz, G. K. H. Madsen, D. Kvasnicka and J. Luitz. *WIEN2k, An Augmented Plane Wave + Local Orbitals Program for Calculating Crystal Properties*. Karlheinz Schwarz, Techn. Universität Wien, Austria, 2001. ISBN 3-9501031-1-2.

[24] P. Hohenberg and W. Kohn, Phys. Rev. B, **136**, (1964) 864.

[25] W. Kohn and L. J. Sham, Phys. Rev. A, **140**, (1965) 1113.

[26] J. P. Perdew. and Y. Wang. *Phys. Rev.* ***B***, **45** (1992) 13244.

[27] F. D. Murnaghan. *Proc. Natl Acad. Sci, USA*, **30** (1944) 244.

[28] M. B. Kanoun, A. E. Merad, G. Merad, J. Cibert and H. Ourag, Solid–State Electronics, **48** (2004) 1601.

[29] O. H. Nielson and R. M. Martin, Phys. Rev. **B**, 32 (1985) 3792.

[30] K. Miwa and A. Fukumoto, Phys. Rev. **B**, 48 (1993) 7897.

[31] Kwiseon Kim, Walter R. L. Lambrecht, and Benjamin Segall, Phys. Rev. **B**, 50 (1994) 1502.

[32] A. F. Wright and J. S. Nelson, Phys. Rev. **B**, 51 (1995) 7866.

[33] A. Polian, M. Grimsditch and I. Grzegory, J. Apll. Phys. **79**, 3343 (1996).

[34] Kwiseon Kim, Walter R. L. Lambrecht, and Benjamin Segall, Phys. Rev. **B**, 53 (1996) 16310.

[35] A. F. Wright, J. Apll. Phys. **82**, 2833 (1997).

[36] Richard M. Martin, Phys. Rev. **B**, 6 (1972) 4546.

[37] Peter Y. Yu and Manual Cardona. *Fundamentals of Semiconductors*. Third edition, Springer, 2001.

[38] C. G. Van de Walle, Phys. Rev. **B**, 39 (1989) 1871.

[39] B. B. Karki, G. J. Ackland and J. Crain, J. Phys.: Condens. Matter, **9** (1997) 8579.

[40] C. Kittel. *Introduction to solid state physics*. Fourth edition, John Willey & Sons. New York, 1971.

CHAPTER 7

Optical properties of the filled tetrahedral semiconductors LiZnX (X=N,P, and As)

7.1 Introduction

Nowotny-Juza LiZnX (X=N,P, and As) semiconductors belong to the class of filled tetrahedral compounds (FTC) $A^{I}B^{II}C^{V}$ recognized as very promising materials for technological applications. They have been first synthesized and structurally characterized in the middle of the last century (1940–1950) by Nowotny [1] and Juza [2]. Their crystal structure can be derived from the zinc blend III–V compounds structure by transmuting the group III atom into its isovalent pair A^{I}+B^{II}, in this context the $B^{II}C^{V}$ form zinc blend lattice and the A^{I} atom can occupy either the $a(\frac{1}{2},\frac{1}{2},\frac{1}{2})$ site (where a is the lattice parameter) and forms the α phase, or the $a(\frac{3}{4},\frac{3}{4},\frac{3}{4})$ site which is the β phase.

Interest in this compound family was renewed since the predictions of Wood et al. [3] and Carlson et al. [4] that LiZnP and LiZnN exhibit semiconducting behavior with direct–wide energy gap. Their predictions have stimulated many other works, and were confirmed experimentally by Kuriyama and his group [5–7] and R. Bacewicz and T.F. Ciszek [8].
The electronic band structure was calculated and interpreted by means of the

insertion rule [4], and the structural aspect and bonding character have been the subject of many studies [9–12]. Recently, Wood and Strohmayer [13] have studied the vibrational properties of LiZnAs and LiZnP, and more recently the elastic properties were reported by us [14]. Unfortunately, there are only few data concerning the optical constants of this interesting semiconductors family, yet up to now there is no theoretical work concerning the linear optical properties of these FTC, although their promising potential technological applications have been emphasized.

In this chapter, we present studies of the linear optical properties of α–LiZnX compounds. The trend in the bandgap is discussed and analysed in terms of covalency and anion p–cation d repulsion effects. The features of obtained optical spectra are assigned to interband transitions along the Brillouin zone high symmetry lines. The rest of this paper is organized as follows; in section 7.2 we briefly discuss the electronic properties of LiZnX; in section 7.3 the trend in the bandgap is analysed ; in section 7.4 we describe the method used for the calculations of optical properties and we give the obtained results. A conclusion is given in section 7.5.

7.2 Band structure and density of states

Since the optical properties are closely related to the electronic structure, it is of interest to describe it first and then we use it in analyzing the different optical spectra features. As in the previous chapter [14], we use the FP–LAPW method with the Perdew–Wang exchange–correlation term [17] and the same calculation details. The electronic band structures, density of states and optical spectra are calculated at the theoretical lattice parameters, which are 4.80 Å, 5.61 Å and 5.80 Å for LiZnN, LiZnP and LiZnAs, respectively.

Figure 7.1 illustrates our calculated band structures (left panels) and the

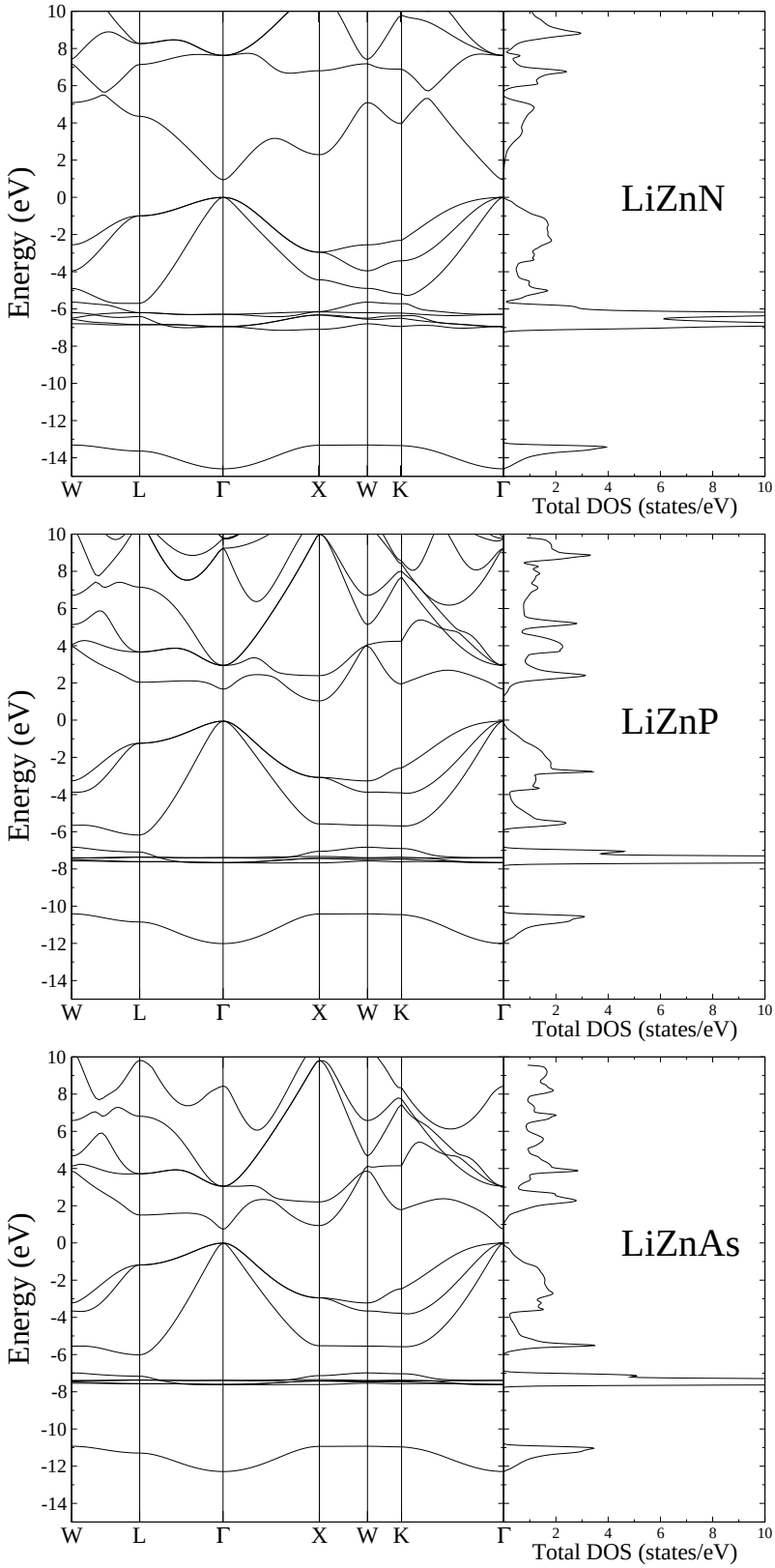

Figure 7.1: Electronic band structure (left panels) and total density of states (right panels) for the ternary compounds LiZnN, LiZnP and LiZnAs, the Fermi level is set to zero.

corresponding total density of states (DOS) (right panels) for the three studied compounds, while figures 7.2–7.4 show the site and angular momentum decomposed DOS. It is clear from these figures that the studied compounds are semiconductors and their band structures show great overall similarities to those of III–V [18–23] and IIB–VI [24–26] compounds. In the III–V binary analogous compounds the d bands are deeper in energy compared to those in the ternary ones LiZnX, this makes the p–d interaction stronger in the latter ones [26, 27]. This p–d coupling, which is included in our calculations, affects the electronic and structural properties of Nowotny–Juza compounds by decreasing the gap and lattice parameter. For example, whereas the Zn atom possesses an additional electronic shell than the Mg atom, the lattice parameter of LiZnN (4.91 Å [6]) is smaller than that of LiMgN (4.95 Å [28]), and its bandgap is also smaller 1.91 eV [6] for LiZnN and 3.2 eV [28] for LiMgN.

The calculated band structure and DOS show similarities for the studied ternary compounds. The first peak reflects the group V atom s states, which corresponds to the low lying band in figure 7.1, and its width originates mainly from the region around the Γ point in BZ, since only there the dispersion of the band is appreciable. The second one, a narrow Zn d states which lie higher in energy for LiZnN than for LiZnP and LiZnAs (see figures 7.1–7.4), this peak is broader (i.e., not core like states) in LiZnN than in the other two compounds. It also contains a small contributions from the V atoms p states and which decreases in this sequence LiZnN–LiZnP–LiZnAs. The rest of the valence and conduction bands are mixture of p and s states with small amount of d states. The contribution of d states to the valence band maximum (VBM) is larger in LiZnN than the others.

Our calculation indicates that the valence band maximum is at Γ point and the minimum of the conduction band is also at Γ for LiZnN and LiZnAs, while it is at the X point for LiZnP. The bandgap nature of LiZnP is not consistent with the experimental finding. It is worth noting that L.H. Yu et al. [12], found

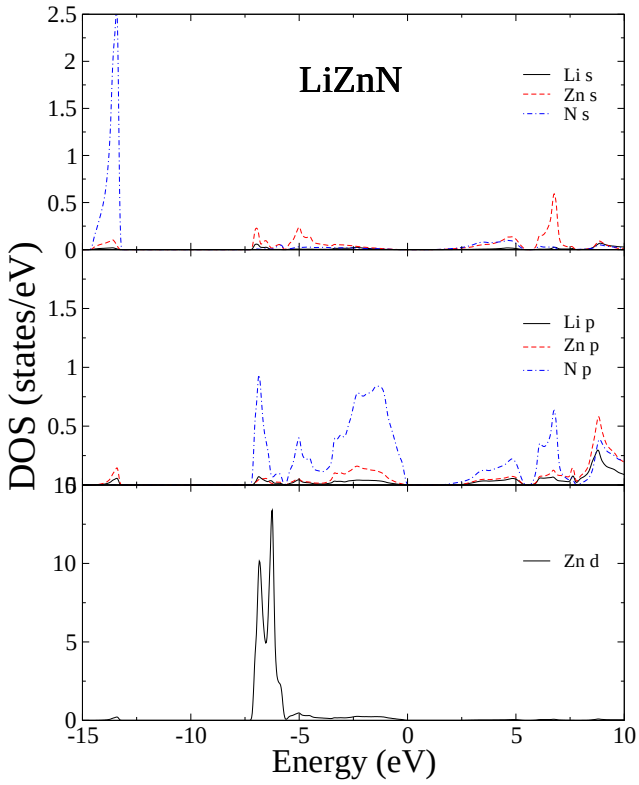

Figure 7.2: Site and angular momentum decomposed DOS of LiZnN, the Fermi level is set to zero.

the same inconsistency for LiMgP and they suggest that more experimental measurements are necessary. In table 7.1, we report our calculated bandgaps together with the experimental and other theoretical results. The theoretical gaps are smaller than the experimental values, this discrepancy is attributed to the LDA method which always underestimates the bandgap. Our calculated bandgaps for the ternaries have similar trend as the measured ones, however, both of them do not follow the usual trend encountered in the GaX binaries, i.e., as the ionicity increases the bandgap increases in the series GaAs–GaP–GaN. It is worth noting that the bandgaps of LiMgX compounds have similar trend as AlX compounds [28]. Therefore, the small bandgap of LiZnN deserves further attention and its origin will be discussed in the next section.

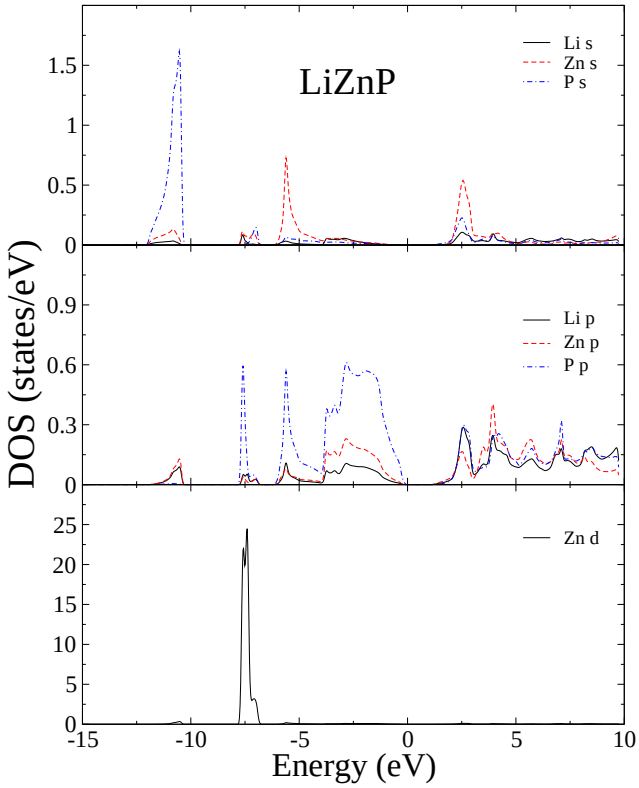

Figure 7.3: As figure 7.2, but for LiZnP.

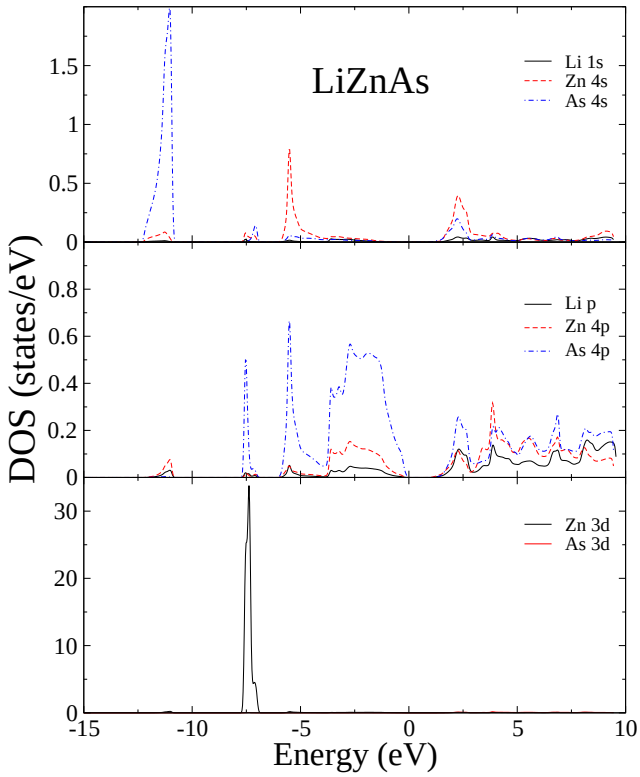

Figure 7.4: As figure 7.2, but for LiZnAs.

Table 7.1: Calculated and experimental bandgaps (eV) for LiZnN, LiZnP and LiZnAs.

	Direct gap ($\Gamma - \Gamma$)		Indirect gap ($\Gamma - X$)		Expt.
	This work	Other	This work	Other	
LiZnN	0.94	0.601 [11]	2.29	2.34 [11]	1.91 [6]
$(ZnN)^-$	0.35		2.84		
GaN[1]	0.55		3.19		
GaN	1.94		3.26		3.2–3.5[4]
LiZnP	1.72		1.09		2.1 [8], 2.04 [5]
$(ZnP)^-$	1.48		1.36		
GaP[2]	1.23		1.65		
GaP	2.10		1.45		2.338–2.35[4]
LiZnAs	0.74		0.94		1.25 [8], 1.51 [7]
$(ZnAs)^-$	0.48		1.23		
GaAs[2]	0.34		1.52		
GaAs	1.11		1.35		1.51[4]

[1] At the lattice parameter of LiZnN.
[2] At the lattice parameter of LiZnP.
[3] At the lattice parameter of LiZnAs.
[4] See Ref. [29] and references therein.

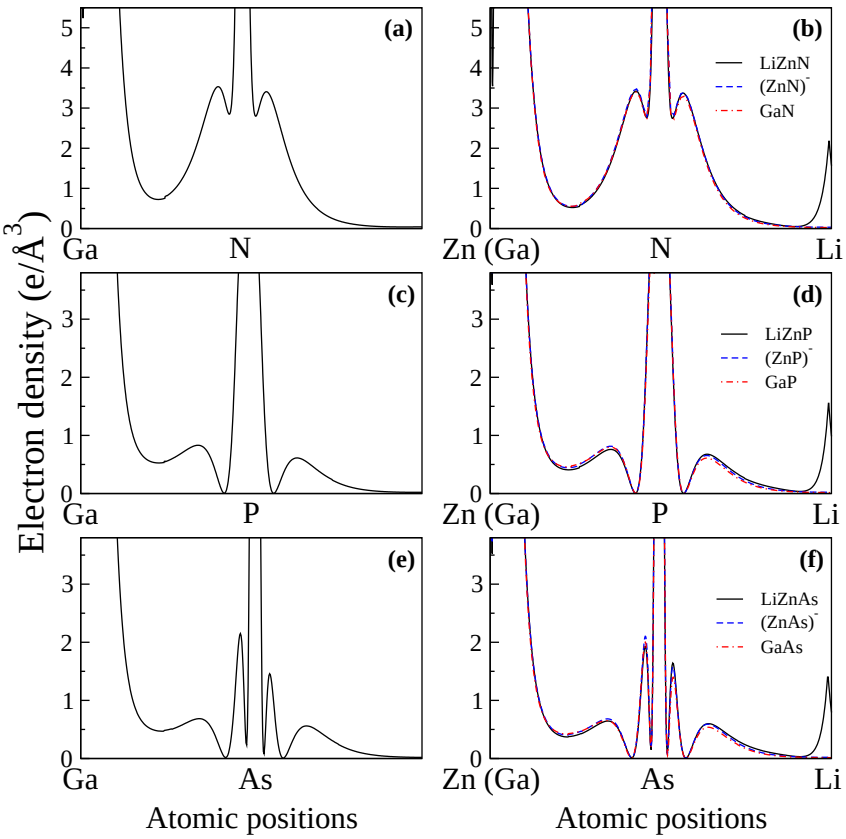

Figure 7.5: Charge density profile along the ⟨111⟩ direction for GaN (a); GaN, LiZnN and $(ZnN)^-$ at a=4.80 Å (b), GaP (c); GaP, LiZnP and $(ZnP)^-$ at a=5.61 Å (d); GaAs (e); GaAs, LiZnAs and $(ZnAs)^-$ at a=5.80 Å (f).

Table 7.2: Calculated p–d repulsion energy (eV) for LiZnN, LiZnP and LiZnAs using model A1 and A2 of Ref. [26]. Q_d is the fraction of d character in the Zn sphere, V_{pd} is the p–d coupling matrix element, and ΔE_{pd} is the energy shift of the valence band maximum due to p–d repulsion.

	Q_d		$\Gamma_{15v} - \Gamma_{15d}$		V_{pd}		ΔE_{pd}	
	A1	A2	A1	A2	A1	A2	A1	A2
LiZnN	0.163	0.120	6.96	6.96	1.13	0.84	2.57	2.27
LiZnP	0.100	0.065	7.60	7.60	0.76	0.49	2.27	1.87
LiZnAs	0.079	0.051	7.60	7.60	0.60	0.39	2.05	1.67

7.3 Trend in bandgaps

As one goes from the binary zinc blende GaX to their filled compounds LiZnX, many effects can alter their electronic properties. In particular the bandgap is related to volume, bonding character and charge density maps at high symmetry points in the BZ. Moreover, for a system containing active d orbital like 3d of Zn atom, the anion p–cation d coupling (repulsion) leads to an upward shift of the VBM. To systematically study these effects we proceed as follows; (i) we assume that the filled compounds can be obtained from their binary parents by, first, increasing the volume of the binary compound, second, replacing the Ga atom by Zn and form the hypothetical $(ZnX)^-$, finally, inserting the $(Li)^+$ ion at the interstitial site and form the filled compound LiZnX; (ii) from the examination of the bandgap and charge density evolutions in all these structures, firstly we can be able to explain the small gap of the FTC in comparison with their parents, and secondly to gain more insight on the puzzling small bandgap of LiZnN in comparison with LiZnP. The charge density profiles are plotted in figure 7.5, and the bandgaps are listed in table 7.1.

From the charge density plots, it is clearly seen that the charge densities are quite similar for the ternary and binary compounds, which qualitatively lead to the same trend in the bonding character of Ga–X and Zn–X bonds, whereas, the X–Li bonds are purely ionic. Furthermore, the heteropolar gaps L_{1v}–L_{1v} and X_{1v}–X_{3v} (the labels of the bands are the same as those of Ref. [9]) are much greater in LiZnN than in LiZnP (see figure 7.1) showing that the polarity is greater in the former than in the later. From this point of view it is expected that the bandgaps in the ternary compounds follow the same trend as in the binaries (i.e.; increase in the series LiZnAs–LiZnP–LiZnN) as suggested by Kuriyama before measuring the bandgap of LiZnN [5].

From table 7.1, the direct bandgap of the binary decreases as the volume increases. Furthermore, the insertion of the Lithium atom increases the gap, this is consistent with the result of [Ref. [4] Fig.2]. The only anomaly is found

when going from GaX (at the same volume of the ternaries) to the hypothetical $(ZnX)^-$, whereas, the gap increases for the arsenide and phosphide compounds, it decreases for the nitride one. As in the case of ZnO, despite its greater ionicity it has smaller bandgap than ZnS [26, 30], the p–d coupling might be responsible of the small gap value of LiZnN. This effect has been confirmed experimentally to exist in LiZnAs and LiZnP by Nelson et al. [27]. In fact, from Fig. 6 of Ref. [26], the orbital energy of Zn 3d is closer to the one of N 2p than to the ones of P 3p and As 4p, therefore one expect the p–d repulsion to be stronger in LiZnN than LiZnP and LiZnAs.

In order to assess for the p–d coupling, we used the tight–binding model given in appendix of Ref. [26] for estimating the energy shift of the valence band maximum for two different band parameters obtained from our calculated band structures. The results are given in table 7.2, which show clearly that the p–d repulsion in LiZnN is stronger than the other compounds, which shifts the VBM upward in energy. This might be the reason why the bandgap of LiZnN is lower than those of LiZnP and LiZnAs.

In conclusion, the lower bandgaps of the filled compounds LiZnX in comparison with their parents is caused by the volume increase in these compounds and p–d coupling between the cation d and anion p orbital. Furthermore, the small bandgap of LiZnN is mainly due to the strong p–d coupling in this compound.

7.4 Optical properties

The linear optical properties in solids can be described with the complex dielectric function $\varepsilon(\omega) = \varepsilon_1(\omega) + i\varepsilon_2(\omega)$, the interband contribution to the imaginary part of $\varepsilon(\omega)$ is calculated as described in chapter 3. The calculated optical spectra depend strongly on the BZ sampling, therefore a sufficiently dense k–mesh is used in the calculations of optical spectra, which consists of $25 \times 25 \times 25$ k–mesh.

The calculated imaginary parts of the dielectric function for the three ternary compounds are displayed in figures 7.6–7.8. Like band structures and density of states, the optical spectra have similarities to those of the III–V binary analogous ones.

To analyze the calculated optical spectra and to determine the origins of the different peaks and features, we decompose each spectrum to its individual pair contribution, i.e., contribution from each pair of valence vi and conduction cj bands (vi–cj) (see figure 7.6). This technique together with the transition band structure (band pair, valence–conduction, energy differences in the BZ) allow the knowledge of the bands which contribute more to the peaks and their locations in the Brillouin zone [19, 32–34]. Figures 7.6–7.8 illustrate the electronic transitions band structures of the three studied compounds (given in the right panels). In tables 7.3–7.5 the calculated energy of the peaks as well as extended regions giving the dominant contributions to elements of the structure in the optical spectra are given. To the best of the author's knowledge no experimental spectra are available for these compounds. The details of the optical spectra are given below.

LiZnN

The spectra of LiZnN is quite different from the two others, it is too broad and contains more structure than those of LiZnP and LiZnAs. The threshold in ε_2 at 0.94 eV is caused by v1→c1 transition at Γ, the counting of the bands is down (up) from the top (bottom) of the valence (conduction) band. The rise and shoulder in 1–4 eV region involves the v1,v2,v3→c1 transitions along Λ, Δ and Σ lines. The rest of ε_2 spectra can be divided into three groups of structures. In the first group in the energy range 4.5–7.0 eV, there are two peaks, the first is mainly due to transition from the two highest valence bands to the lowest conduction band i.e., v1,v2→c1 in the W–L (Q line) and L–Γ

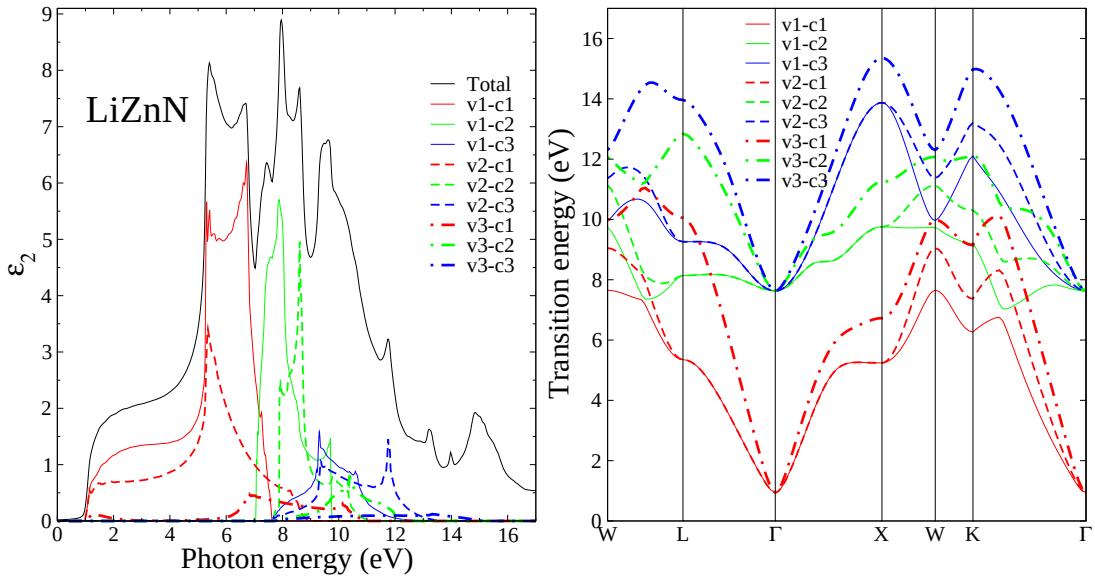

Figure 7.6: The decomposition of the imaginary part of the dielectric function into band–to–band contributions (left panel) and the transition energy band structure (right panel) for LiZnN. For the counting of the bands see text.

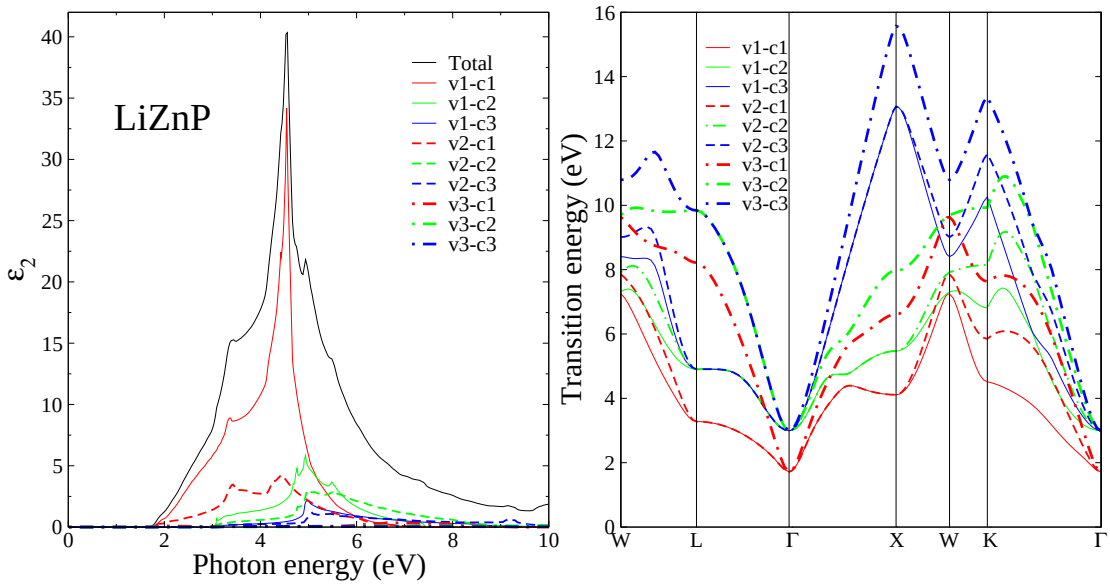

Figure 7.7: As figure 7.6, but for LiZnP.

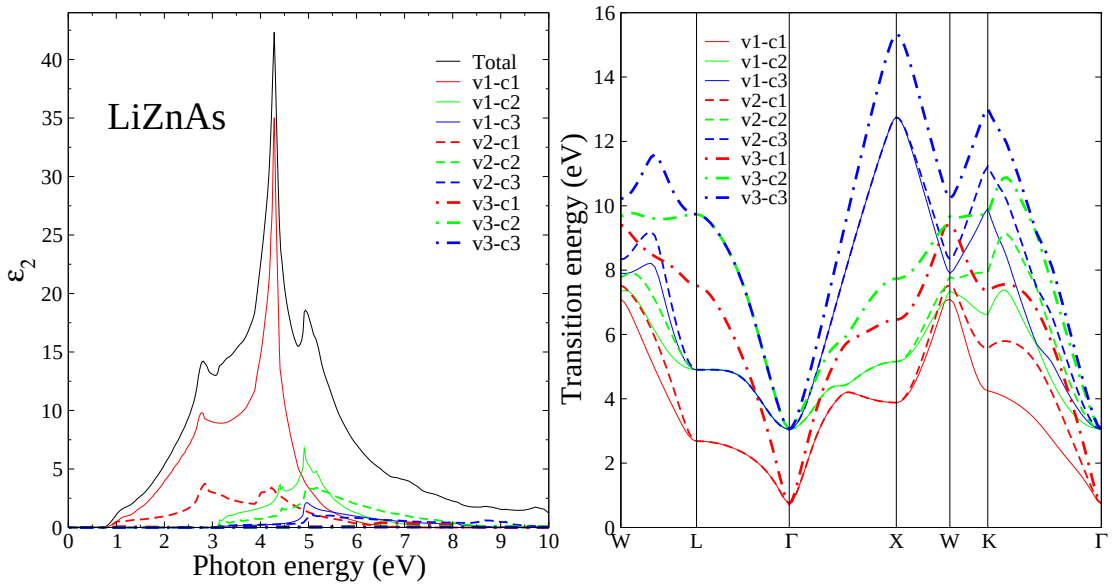

Figure 7.8: As figure 7.6, but for LiZnAs.

Table 7.3: Optical transitions in α–LiZnN.

Energy of optical structure	Major contribution transitions	
Peak position (eV)	Transition	Energy (eV)
5.30	Δ , X: v1→c1	5.30
	L, Q, Λ, X–W, Σ : v1→c1 ; v2→c1	5.35 ; 5.41
6.71	Q, Σ : v1→c1	6.72
	X, Δ : v3→c1	6.72
7.44	Q, Σ : v1→c2	7.44
7.96	Q, Λ, Δ, Σ : v1;v2→c2	7.88 ; 7.93
8.61	Q, Δ, Σ : v2→c2	8.61
9.48	Q (near L), Δ, Σ: v1→c3	9.30, 9.48
9.64	(near X); W–K: v1→c2	9.72; 9.70
	Σ : v2→c2	9.78
10.08	Q (Near L), Σ: v3→c1	10.08
10.58	Q, X–W–K,Σ: v1→c3	10.58
	Δ, Λ, Σ: v3→c2	10.39
11.75	Q, Δ, X–W, Σ: v2→c3, v3→c2	11.75
13.21	Q, Λ,Δ, W–K, Σ: v3→c3	13.21

(Λ line) directions in the vicinity of L, and in the Γ–X (Δ line). The second peak results from the K–Γ (Σ line). The second group in the 7.0–9.0 eV region consists of three peaks. The first two originate from v1→c2 transition in the

Q, Σ and Λ lines. The last one is arising mainly from v2→c2 transition in the Δ and Σ directions. There is also a significant contribution from the last transition to the second peak in Λ direction where the two bands are parallel (see figure 7.1). The last structure in the energy range 9–16 eV comes from the three highest valence bands to the third conduction band transitions. The positions of the peaks and the major contribution transitions are collected in table 7.3.

Table 7.4: Optical transitions in α–LiZnP.

Energy of optical structure	Major contribution transitions	
Peak position (eV)	transition	Energy (eV)
3.41	Q, Δ, Σ: v1→c1	3.36
	Q, Δ, Σ: v2→c1	3.42
4.55	Q, Σ: v1→c1	4.54
	Q, Δ, Σ: v1,v2→c1	4.40
4.79	Δ, Λ, Σ: v1→c2 ; v2→c2	4.76 ; 4.79
4.93	near L: v1→c2	4.93
	Q, Δ, Σ: v2→c2, v1→c3	4.98
	Q, Δ, Σ: v2→c3	5.07
5.5	X–W, Q, Σ: v1→c2	5.48
	X–W, Q, Σ: v2→c2	5.53

Table 7.5: Optical transitions in α–LiZnAs.

Energy of optical structure	Major contribution transitions	
Peak position (eV)	transition	Energy (eV)
2.77	Q, L : v1→c1	2.68
	Q, L : v2→c1	2.84
4.28	Δ, W–K : v1→c1	4.28
	Σ: v2→c1	4.28
	X : v1,v2→c1	3.94
	K : v2→c1	4.16
4.91	L, Δ, Λ : v1→c2	4.91
	Σ, Δ : v2→c2	5.00
5.15	X : v1→c2	5.15

LiZnP and LiZnAs

The imaginary parts of the dielectric function of LiZnP and LiZnAs are quite similar. From figures (7.7 and 7.8) it is clear that the most important contributions to the peaks in the optical spectra are due to the interband transitions from the highest valence band to the lowest conduction band. There is also a significant contribution from v2→c1 and v1→c2. Table 7.4 and 7.5 indicate the contributing regions and directions in the BZ to the spectra of LiZnP and LiZnAs, respectively. The first peak originates from the Λ direction and the neighborhood of L in the Q line. The main peak is arising from the Δ line and the neighborhood of K. The third peak comes from the Q, Λ and Δ lines and it is worth noting that the contribution from v1→c2 to this peak is somewhat higher in LiZnAs than in LiZnP. At higher energies the spectra decay rapidly with photon energies.

Table 7.6: The calculated dielectric constants of α–LiZnX and their binary analogous GaX, together with the available experimental and other calculation results.

Materials	Uncorrected	Corrected	Other	Expt.	ΔE (eV)
LiZnN	6.58	5.61			0.97
GaN	5.59	4.79	4.78 [33]	5.2, 5.7[1]	1.41
LiZnP	10.53	9.85		9.6[2] [10]	0.32
GaP	11.05	9.14	9.1–9.59 [35][3]	9.1 [35][3]	1.00
LiZnAs	12.56	10.44	11.1 [13]		0.76
GaAs	13.98	10.88	10.2–13.1 [35][3]	10.8–10.9 [35][3]	1.02

[1] Wurtzite values taken from Ref. [33], [2] Ref. [10] (Estimated value),
[3] See Ref. [35] and references therein.

The real parts of the dielectric function were also calculated from the imaginary parts using the Kramers–Kronig relation, but they are not shown here. We just give the static dielectric constants $\varepsilon(0)$. However, the dielectric constant is overestimated by the LDA, which is often attributed to the underestimation of the bandgap by this approximation [35, 36]. In order to correct for this LDA effect, a constant energy shift is applied to the conduction bands so

as to match the calculated bandgaps with the experimental data. The theoretical values of the static dielectric constant $\varepsilon(0)$ (with and without shift) of the studied compounds, together with the theoretical and experimental ones of the binary parents GaX are summarized in table 7.6. The last column contains the values of the energy shift. For the binaries, the corrected values of $\varepsilon(0)$ are in good agreement with the experimental ones. This might be an estimate of the reliability of the predicted values for the ternaries.

7.5 Conclusion

In conclusion, we have presented first principles study of the electronic properties and optical spectra of the three filled tetrahedral compounds LiZnN, LiZnP and LiZnAs. In our calculations the FP–LAPW in the LDA scheme has been used. The bandgap trend is analysed in terms of bond covalency and anion p–cation d coupling effect. The small value of LiZnN gap is attributed to the later. The calculated optical spectra are quite similar for LiZnP and LiZnAs. The decomposition of the dielectric functions into individual band–to–band contributions and the transition band structures allowed to identify the microscopic origin of the features in the optical spectra and the contributions of the different regions in the Brillouin zone. The calculated static dielectric constants of the ternaries obtained by correcting the calculated bandgaps, overestimated by the LDA, with the scissor operator predict that they are close to the binary ones for LiZnP and LiZnAs.

BIBLIOGRAPHY

[1] H. Nowotny, K. Bachmayer, Mh. Chem. 80 (1949) 734.

[2] R. Juza, F. Hund, Z. Anorg. Chem. 257 (1948) 1.

[3] D.M. Wood, A. Zunger, R. de Groot, Phys. Rev. B **31** (1985) 2570.

[4] A.E. Carlsson, A. Zunger, D. M. Wood, Phys. Rev. B **32** (1985) 1386.

[5] K. Kuriyama, T. Kato, Phys. Rev. B **37** (1988) 7140.

[6] K. Kuriyama, T. Kato, T. Tanaka, Phys. Rev. B **49** (1994) 4511.

[7] K. Kuriyama, T. Kato, T. Tanaka, Phys. Rev. B **49** (1994) 11452.

[8] R. Bacewicz, T.F. Ciszek, Appl. Phys. Lett. **52** (1988) 1150.

[9] Su–Huai Wei, A. Zunger, Phys. Rev. Lett. **56** (1986) 528.

[10] K. Kuriyama, Y. Takahashi, K. Tomizawa, Phys. Rev. B **47** (1993) 13861.

[11] L.H. Yu, K.L. Yao, Z.L. Liu, Physica B **353** (2004) 278.

[12] L.H. Yu, K.L. Yao, Z.L. Liu, Solid State Commun. **135** (2005) 124.

[13] D.M. Wood, and W.H. Strohmayer, Phys. Rev. B **71** (2005) 193201.

[14] F. Kalarasse, B. Bennecer, J. Phys. Chem. Solids **67** (2006) 846.

[15] D. Singh. *Planes waves, pseudo-potentials and the LAPW method*. Kluwer Academic Publishers, Boston, Dortrecht, London, 1994.

[16] P. Blaha, K. Schwarz, G.K.H. Madsen, D. Kvasnicka, J. Luitz. *WIEN2k, An Augmented Plane Wave + Local Orbitals Program for Calculating Crystal Properties*. Karlheinz Schwarz, Techn. Universität Wien, Austria, 2001. ISBN 3-9501031-1-2.

[17] J.P. Perdew, Y. Wang. Phys. Rev. **B** 45 (1992) 13244.

[18] J.P. Walter, M.L. Cohen, Phys. Rev. **183** (1969) 763.

[19] M. Alouani, L. Brey, N.E. Christensen, Phys. Rev. B **37** (1988) 1167.

[20] C. Persson, A. Zunger, Phys. Rev. B **68** (2003) 073205.

[21] K. Miwa, A. Fukumoto, Phys. Rev. B **48** (1993) 7897.

[22] K. Kim, W.R.L. Lambrecht, B. Segall, Phys. Rev. B **50** (1994) 1502.

[23] N.E. Christensen, Phys. Rev. B **30** (1984) 5753.

[24] J.P. Walter, M.L. Cohen, Phys. Rev. B **1** (1970) 2661.

[25] N.E. Christensen, O.B. Christensen, Phys. Rev. B **33** (1986) 4739.

[26] Su–Huai Wei, A. Zunger, Phys. Rev. B, **37** (1988) 8958.

[27] A.J. Nelson, M. Engelhardt, H. Hochst, Journal of Electron Spectroscopy and Related Phenomena **51** (1990) 623

[28] K. Kuriyama, K. Nagasawa, K. Kushida, J. Cryst. Growth **237/239** (2002) 2019.

[29] I. Vurgaftman, J.R. Meyer, L.R. Ram–Mohan, J. Appl. Phys. **89** (2001) 5815.

[30] M. Oshikiri, F. Aryasetiawan, Phys. Rev. B **60** (1999) 10754.

[31] C. Ambrosch-Draxl, J.O. Sofo. *Linear optical properties of solids within the full-potential linearized augmented plane wave method.* preprint, arXiv: cond–mat/0402523, Feb 2004.

[32] I. Gorezyca, N.E. Christensen, M. Alouani, Phys. Rev. B **39** (1989) 7705.

[33] N.E. Christensen, I. Gorezyca, Phys. Rev. B **50** (1994) 4397.

[34] W.R.L. Lambrecht, S.N. Rashkeev, Phys. Stat. Sol. (**b**) 217 (2000) 599.

[35] F. Kootstra, P.L. de Boeij, J.G. Snijders, Phys. Rev. B **62** (2000) 7071.

[36] C. Persson, R. Ahuja, A. Ferreira da Silva, B. Johansson, J. Phys.: Condens. Matter 13 (2001) 8945.

CHAPTER 8

Electronic structure of the filled tetrahedral compound LiCdP and zinc–blende InP: application of the insertion rule

8.1 Introduction

Among the Nowotny–Juza filled tetrahedral compounds [1, 2], the LiZnX and LiMgX (where X=N, P, As) are the most studied both experimentally [3–7] and theoretically [8–21]. Unfortunately, there are only few works concerning the electronic properties of the Cadmium based compounds of this family (i.e., LiCdX). The bandgap of LiCdP has been roughly estimated by Bacewicz and Cizeck [22], they reported that they can not determine its nature (direct or indirect). On the theoretical side, to our knowledge, there have been two previous calculations of LiCdP electronic structure using the linear muffin tin orbital method (LMTO). The first one by Pawlowska et al. [23] only displays the band structure, the second one by Kandepal et al. [15] reports some electronic properties of LiCdP. Very recently Mellouki et al. [24] have reported the elastic properties and deduced the sound velocities in different directions of this compound.

However, since LiCdX compounds are analogous to the zinc–blende InX ones, which crystallize in the same space group, it is expected that their properties

are quite similar to them. Moreover, it has been argued by Richardson and Cohen [25] that the filled compounds derived from InP, InAs and InSb are expected to have larger bandgaps than their parents. Their suggestions were based on the analysis of valence charge densities at high symmetry points of the Brillouin zone (BZ) in conjunction with the insertion rule [9]. Thus a detailed investigation of the electronic structure of LiCdX (X=P, As and Sb) is of great interest.

The aim of this chapter is to give a detailed study of the electronic properties of the filled compound LiCdP. To give more insight on the filling induced change in the electronic band structure we also calculate the electronic properties of the binary analogous compound InP. This chapter is organized as follows; in section 8.2 we describe the crystal structure and we give the calculation details; section 8.3 encloses the obtained results and their discussions; finally a summary is given in section 8.4.

8.2 Structural aspects and computational details

The crystal structure of Nowotny–Juza filled compounds, as illustrated in figure 8.1, is closely related to the zinc–blende structure. The zinc–blende structure can be characterized as an "empty tetrahedral interstitial structure", with the cation atom at $\tau_1(0,0,0)a$ and the anion at $\tau_2(\frac{1}{4},\frac{1}{4},\frac{1}{4})a$, and two vacant interstitial sites at $\tau_3(\frac{1}{2},\frac{1}{2},\frac{1}{2})a$ and $\tau_4(\frac{3}{4},\frac{3}{4},\frac{3}{4})a$, where a denotes the lattice parameter. The filled compounds $A^IB^{II}C^V$ can be obtained from their binary analogous ones ($D^{III}C^V$) by transmuting the cation atom (group D^{III} atom) to its isovalent pair B^{II}+A^I (e.g., In to Cd+Li), the B^{II} and C^V atoms form a regular zinc–blende crystal, and the A^I atom can occupy either the τ_3 site and forms the α phase or the τ_4 site which is the β one. When the two sites are occupied we obtain the γ phase.

The present calculations are performed using the full potential linear aug-

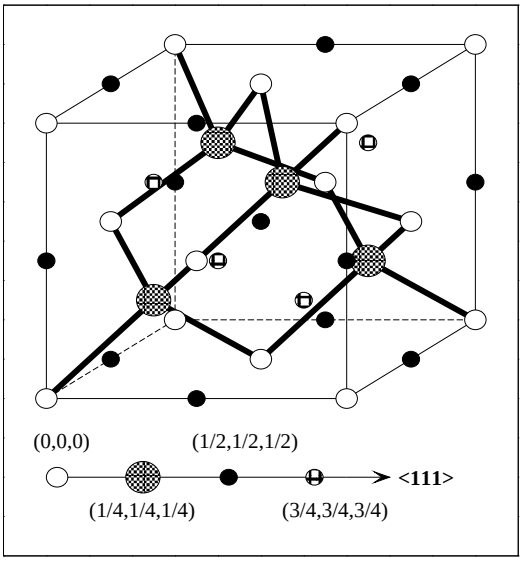

Figure 8.1: Crystal structure of the Nowotny–Juza filled tetrahedral compounds. The occupation of the sites by the atoms is explained in the text.

mented plane wave method within the local density approximation (LDA), as implemented in the Wien2k code [27].

In this work we treat the core electrons fully relativistically, and the valence electron scalar relativistically (all the relativistic effect are taken into account except the spin orbit coupling). In the calculations, the In ($4d^{10}5s^25p^1$), Li ($2s^1$), Cd ($4d^{10}5s^2$) and P ($3s^23p^3$) states are treated as valence electrons, and the muffin–tin radii are chosen to be 2.2 Bohr for all atoms of InP and LiCdP. The basis functions are expanded up to $R_{mt} \times K_{max} = 8$ (where K_{max} is the plane wave cut–off and R_{mt} the smallest of all MT sphere radii), and up to $l_{max} = 10$ in the expansion of the non spherical charge and potential. We use the Perdew and Wang functional [30] for the exchange and correlation interaction. For the integration we used $8 \times 8 \times 8$ k–points mesh in the whole first Brillouin zone and the self consistent calculations are considered to be converged when the total energy is stable within 0.1 mRyd.

8.3 Results

8.3.1 Structural properties

The ground state structural parameters are determined by calculating the total energy for a set of unit cell volumes and fitting them to the Murnaghan's equation of state [31]. The fitted curves were reported in Ref. [24].
The obtained lattice parameter, bulk modulus and its first order pressure derivative are listed in table 8.1 along with available experimental data and results of other calculations. The calculated lattice parameters, even underestimated by the LDA, agree well with the experimental ones. However, our result for InP bulk modulus is in good agreement with the measured value. The total energy calculations show that the α phase of LiCdP is more stable than the β one.

Table 8.1: Structural parameters, lattice parameter a_0 in (Å), Bulk modulus B in (GPa) and its pressure derivative B' for α–LiCdP, β–LiCdP and zinc–blende InP.

	α–LiCdP	β–LiCdP	InP
a_0	5.98[1], 6.11[2], 6.087[2], 6.096[3]	5.99[1]	5.84[1], 5.869[4], 5.87[5]
B	66.22[1], 52.80[2]	65.31[1]	70.79[1], 71.10[5]
B'	4.44[1]	4.59[1]	4.29[1]

[1]This work,
[2]Ref. [15],
[3]Ref. [22],
[4]Ref. [32],
[5]Ref. [33].

8.3.2 Band structure

Figure 8.2 shows the electronic band structures of the α and β–LiCdP compared to the zinc–blende InP one. From this figure it is clear that LiCdP and InP are semiconductors with direct gap at the Brillouin zone center (Γ point). The different bandgaps are summarized in table 8.2. The conduction band valleys follow the Γ–L–X ordering of increasing energy for β–LiCdP and InP, and

the Γ–X–L one for α–LiCdP. The insertion of Li^+ ions at the interstitial sites pushes the energy levels of the second valence bands upwards and reduces their width in the two phases of LiCdP compared to InP. The most striking features of the bandgaps is that the direct bandgap of α–LiCdP is wider than that of InP. The situation is reversed for the indirect gap Γ–X. The wider direct and smaller indirect bandgaps of the ternary compound α–LiCdP in comparison with its binary analogous InP is in good agreement with the previous report of Richardson and Cohen [25], and can be understood through the '*interstitial insertion rule*' [9] which states that: "*substitution of the tetrahedral interstitial sites in zinc–blende semiconductor by He– or Li^+–like species (i.e., repulsive s core potentials, attractive non–s core potentials) raises (lowers) the energy of the conduction bands that have s (non–s) character on these sites*". To assess for this, and since the character of charges does not change qualitatively, i.e., the state moving upwards (downwards) still has s (non–s) character at the occupied site [12], we have calculated the angular momentum decomposition of the occupied interstitial site charges (Q_l) (in the Li atomic sphere) and the energy variations ($\Delta E = E_{LiCdP} - E_{InP}$) of the lowest conduction band at the high symmetry points L, Γ and X. The results are summarized in table 8.3. For the α phase the Γ and L states have s character and move upward in energy ($\Delta E > 0$ in table 8.3), whereas the X state which possesses a non–s character moves downward in energy, thus the '*interstitial insertion rule*' is successfully applied in this case (α phase). On the other hand, for the β phase the L state which has a non–s character moves downwards, and the X state with a strong s character moves upwards, while the Γ state has s character but moves downwards in energy, so it does not obey the '*interstitial insersion rule*'. In conclusion the '*interstitial insertion rule*' is not obeyed by all conduction band variations of LiCdP as in the case of LiMgP [13], where it has been found that this rule cannot be applied in predicting all conduction band modifications of LiMgP.

Table 8.2: Calculated bandgaps (in eV) of α–LiCdP, β–LiCdP and InP

	α–LiCdP	β–LiCdP	InP
Γ–Γ	0.635[1], 1.30[2]	0.396[1]	0.521[1], 1.35[3]
Γ–X	1.189[1]	1.606[1]	1.571[1]
Γ–L	1.669[1]	0.771[1]	1.318[1]

[1]This work,
[2]Expt. [22],
[3]Expt. [33].

Table 8.3: The energy variations of the first conduction bands in LiCdP compared to zinc–blende InP ($\Delta E = E_{LiCdP} - E_{InP}$, where E corresponds to the respective conduction band states), and the percentages of s–like (Q_s) and non–s–like (Q_{non-s}, i.e., p, d, f components) charges inside the Li atomic sphere in the respective conduction band states

		L	Γ	X
α–LiCdP	ΔE (eV)	0.351	0.114	−0.382
	Q_s	7.752 %	2.464 %	0.000 %
	Q_{non-s}	0.389 %	0.185 %	6.014 %
β–LiCdP	ΔE (eV)	−0.547	−0.125	+0.035
	Q_s	0.339 %	11.817 %	20.864 %
	Q_{non-s}	9.433 %	0.137 %	0.027 %

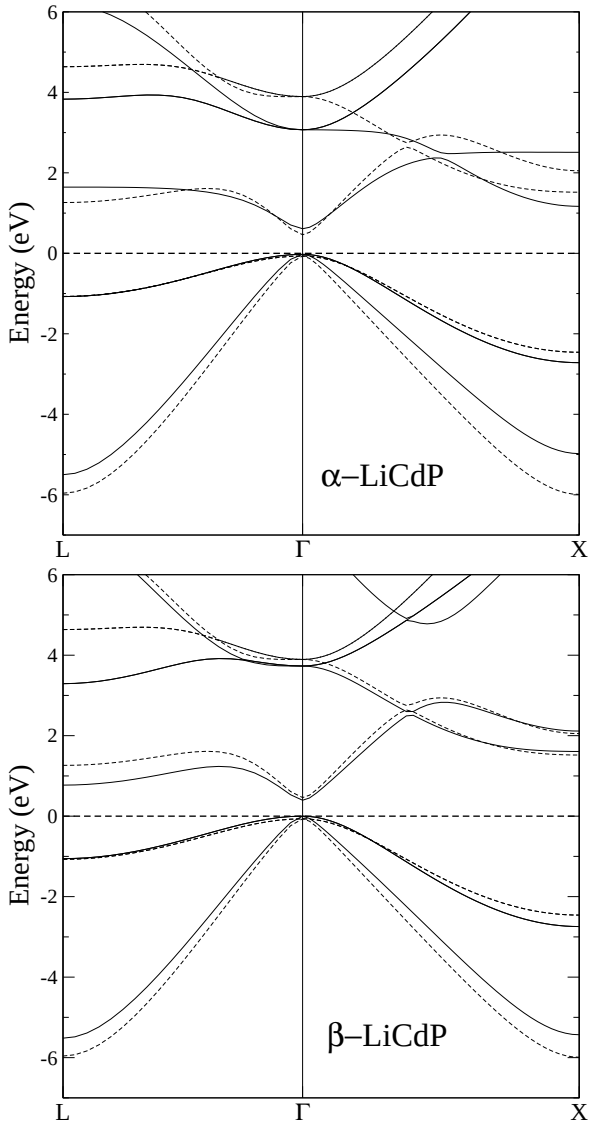

Figure 8.2: Electronic band structures of α–LiCdP and β–LiCdP. For comparison, the dashed lines show the bands of zinc–blende InP. The Fermi level is set to 0.

8.3.3 Valence charge density and bonding character

To gain more insight on the bonding character and to explain the charge transfer in LiCdP and InP, we have calculated the valence charge densities in the (110) plane.

Figure 8.3 depicts the charge contours and figure 8.4 shows the charge profiles along the $< 111 >$ direction. From this figure there is a great similarity between the charge density of the Cd–P and In–P bonds, they are characterized by a strong charge overlapping and bonding maxima, which is clearly seen in the profile plots (in figure 8.4 the charges are drawn toward the P atom and exhibit a single hump in the bond charge), therefore they can be characterized by a strong covalent character and a weak ionic one. On the other hand the Li–P bond in α–LiCdP and the Li–Cd one in β–LiCdP are nearly purely ionic. So that, LiCdP can be characterized as half–ionic and half–covalent at the same time. These bonding characteristics were also found in the other filled tetrahedral compounds LiZnAs [10] and LiZnP [6].

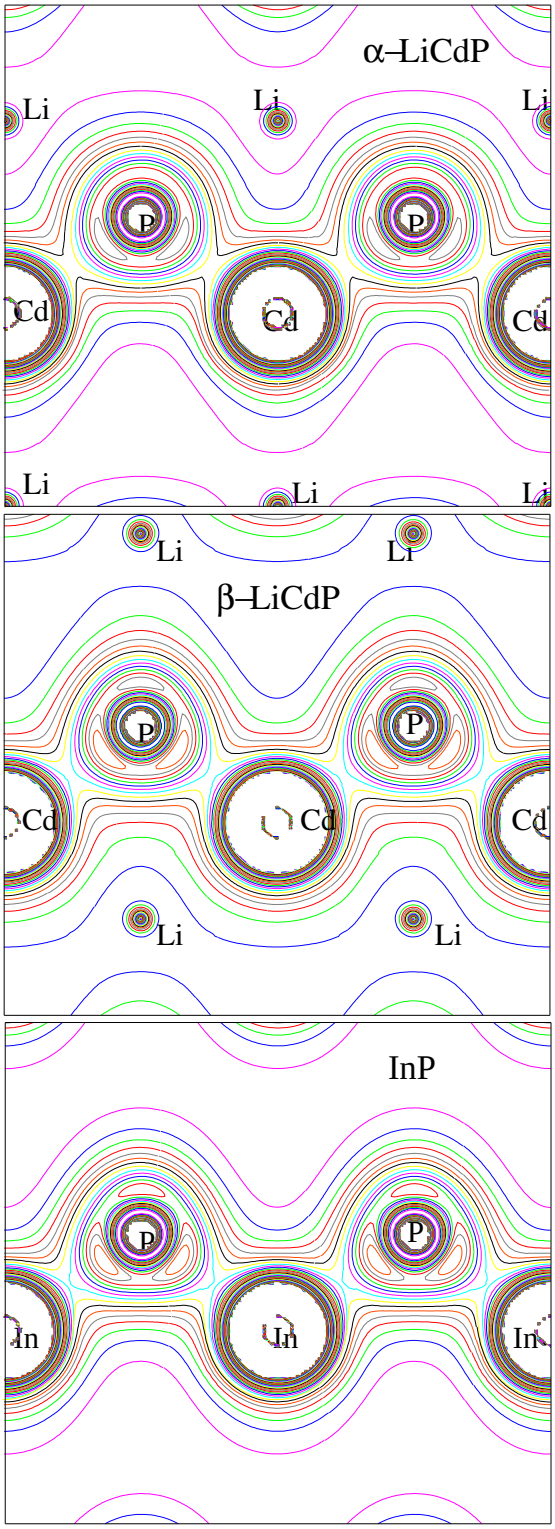

Figure 8.3: Valence charge density contours in the (110) plane.

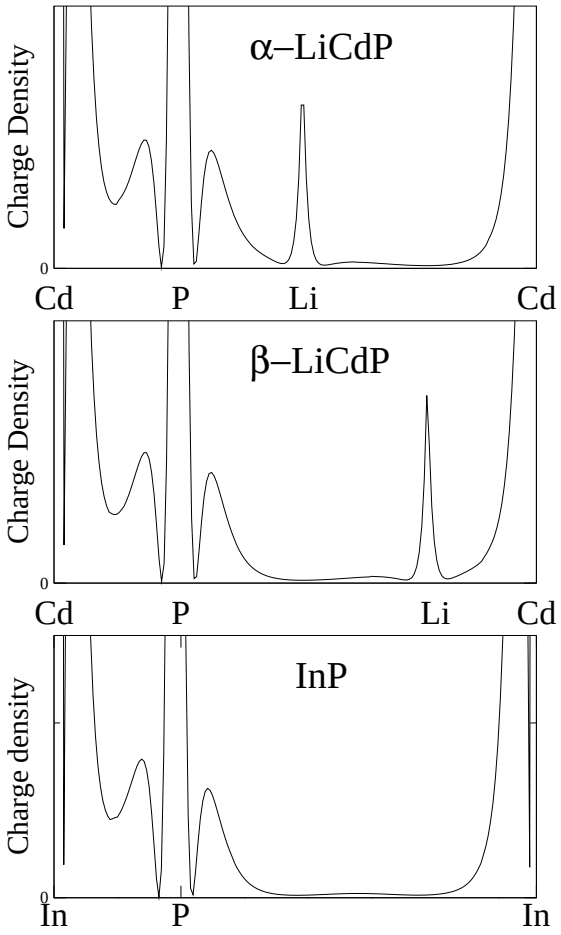

Figure 8.4: Charge profile along the $< 111 >$ direction.

8.4 Conclusion

In conclusion, we have used the full potential linearized augmented plane wave method within the local density approximation to investigate the structural, electronic and bonding properties of the filled tetrahedral compound LiCdP. Total energy optimization gives ground state structural parameters in good agreement with experiment and shows that the most stable phase of LiCdP is the α one. The conduction band modifications at high symmetry points Γ, X and L are discussed and found to obey the '*interstitial insertion rule*' except the Γ state of β–LiCdP. The calculated bandgaps show that the direct gap of α–LiCdP is larger than the one of InP, while the opposite is true for the indirect gap Γ–X. The valence charge densities show that the Cd–P bonds have covalent character in both α and β phases, whereas, the Li–Cd bond in β–LiCdP and the Li–P one in α–LiCdP are nearly purely ionic, so that the filled tetrahedral compound LiCdP can be characterized as half–covalent and half–ionic at the same time.

BIBLIOGRAPHY

[1] H. Nowotny, K. Bachmayer, Mh. Chem. 80 (1949) 734.

[2] R. Juza, F. Hund, Z. Anorg. Chem. 257 (1948) 1.

[3] K. Kuriyama and T. Katoh, Phys. Rev. B **37** (1988) 7140.

[4] K. Kuriyama, Y. Takahashi and K. Tomizawa, Phys. Rev. B **47** (1993) 13861.

[5] K. Kuriyama, T. Kato and T. Tanaka, Phys. Rev. B **49** (1994) 4511.

[6] K. Kuriyama, T. Kato and T. Tanaka, Phys. Rev. B **49** (1994) 11452.

[7] K. Kuriyama, K. Nagasawa, K. Kushida, J. Cryst. Growth **237/239** (2002) 2019.

[8] D.M. Wood, A. Zunger and R. de Groot, Phys. Rev. B **31** (1985) 2570.

[9] A.E. Carlsson, A. Zunger, D.M. Wood, Phys. Rev. B **32** (1985) 1386.

[10] S.–H. Wei, A. Zunger, Phys. Rev. Lett. **56** (1986) 528.

[11] H.–P. Li, Z.–F. Hou, M.–C. Huang and Z.–Z. Zhu, Chinese Phys. Lett. **20** (2003) 114.

[12] L.H. Yu, K.L. Yao and Z.L. Liu, Physica B **353** (2004) 278.

[13] L.H. Yu, K.L. Yao and Z.L. Liu, Solid State Commun. **135** (2005) 124.

[14] D.M. Wood, and W.H. Strohmayer, Phys. Rev. B **71** (2005) 193201.

[15] H.C. Kandpal, C. Felser and R. Seshardri, J. Phys. D: Appl. Phys. **39** (2006) 776.

[16] F. Kalarasse and B. Bennecer, J. Phys. Chem. Solids **67** (2006) 846.

[17] F. Kalarasse and B. Bennecer, J. Phys. Chem. Solids **67** (2006) 1850.

[18] F. Kalarasse, B. Bennecer and A. Mellouki, J. Phys. Condens. Matter **18** (2006) 7237.

[19] B. Bennecer and F. Kalarasse, *Algerian Journal of Advanced Materials (AJAM)* ISSN: 1111-625X, 3 pp. 23–26. Proceedings of the Fourth International Congress on Material Science and Ingineering CISGM-4, Tlemcen, Algeria, 2-4th May, 2006.

[20] A. Bouhemadou, R. Khenata and F. Zerarga, Solid Satate Communication **141** (2007) 288.

[21] L. Kalarasse, A. Mellouki, B. Bennecer and F. Kalarasse, *Pressure effect on the optical properties of the filled tetrahedral semiconductors LiZnX (X=N,P, and As)*, J. Phys. Chem. Solids, in press.

[22] R. Bacewicz and T.F. Ciszek, Appl. Phys. Lett. **52** (1988) 1150.

[23] Z. Pawlowska, N.E. Christensen, S. Satpathy and O. Jepsen, Phys. Rev. B **34** (1986) 7080.

[24] A. Mellouki, L. Kalarasse, B. Bennecer and F. Kalarasse, *First principles calculations of the structural and elastic properties of the filled tetrahedral compounds LiCdX (X=N,P,As)*, Comput. Mater. Sci., in press.

[25] S.L. Richardson and M.L. Cohen, Phys. Rev. B **35** (1987) 1388.

[26] D. Singh, *Planes waves, pseudo-potentials and the LAPW method*. Kluwer Academic Publishers, Boston, Dortrecht, London, 1994.

[27] P. Blaha, K. Schwarz, G.K.H. Madsen, D. Kvasnicka and J. Luitz, *WIEN2k, An Augmented Plane Wave + Local Orbitals Program for Calculating Crystal Properties*. Karlheinz Schwarz, Techn. Universität Wien, Austria, 2001. ISBN 3-9501031-1-2.

[28] P. Hohenberg and W. Kohn, Phys. Rev. B, 136, (1964) 864.

[29] W. Kohn and L.J. Sham, Phys. Rev. A, **140**, (1965) 1113.

[30] J.P. Perdew and Y. Wang. Phys. Rev. **B** 45 (1992) 13244.

[31] F.D. Murnaghan. *Proc. Natl Acad. Sci, USA*, **30** (1944) 244.

[32] M.–Z. Huang and W.Y. Ching, Phys. Rev. B **47** (1993) 9449.

[33] P.Y. Yu and M. Cardona, Fundamentals of Semiconductors, Third edition, Springer, 2001.

CHAPTER 9

Summary and concluding remarks

We have used the full–potential linearized augmented plane wave method in the framework of the density functional theory in order to investigate the structural, electronic and optical properties of a series of semiconducting compounds including the rocksalt GeTe, SnTe, and PbTe, the antifluorite Be_2C, Mg_2C, Mg_2Si and Mg_2Ge, and the Nowotny–Juza filled tetrahedral compounds LiZnN, LiZnP, LiZnAs and LiCdP.

The calculated structural parameters are in good agreement with the available experimental data. The band structure and density of states show that all the studied compounds are semiconductors. The obtained bandgap values, even underestimated by the LDA, are in good agreement with the measured ones. The anomalous feature of the electronic band structure of the filled tetrahedral compounds is the small gap of LiZnN compared to LiZnP which is attributed to the strong p–d coupling in this compound. The band structure of LiCdP shows that this compound obeys the interstitial insertion rule.

The optical spectra of GeTe, SnTe, and PbTe are successfully calculated. However, increasing the density of the k–mesh in the BZ is shown to shift the structures and peaks positions to lower energies. The microscopic origin of the main

features in the optical spectra is analyzed, and found to be due to transitions between the highest valence and lowest conduction bands, which are both of p character. Furthermore, the contributions of the different regions in k–space are discussed in terms of the transition band structures. The positions of the main peak in the imaginary part of the dielectric function decrease through this sequence PbTe–SnTe–GeTe in the cubic phase. For SnTe and PbTe, our calculated spectra are in good agreement with the experimental ones.

The predicted values of the static dielectric constants for LiZnP and LiZnAs are close to those of the binary compounds GaP and GaAs, respectively. So that the coordination change does not affect much the dielectric constants.

We have also studied the effect of hydrostatic pressure on the electronic and optical properties of the antifluorite compounds Be_2C, Mg_2C, Mg_2Si and Mg_2Ge. The calculated pressure coefficients indicate that the $E_g^{\Gamma-\Gamma}$ and $E_g^{\Gamma-L}$ increase with pressure for all the studied compounds, whereas $E_g^{\Gamma-X}$ increases with pressure for the carbide compounds and decreases for the other two and it is negative beyond 6.1 GPa for Mg_2Si and 6.7 GPa for Mg_2Ge. Furthermore, the smaller value of the first order pressure coefficient of Be_2C compared to diamond is attributed to the ionic character of the Be–C bond in this compound. The structures in the optical spectra shift towards higher energies when the pressure increases and the static dielectric function decreases with pressure.

The most important conclusions of our study is that :
(i) The bandgap of IV-VI compounds has anomalous behaviour, it increase in the following order GeTe–SnTe–PbTe.
(ii) The Nowotny Juza filled tetrahedral compounds follow the same behaviour as their binary analogous III–V zinc-blend, and their properties are closely related to them, including elastic constants, sound velocities, electronic band

structure and optical properties, with some modifications, for example the degree of directness of the bandgap is changed as a result of the distortion of band structure which can be understood through the charge distribution at high symmetry points of the Brillouin zone in conjunction with the interstitial insertion rule. These findings indicate that Nowotny–Juza compounds provide new opportunities in bandgap engineering.

(iii) The valence charge densities show that the Zn–P, Zn–As and Cd–P bonds have covalent character, whereas, the Li–Cd, Li–P and Li–As bonds are nearly purely ionic, so that the filled tetrahedral compound LiZnP, LiZnAs and LiCdP can be characterized as half–covalent and half–ionic semiconductors at the same time. Whereas, Li–N and Zn–N bonds are strongly ionic, so that LiZnN is an ionic semiconductors.

(iv) The peaks and structures of the imaginary part of dielectric function are shifted towards higher energies as the cation atomic number increases for rocksalt IV-VI compounds, and shift towards lower energies for the antifluorite compounds. For the Nowotny–Juza compounds the peaks shift towards lower energies when the anion atomic number increases.

(v) The static dielectric constant decreases as the cation atomic number increases in the rocksalt IV-VI compounds, whereas the inverse occurs for the antifluorite compounds where it increases. On the other hand, it increases with anion atomic number for the Nowotny–Juza compounds and follows the same trend as the III-V zinc-blend–like compounds.

(vi) Under hydrostatic pressure the electronic band structures and optical spectra of antifluorite semiconductors follow the same behaviour as those of zinc–blend–like and diamond–like elemental semiconductors.